N° d'ordre : 3727

Thèse

présentée devant
l'UNIVERSITÉ DE RENNES I
pour obtenir le grade de
Docteur de l'Université de Rennes I
Mention : *Traitement du Signal et Télécommunications*

par
Khwaja Ahmed Shaharyar

Équipe d'accueil : Institut d'électronique et de télécommunications de Rennes
École doctorale : Matisse
Composante universitaire : UFR Structure et Propriétés de la Matière

Génération rapide de signaux radar d'environnements complexes pour la simulation de systèmes imageurs SAR

Soutenue le 25 mars 2008 devant la commission d'examen

Composition du jury

Président du jury	
René Garello	Professeur–Telecom Bretagne, Brest
Rapporteurs	
Jean-Marie Nicolas	Professeur–Telecom ParisTech, Paris
Torbjørn Eltoft	Professeur–Université de Tromsø, Norvège
Examinateurs	
Christian Cochin	Ingénieur–DGA / CELAR, Expert en Détection Electromagnétique, Bruz
Laurent Ferro-Famil	Maître de Conférences–Université de Rennes 1
Membre invité	
Marijke Vandewal	Répétiteur–Ecole Royale Militaire, Belgique
Directeur de thèse	
Eric Pottier	Professeur–Université de Rennes 1

This thesis is dedicated to my father Khwaja Ahmed Khurshid, my mother Azra, my sister Ayesha, her spouse Khurram, and their adorable children Nausherwan and Jahanara

Contents

Acknowledgements

I would like to thank Prof. Eric Pottier for accepting me in the Remote Sensing group "SAPHIR", providing funding for the whole period of the PhD thesis and making it possible for me to participate in different international conferences. I would also like to express my gratitude to Dr. Laurent Ferro-Famil for introducing me to SAR during my Masters degree internship, accepting me as a doctoral candidate and proposing this thesis, and discussing my queries. Both Prof. Pottier and Dr. Ferro-Famil, not only provided an example of hard work by their ubiquitous presence in the lab, but also created a cordial environment owing to their friendly demeanor. I also thank them for giving me an exposure to a research environment.

I thank Prof. René Garello for agreeing to become the president of the jury, Prof. Torbjørn Eltoft and Prof. Jean-Marie Nicolas for reading thoroughly my thesis report and giving highly useful remarks for its improvement, Mr. Christian Cochin for his presence as an examiner and Dr. Marijke Vandewal for her encouraging remarks and suggestions for clarifying my manuscript.

My special acknowledgements to the group secretary Ms. Joëlle Drouet who took care of all the administrative procedures and offered good advices on different matters.

I am indebted to Stefan, with whom I had many useful discussions and whose constant presence in the office provided me good company. He proved to be a dependable and trustworthy friend time and again. Thanks are also due to my friend Aïssa, who, besides keeping me company and lending a helping hand quite often, introduced me to LaTeX. I am equally grateful to Hung and Son for their reassuring friendship and timely help.

I owe thanks to the current and the former group members, especially Maxim, Sandrine, Nicolas, Stéphane, Yue, Sangun, Franck, Tadashi, Dr. Sophie Allain, Dr. Stéphane Méric and Frédéric Boutet for their efforts to create a convivial atmosphere in the group, and I wish all of them good luck in their future endeavors. I would also like to acknowledge other lab members, in particular Prof. Kouroch Mahdjoubi, Noëlle, Franck N., Constant, Shoaib, Papa Moussa, Demba, Metin, Dr. Anne-Claude Tarot, Wafa, Thomas and Tinh for their pleasantness.

I thank Prof. Gérard Faucon, Dr. Jean-Jacques Bellanger, Prof. Jean-Pierre Le Cadre, Mr. Pommier and Ms. Odile Barange for their kindliness during my Masters studies, and I would also like to appreciate Dong, Phuong, Reza, Omer, Sheraz, Roméo, Sigrid, Margot, Karim, Basel, Ripu and Neerja for their friendly behavior.

Finally, I would like to express my profound gratitude to my family members: My parents for their guidance and numerous sacrifices that enabled me to pursue higher studies, my sister and my brother-in-law for their support, and my aunt, uncle and cousin for their caring attitude.

List of Figures

List of Tables

Notations

Altitude	z
Antenna length in azimuth direction	l_y
Antenna length in ground-range direction	l_x
Aspect angle/Instantaneous angle	θ_{as}
Azimuth aperture angle	θ_y
Azimuth Fourier transform	F_y
Azimuth position	y
Azimuth position varying slant-range	$d(y)$
Azimuth resolution	δy
Azimuth velocity of a moving object	v_y
Azimuth wavenumber	k_y
Carrier frequency	f_c
Carrier wavelength	λ_c
Carrier wavenumber	k_c
Chirp rate	K_r
Chirp rate in the distance azimuth wavenumber domain	$K(r, k_y)$
Chirp scaling algorithm	CSA
Correlation (interferometric/polarimetric)	$\gamma_{i/p}$
Double bounce reflection mechanism	DB
Fast Fourier transform	FFT
Fourier Transform	FT
Ground range	x
Ground range velocity of a moving object	v_x
Geometric optics	GO
Ground range resolution	δx
Physical optics	PO
Inverse azimuth Fourier transform	F_y^{-1}
Inverse chirp scaling algorithm	ICSA
Inverse fast Fourier transform	IFFT
Inverse Fourier transform	IFT
Inverse omega-k algorithm	IOKA
Inverse range Fourier transform	F_r^{-1}
Motion compensation	MoCo
Narrow bandwidth	Nba

Narrow beamwidth	Nbw
Normalized azimuth velocity of a moving object	$\mathbf{v_y}$
Normalized slant range velocity of a moving object	$\mathbf{v_r}$
Number of samples for chirp in azimuth direction	n_a
Number of samples for transmitted chirp	n_t
Number of scene samples in azimuth direction	n_y
Number of scene samples in range direction	n_r
Omega-k algorithm	OKA
Principle of stationary phase	POSP
Range cell migration	RCM
Range Fourier transform	F_r
Pulse repetition frequency	f_{PRF}
Range resolution	δr
Range wavenumber with carrier wavenumber	k_r
Range wavenumber without carrier wavenumber	Δk_r
Raw data	RD
Reflectivity map	$\sigma(r, y)$
Scattering matrix	S
Sensor height	h
Sensor velocity	v_{SAR}
Shortest slant-range	r
Single bounce reflection mechanism	SB
Slant range velocity of a moving object	v_r
Speed of light	c
Subaperture	SA
Swath length in azimuth direction	ΔY
Swath length in ground range direction	ΔX
Incidence angle	θ
Time bandwidth product	TBP
Transmitted bandwidth	B_t
Transmitted pulse	$p(t)$
Transmitted time	t
Transmitted wavenumber with carrier wavenumber	k
Transmitted wavenumber without carrier wavenumber	Δk
Triple bounce reflection mechanism	TB
Widebeamwidth	Wbw

Introduction

Remote sensing consists of data acquisition by means of imaging sensors and has many important applications, e.g., imaging of the Earth surface, imaging of ocean floors, assessment of crop conditions, etc. Imaging sensor systems, that may be airborne or satellite borne are classified in two categories: The first one is passive sensors, which make use of the natural radiation emitted or reflected by the surface of the object being observed. The second category is that of active sensors, which have a transmitter.

Spatial resolution is an important feature of the imaging systems, which can be described as the minimum distance at which two different objects can be differentiated. The passive sensors have the resolutions ranging from a few meters to tens of meters [1]. However, their main limitation is the inability to operate in the presence of clouds or fog. This can be overcome by the active sensors operating in the microwave range of the electromagnetic spectrum. This reduces the effects of clouds and fog and allows them to be independent of external sources for imaging, i.e., having a day and night, and all-weather imaging capability. These active sensors are represented by radars. However, they also have a disadvantage in the form of poor resolution to antenna dimension (aperture) relationship, e.g., an active transmitter operating at a wavelength of 1 m and having a physical aperture of 1 m placed at a distance of 1000 m from an observation point results in a resolution of 1000 m, that is insufficient. In order to achieve a higher resolution, e.g., 1 m, the antenna aperture should be increased to 1000 m [2]. Due to physical limitations, it is not possible to manufacture an antenna of such a long length and mount it on an airborne platform.

A solution to this problem can be obtained by artificially creating the effect of a long antenna, by moving a smaller one along a certain path, which emits electromagnetic pulses perpendicular to the flight path and downward to the Earth surface. The received signals at the different positions on the path are stored and then processed afterwards. Synthetic Aperture Radar (SAR) is based on this concept.

The signals received by SAR depend on the energy reflected from a point target spread in across-flight and along-flight directions. The purpose of SAR focusing/processing/image formation is to collect (compress) this dispersed energy into a single pixel in the output image. In early SAR systems, optical processing was used for processing the received data, however, presently, digital processing techniques are the preferred methods [1]. The traditional SAR processing technique is Range-Doppler Algorithm [3] whereas newer techniques are Chirp Scaling Algorithm [4] and Omega-K Algorithm, either borrowed from geophysics [5] or considered from a signal processing point of view [2], [6] . Each of these algorithms are suited for different configurations/parameters, although the latter one may

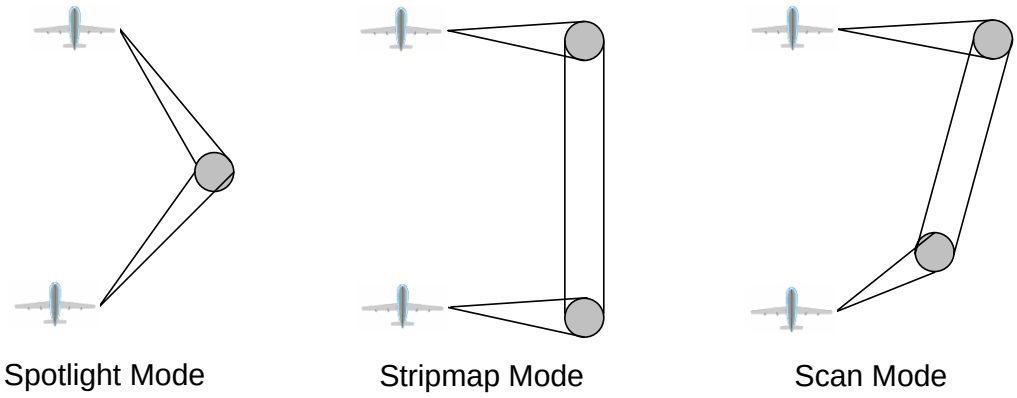

Figure 1: SAR Operating Modes

be the exact form.

There are three operating modes for a SAR system: Spotlight, stripmap and scan, as shown in figure 1. In the spotlight mode, the antenna beam is steered to continuously illuminate the terrain patch being imaged. In the stripmap mode, the radar antenna points along a fixed direction with respect to the flight path, thus covering a strip of terrain parallel to the path of motion. The stripmap mode involves either a broadside geometry, in which the antenna beam points perpendicular to the flight direction, or a squint geometry, where the antenna is pointed at some angle to the normal of the flight path. In the scanmode, the antenna is steered to illuminate a strip of terrain at any angle to the flight path. This thesis is concerned with the airborne stripmap mode and broadside geometry.

This thesis is carried out in the framework of the Brittany region project MOSISMAR in collaboration with ENST Bretagne. The project is concerned with the development of a simulator that may eventually be applied to model different sea states. As a first step, different SAR processing algorithms are studied and simulations of raw data are carried out for realistic, static and anisotropic scenes, as well as a moving object.

The objectives of this thesis are to study the SAR imaging process and suggest efficient techniques to model it, i.e., SAR raw data generation. This may be necessary to test different focusing procedures, to study the interaction of an electromagnetic wave with a surface, effects of different parameters on the focused image quality, simulation of different errors, mission simulation tool [7], [8] etc. Moreover, space agencies can have access to different types of raw data in a short period of time, but in case of other research environments, this is quite limited. Raw data for new configurations are not easy to obtain and with the help of simulation, it may be possible to simulate new SAR configurations [9].

This thesis initiates with the presentation of the basics of SAR geometry and different mathematical expression are presented that describe the relation of along-flight and across-flight resolutions to different parameters. It is shown that the use of a linear frequency modulated signal called a chirp signal leads to a high resolution in the across-flight di-

rection. The range frequency varying nature of the azimuth frequency is demonstrated as well. It is also shown that the movement of a sensor leads to a high resolution in the along-flight direction due to creation of a chirp in this direction at the expense of a phenomenon called range migration due to a changing radar-object distance. This effect complicates the processing as it should be compensated to compress the raw data. The image formation process is introduced for a single point, followed by time-domain processing in case of multiple points known as the Backprojection algorithm [2]. The basics of interferometry that enables height calculation from phase difference of two images are also discussed, alongwith an example for a single point. The corresponding relations between the measured phase and height are described. Polarimetry is discussed briefly, alongwith important parameters, used later on in the thesis.

Processing in time-domain is computationally very intensive and may require heavy computational resources. As a result, different alternatives have to be considered, that consist of processing in the frequency domain. In chapter 2, the corresponding expressions of the raw data in one dimensional and two dimensional frequency domains calculated using the principle of stationary phase (itself an approximation) are explained. The possibility of image formation in each one of these domains is discussed and it is shown that a single point can be focused in the two dimensional frequency domain using a matched filter. This matched filter, however, changes for each point and using an approximate approach of subpatches [10], it is possible to focus images in the two dimensional frequency domain using a matched filter tuned for each subpatch center. However, there is a tradeoff between computational efficiency and accuracy and the phase error, that may arise due to the lack of adaptivity within a subpatch, is calculated and other alternatives are proposed. The first one is the Omega-k algorithm, that achieves the focusing in the two dimensional frequency domain, using a reference matched filtering and an interpolation. This is the exact form of image formation and can cater for wide aperture focusing. The second approach is the Chirp Scaling algorithm, that consists of equalizing the range migration trajectories in the one dimensional frequency domain by using a reference chirp signal. After equalization, range migration can be compensated by a fixed range shift. The approximations involved in the Chirp Scaling algorithms are also briefly mentioned. The steps involved in these two algorithms are summarized alongwith the block diagrams and examples with simulated raw data and images. The differences between the two dimensional spectra of raw data and of a focused image are also demonstrated. The original form of the Omega-k algorithm, borrowed from seismic processing is also detailed.

Raw data simulation in its simplest form, i.e., in time-domain is explained. It is clear that this approach consists of calculating a delayed chirp signal for each point in the image and for all the trajectory positions. Thus, it is a summation process in both along-flight and across-flight direction and requires high computational resources that may not be always available. Consequently, in chapter 3, this process is explored in the frequency domain. It is shown that, similar to the case for processing, the computational efficiency for this process can be improved using expressions in the two dimensional frequency domain. An improvement of this simulation technique using Fast Fourier Transforms in one dimension, is introduced to increase the efficiency as the summation process is reduced to one dimension only. The accuracy of this method is estimated by comparing the simulated

raw data to those obtained using a time-domain simulator. Subsequently, phase differences between both two raw data are compared in the along-flight and across-flight direction. It is shown that with some further manipulations, the simulation process can be realized efficiently in the two dimensional frequency domain. A relationship between the reflectivity map and the corresponding image is shown, that is actually the two dimensional convolution of the reflectivity map and a SAR image for a reference range and azimuth position. It is concluded that raw data can be simulated using inverse processing algorithms, and the inverse Omega-k algorithm (involving the least number of approximations) is a good candidate for this purpose. The inverse Chirp Scaling algorithm is also examined, and the approximations involved are studied analytically to find a validity domain in terms of system parameters. It is also shown that a simulation method proposed in [11] has a much smaller validity domain compared to the approach presented in this thesis. The influence of approximations in case of the inverse Chirp Scaling is demonstrated by means of a relevant example and compared to the results obtained with the inverse Omega-k. A moving point/object raw data simulator is described and it is demonstrated that this process can be efficiently carried out using the previously described methods by means of a rotation and a scaling operation.

It is the sensor movement that gives rise to high resolution in azimuth at the expense of range migration that can be compensated. Similarly, sensor motion errors (especially in the airborne case) arising due to different factors have to be compensated in order to obtain high-quality focused images. These motion errors cause defocusing and a position shift in the processed image. Error corrections are achieved by motion compensation algorithms that can be divided into two categories: Narrow-beamwidth and Wide-beamwidth. The former assumes that the aperture in the along-flight direction is narrow enough [12], so that motion errors within the azimuth beam are the same as those at the beam center and can be approximated to be along-flight position invariant. This process can be integrated very easily with the Chirp Scaling processing [13] or with a modified Omega-k algorithm [14] that can also take into account wide-beamwidth errors. Algorithms belonging to both the categories are described in chapter 4, alongwith some examples. The effects of motion errors on a processed image are also presented. The case of motion error simulation is subsequently discussed, and it is shown that unlike raw data simulation in the absence of motion errors, there is no direct method to achieve this. The only option is to combine frequency simulation, alongwith summation operation. This involves certain approximations, that are described in detail, alongwith some simulation examples and the phase error as a result of these approximations.

In order to analyze the accuracy of the proposed simulation schemes, examples with point scatterers were presented in chapters 3 and 4. In chapter 5, the simulation process is applied to an extended scene, consisting of a rough ground and single or multiple buildings. The concept of roughness and the different parameters that define roughness are explained. Speckle, that causes fluctuations of intensity in an image is described alongwith the building geometry and the corresponding features that can be observed in an image. The backscattering coefficients are subsequently explained. These coefficients, present in a reflectivity map, give the electromagnetic properties of a scene and are calculated using an electromagnetic model. These can be divided into a coherent and incoherent part that

can be seen as the mean and variance of a gaussian distribution, respectively. This gaussian distribution, infact represents the speckle. Expressions, calculated using an already existing model [15] are presented. The coherent part of the reflectivity that leads to an along-flight varying response, is also introduced and included in the simulation to make it more realistic compared to the already existing simulations. A subaperture analysis [16] is also carried out that shows the expected along-flight behavior of a scene consisting of buildings oriented at different angles. An example is also presented for raw data simulation in case of motion errors for a scene consisting of a single building. Interferometric SAR simulation is introduced, alongwith different types of decorrelation and simulation is carried out taking into account the geometric decorrelation only. However, the possibility of including other types of decorrelation such as misregistration, system noise, topography, etc are also discussed. With the presented approach, it is possible to generate not only raw data, but directly the interferometric image pairs as well. This process may be better than simulating just the interferogram as in [17], as the correct geometric decorrelation is taken into account using range spectral shift, and may be used for studying range resolution improvement. In the case of simple interferogram simulation, the decorrelation is achieved using correlated gaussian variables, which, although correct, cannot be used for studying the previously mentioned phenomenon. Examples are given in the case of a plane surface and a scene, consisting of a building, and the height estimations using the simulated interferometric image pairs are shown to match with the actual height.

Summarizing the previous discussion, the manuscript is organized as follows:

- Chapter 1 presents the SAR basics, and gives as well an introduction to image formation.
- Chapter 2 describes the Omega-k and Chirp Scaling algorithms.
- Chapter 3 examines different simulation strategies, their computational complexity and their accuracy for simple point scatterers as well as a moving point scatterer or an object.
- Chapter 4 describes the possibility to simulate raw data in the presence of sensor motion errors, alongwith the approximations involved and their limits of validity .
- Chapter 5 applies results of the previous chapters to an extended scene and presents an introduction to interferometric SAR simulation.

At the end of this manuscript, conclusions are summarized and future directions for this work are presented.

Chapter 1

Basics of SAR

1.1 Outline of the Chapter

This chapter starts with the geometric configuration of a Synthetic Aperture Radar (SAR) system and presents its different characteristics. It discusses the main concepts behind the functioning by describing a chirp signal as well as demonstrating the data storage for the synthetic aperture. The relationships of the achieved resolution to various system parameters are calculated, as well as compared to those obtained by a conventional radar, in both along-flight and across-flight directions. The SAR image formation process[1] is introduced by two examples and the basic concepts of polarimetry and interferometry are discussed.

1.2 Geometric Configuration

The broadside geometric configuration of a SAR operating in the stripmap mode is shown in figures 1.1 and 1.2. The radar is situated at a height h and moves with a velocity v_{sar}. The along-flight axis is referred to as azimuth (y), while the across-flight axis is referred to as ground-range (x). The altitude is represented by z. The radar transmits in the direction normal to the flight direction following the radial axis and with an angle of incidence θ_i (θ_c at the center of the imaged scene), and the distance in the line of sight direction is known as slant-range (r)[2]. The relation between x and r is given as (assuming a point at ground range x and zero azimuth and altitude)

$$r^2 = x^2 + h^2 \tag{1.1}$$

Furthermore, the azimuth varying radar-target distance is

$$d(y)^2 = x^2 + y^2 + h^2 \tag{1.2}$$

Note that $d(y = 0) = r$.

[1] In this thesis, the terms SAR image formation, SAR processing and SAR data processing are used interchangeably

[2] In this thesis, the terms slant-range and range are used interchangeably

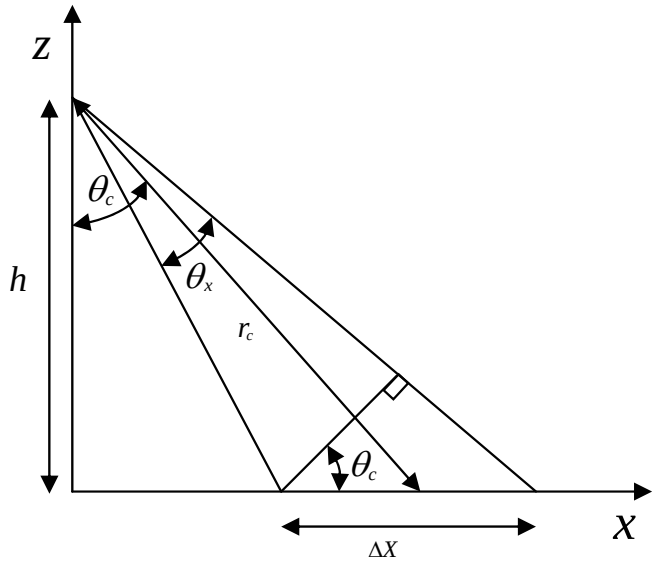

Figure 1.1: Broadside Geometry in Altitude Ground-Range Domain

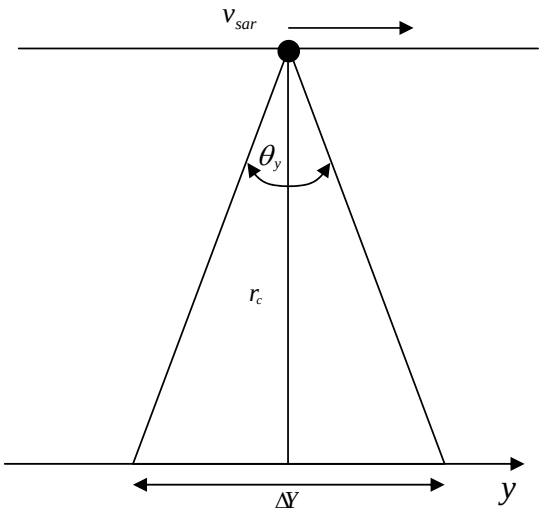

Figure 1.2: Broadside Geometry in Slant-Range Azimuth Domain

The area covered by the radar waves in the ground-range and azimuth directions is shown in figures 1.1 and 1.2. It is proportional to the apertures of the physical antenna having dimensions of l_x and l_y in the ground-range and azimuth directions, respectively. These apertures can be approximated in radians using the following relations:

$$\theta_x = \frac{\lambda_c}{l_x} \tag{1.3}$$

$$\theta_y = \frac{\lambda_c}{l_y} \tag{1.4}$$

where c is the speed of light, $\lambda_c = c/f_c$ is the wavelength and f_c is the carrier frequency of the transmitted signal.

1.2.1 Calculation of Ground Range Swath

Making use of the following relation between the incidence angle and the slant range at the center of the area covered by the antenna footprint, and the approximation $\tan(\theta_c) \approx \theta_c$ for small θ_c, an expression for range swath ΔX can be obtained as follows:

$$\cos(\theta_c) \approx \frac{r_c \tan(\theta_x/2)}{\Delta X/2} \tag{1.5}$$

$$\Delta X = \frac{r_c \theta_x}{\cos(\theta_c)} \tag{1.6}$$

1.2.2 Calculation of Azimuth Swath

From figure 1.2, the following expression can be obtained:

$$\tan(\theta_y/2) = \frac{\Delta Y}{2r_c} \tag{1.7}$$

Using again the small-angle approximation, ΔY can be written as

$$\Delta Y \approx r_c \theta_y \tag{1.8}$$

1.3 Resolution in Range

1.3.1 Conventional Radar

Let a and b be two fixed targets placed at slant-range distances of r_a and r_b, respectively from the radar. The time taken for the waves to travel back and forth is $\frac{2r_a}{c}$ and $\frac{2r_b}{c}$ for a and b, respectively and the two echoes are shifted in time by the duration given as follows:

$$\left| \frac{2r_a}{c} - \frac{2r_b}{c} \right| \tag{1.9}$$

$|r_a - r_b|$ is the distance that separates the two targets. The radar system can distinguish

between the two pulses if they are separated by a time delay of T_p, where T_p is the duration of the transmitted pulse. This is known as the resolution of a radar and is given in slant-range as

$$\delta r = \frac{cT_p}{2} \tag{1.10}$$

while the resolution in ground-range is

$$\delta x = \frac{\delta r}{\sin(\theta_i)} \tag{1.11}$$

where θ_i is the incidence angle corresponding to a slant-range distance of r_i.

1.3.2 Synthetic Aperture Radar

It can be remarked from equation 1.10 that in order to obtain a high slant-range resolution, the transmitted pulses must be of short duration. However, practically it is difficult to emit short pulses which have energy high enough to allow for the detection of the received echoes. A technique to emit a high average power without having a high peak power is the linear modulation of frequency. It consists of emitting pulses that are linearly modulated in frequency for a duration of time T_p in a frequency band B_t. The frequency of this signal "sweeps" this band centered on carrier frequency f_c at a chirp rate K_r. Such a signal is called a chirp because an audio signal of rising (or falling frequency) over time is similar to a bird's chirp [6] and has the following form:

$$p(t) = \text{rect}(t/T_p)\exp(j2\pi f_c t + j\pi K_r t^2) \tag{1.12}$$

where t represents the across-track time (also known as fast-time) and ranges from $\frac{-T_p}{2}$ to $\frac{T_p}{2}$.

The time-varying frequency can be written as

$$f_r(t) = f_c + K_r t \tag{1.13}$$

and the bandwidth is

$$B_t = K_r T_p \tag{1.14}$$

The chirp signal can be called an up chirp or a down chirp when the slope K_r is positive or negative, respectively. This signal after reflection from a point scatterer, is sampled at the receiver, and in order to fulfil the Nyquist criterion, the sampling frequency f_{st} must be greater than twice the highest transmitted frequency, from where the following limit for the sampling rate T_{st} is obtained:

$$T_{st} < \frac{1}{B_t} \tag{1.15}$$

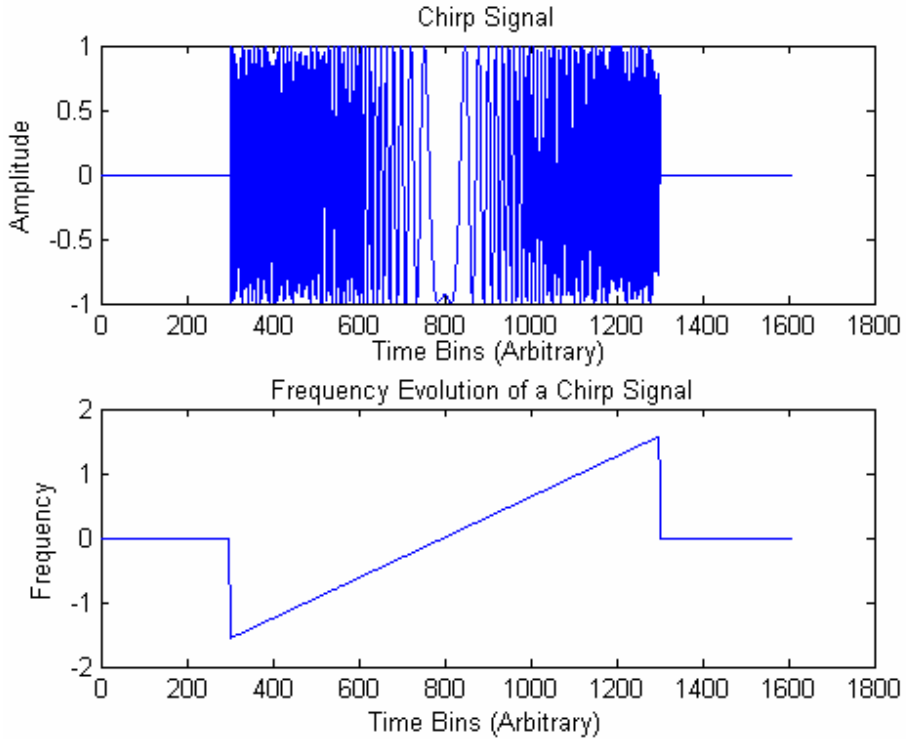

Figure 1.3: Chirp Signal and its Frequency

The sampled received data is stored in different bins or pixels and the bin/pixel size in slant-range is given as

$$\delta b_r = \frac{cT_{st}}{2} \tag{1.16}$$

Figure 1.3 shows an up chirp signal and its frequency evolution with respect to time. At the receiver, a matched filtering operation is performed, which consists of correlating the received chirp signal from a target located at distance r_a with the complex conjugate of the replica of the transmitted signal. This operation can be written as follows:

$$p_c(t) = \int_{-\infty}^{\infty} p\left(t - \frac{2r_a}{c}\right) p^*(t-u)du \tag{1.17}$$

The result of this integration is a sinc pulse, given by [3]

$$p_c(t) \approx T_p \text{sinc}\left\{K_r T_p \left(t - \frac{2r_a}{c}\right)\right\} \tag{1.18}$$

Its mainlobe width is inversely proportional to the bandwidth of the transmitted signal. Since this width is less than that of the received signal, it is known as the compressed

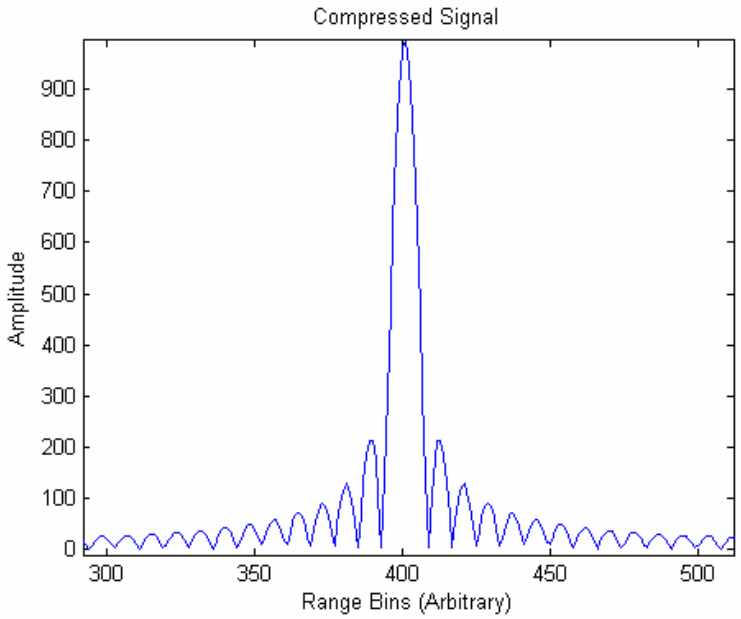

Figure 1.4: Compressed Signal after Matched Filtering Operation

signal [3]. Note that after compression, the time axis can be replaced by range (as the compressed pulse is localized in distance) and the compressed pulse can be expressed as

$$p_c(r) \approx T_p \text{sinc}\left\{2K_r T_p \frac{(r - r_a)}{c}\right\} \tag{1.19}$$

From equation 1.19, the slant-range resolution can be calculated as

$$\delta r = \frac{c}{2K_r T_p} = \frac{c}{2B_t} \tag{1.20}$$

Figure 1.4 shows the sinc pulse as a result of the operation described by equation 1.17. By observing it and taking into account equations 1.12 - 1.14 and 1.20, the advantages of the chirp signal can be summarized as:

- The transmitted signal at the radar has a high bandwidth but longer pulse duration, therefore, a satisfactory level of average power can be maintained without transmitting a very high peak power signal.
- After the matched filtering operation, the output signal is narrow, thus resulting in good range resolution.

Another parameter concerned with the chirp signal is the time bandwidth product defined as the product of the bandwidth of the chirp signal and its duration. It is given by

[3] Also known as focused signal

$TBP = B_r T_p = KT_p^2$ and can be seen as a measure of the number of zero crossings of the signal [3].

1.4 Resolution in Azimuth

1.4.1 Conventional Radar

For a traditional radar, the azimuth resolution at the center of the antenna beampattern is

$$\delta y_c = \frac{\lambda_c r_c}{l_y} \tag{1.21}$$

In this case, the larger the size of the antenna, the better the resolution. For a good resolution, the antenna becomes too large to be physically realizable, and a solution is to "artificially" create a large antenna.

1.4.2 Synthetic Aperture Radar

A large antenna can be synthesized by moving a smaller antenna and collecting the data received at all the along-flight positions. The received signal for a point located at a beam center slant-range distance of r_a (it is the shortest distance between the radar and the point illuminated and is reached when the radar is directly in front of the target) and an azimuth position y_a is

$$\begin{aligned} s_a(t,y) &= p\left(t - \frac{2d_a(y)}{c}, y\right) \\ &= \text{rect}\left\{\frac{(t - 2d_a(y)/c)}{T_p}\right\} \exp\left\{j2\pi f_c\left(t - \frac{2d_a(y)}{c}\right) + j\pi K_r\left(t - \frac{2d_a(y)}{c}\right)^2\right\} \end{aligned} \tag{1.22}$$

where $r_a = \sqrt{x_a^2 + h^2}$ and $d_a(y) = \sqrt{r_a^2 + (y - y_a)^2}$ for $-\Delta Y/2 \leq y \leq \Delta Y/2$, as the target is illuminated for a total azimuth distance of ΔY. x_a is the ground-range position of the target. The evolution of the radar-target distance $d_a(y)$ is shown in figure 1.5 for $r_a = 2611m$ and $y_a = 0m$. This hyperbolic form causes the received signal to shift in the range directions, and is known as range migration. The received signal is stored for each along-flight position as shown in the figure 1.6. It shows that besides the transmitted chirp in range direction, a chirp exists in azimuth direction as well due to the movement of the sensor and the subsequent storage of the received pulses, that can be seen on the right hand side of the figure. The shifting of the received pulses due to range migration is also indicated. The presence of the azimuth chirp in the received signal can be demonstrated analytically by considering the received signal after demodulation given by equation 1.23.

$$s_a(t,y) = E_t\left(\frac{t - 2d_a(y)}{c}\right) \exp\left\{-j4\pi f_c \frac{d_a(y)}{c} + j\pi K_r\left(t - \frac{2d_a(y)}{c}\right)^2\right\} \tag{1.23}$$

where $E_t(t) = \text{rect}(\frac{t}{T_p})$ is called the range envelope representing the chirp duration. For

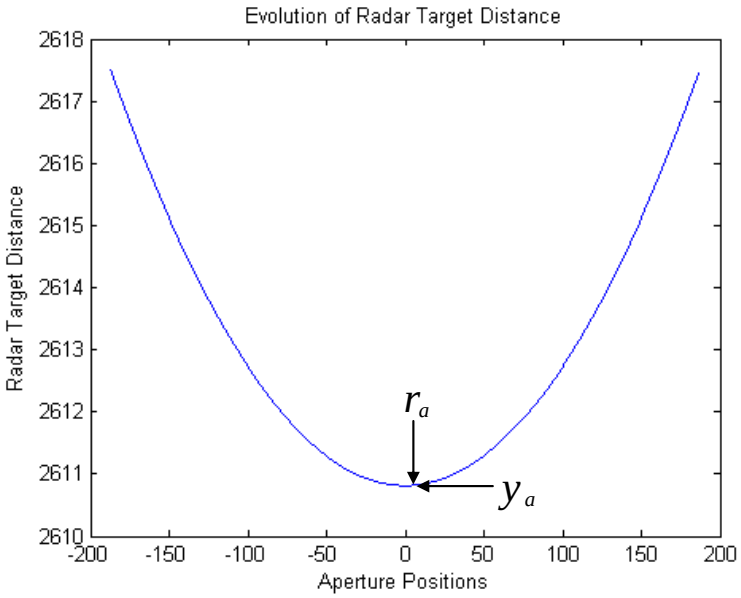

Figure 1.5: Evolution of the Distance between Radar and Target

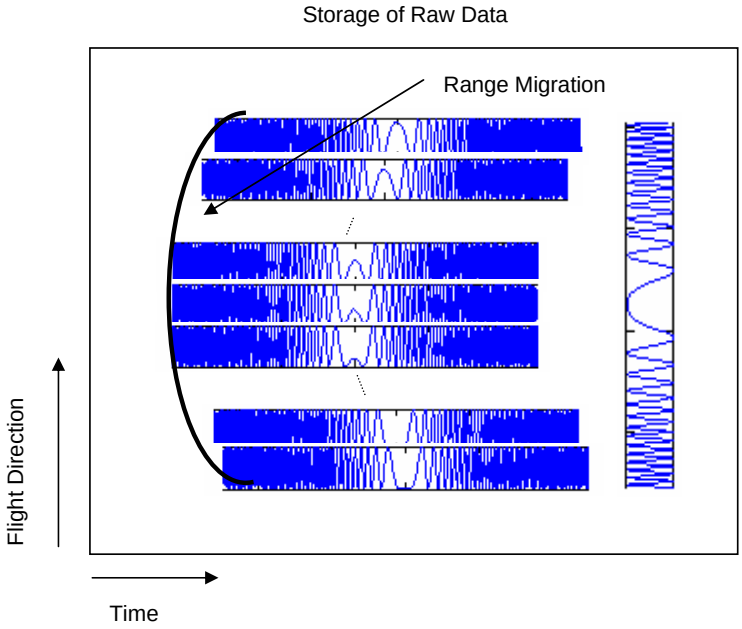

Figure 1.6: Storage of Raw Data and Presence of Azimuth Chirp

the moment, range migration is ignored by assuming $r_a \gg y$.

The expression given by equation 1.23 can be divided in two parts: The first exponential term representing the azimuth part $s_{ay}(t, y)$, whereas the second one representing the range part $s_{ar}(t, y)$ (as it contains the term t). Using the Taylor series approximation and parabolic approximation for the radar-target distance [3], ignoring the range envelope and considering a target at the centre of the scene, i.e., $y_a = 0$, we obtain

$$d_a(y) \approx r_a + \frac{y^2}{2r_a} \tag{1.24}$$

$$s_{ay}(t, y) = \exp\left\{-j4\pi\frac{f_c}{c}\left(r_a + \frac{y^2}{2r_a}\right)\right\} \tag{1.25}$$

The exponential term $\exp\left(-j2\pi\frac{f_c y^2}{cr_a}\right)$ represents a frequency modulated signal in azimuth direction, with a rate given by $K_y = 2f_c/cr_a$. Note that this rate is dependant on the shortest slant-range distance, and is thus different for each slant-range position. From equation 1.25 it is clear that due to the movement of the radar, a chirp has been generated in azimuth direction as well.

Azimuth resolution can be obtained by calculating the chirp signal bandwidth in the azimuth direction that can be achieved by multiplying the total aperture length with the above mentioned chirp rate. Using the relations given by equations 1.4 and 1.8, the bandwidth B_y comes out to be

$$B_y = K_y \Delta Y \simeq \frac{2}{l_y} \tag{1.26}$$

From this, the azimuth resolution can be approximated to be

$$\delta y = \frac{l_y}{2} \tag{1.27}$$

This resolution is much higher than that of a traditional radar having the equivalent dimensions.

The sampling frequency in azimuth is known as Pulse Repetition Frequency (f_{PRF}). To meet the Nyquist criterion, it should be greater than twice the highest azimuth frequency and thus the sampling time T_{sy} should satisfy the following constraint:

$$T_{sy} < \frac{1}{B_y} \tag{1.28}$$

The bin/pixel size for the received data in terms of azimuth distance is given by

$$\delta b_y = v_{SAR} T_{sy} \tag{1.29}$$

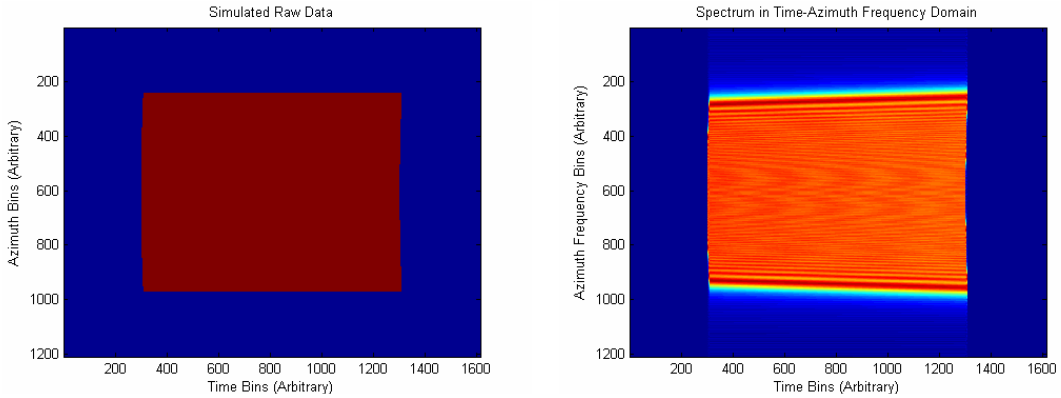

Figure 1.7: Simulated Raw Data in Time Azimuth Domain and its One Dimensional Spectrum in Azimuth Direction for a Single Point

1.4.3 Example with Simulated Data

Figure 1.7 shows an example of simulated data for a simple point target, as well as its spectrum in azimuth-frequency time domain. One interesting observation is that the azimuth bandwidth increases with time, shown by the trapezium like shape of the spectrum. This cannot be explained by equation 1.25. In order to explain it, $s_{ar}(y,t)$ is also taken into consideration and equation 1.23 is rewritten using the parabolic approximation:

$$\begin{aligned} s_a(t,y) \quad \approx \quad & \exp\left\{-j4\pi\frac{f_c}{c}(r_a+\frac{y^2}{2r_a})+j\pi K_r t^2\right\} \\ & \exp\left\{j4\pi K_r\frac{(r_a+y^2/2r_a)^2}{c^2}-j4\pi K_r\frac{(r_a+y^2/2r_a)t}{c}\right\} \end{aligned} \tag{1.30}$$

By simple observation or taking a double derivative of the above expression with respect to y and ignoring the term containing c^2 in the denominator as it is very small, the modified azimuth rate is calculated (assuming the azimuth aperture to be small and range migration to be negligible) as

$$K_{ym}(t) = \frac{2f_c}{cr_a} + \frac{2K_r(t-2d_a(y)/c)}{cr_a} - \frac{4K_r y^2}{c^2 r_a^2} \tag{1.31}$$

Thus in addition to the rate K_y, there is an extra term that varies with the across-flight time t. Defining $\theta_{as}(y) \approx (y-y_a)/r_a$, where $\theta_{as}(.)$[4] is called the aspect angle, the azimuth bandwidth is given as

$$B_y(t) \approx \frac{4f_c\theta_{as}(\Delta Y/2)+4K_r\{\theta_{as}(\Delta Y/2)\}t}{c} \tag{1.32}$$

or

$$B_y(t) \approx \frac{2f_r(t)\theta_{as}(\Delta Y)}{c} \tag{1.33}$$

[4] Also known as instantaneous squint angle

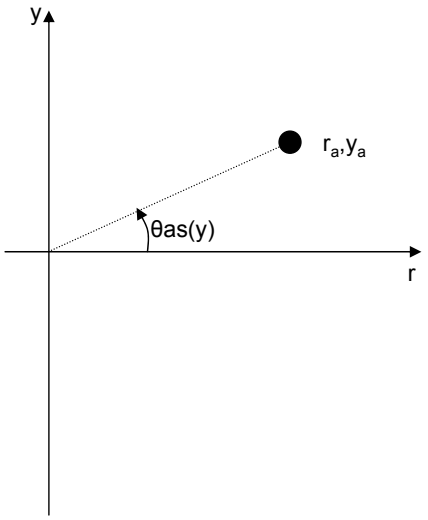

Figure 1.8: Aspect Angle

Thus, it can be seen that the azimuth chirp rate changes with time. Consequently, it can be stated that the bandwidth increases as a function of across-flight time, which explains the trapezium-like shape of the spectrum.

1.5 Introduction to Image Formation

The received data consists of information from the imaged scene spread over a certain interval. The purpose of image formation is to extract this information by compressing the data and thus reducing the spread resulting in a synthesized/compressed image. This process, known as SAR image formation/SAR data processing, will be discussed in the following subsections.

1.5.1 Focusing a Single Point Response

As discussed in the preceding sections, there are two chirps in the received signal: One in the range direction and the other in the azimuth direction. These chirps can be compressed by using one dimensional matched filtering in both directions. However, the presence of range migration hampers this direct process and involves another step, which consists of range migration compensation. This is necessary as the received pulses are shifted in range due to the hyperbolic form of the radar-target distance. Note that this is the price paid for having a higher resolution, as this effect arises due to the changing radar-target distance. The received data can be compressed in the range direction without range migration compensation, however, in order to achieve azimuth compression, this should first be compensated.

The demodulated received data for a single point at slant-range and azimuth position of r_a and y_a, respectively is given as

$$s_a(t,y) = E_t(t-2d_a(y)/c)E_y(y-y_a)\sigma(r_a,y_a) \exp\left\{-j4\pi f_c\frac{d_a(y)}{c}+j\pi K_r\left(t-\frac{2d_a(y)}{c}\right)^2\right\} \quad (1.34)$$

where $\sigma(r_a, y_a)$ is the reflectivity describing the electromagnetic properties of the target (at slant-range and azimuth position of r_a and y_a, respectively) and $E_y(y)$ is the envelope in the azimuth direction (due to the antenna beam pattern) defined as $E_y(y) = \text{rect}(\frac{y}{\Delta Y})$. As a first step, range compression is carried out by means of matched filtering in the range direction as follows:

$$s_{ad}(t,y) = \int_{-\infty}^{\infty} p\left(t-\frac{2d_a}{c}\right)p^*(t-u)du = E_t(t-2d_a(y)/c)E_y(y-y_a)\sigma(r_a,y_a) \exp\left\{-j4\pi f_c\frac{(r_a+y^2/2r_a)}{c}\right\} T_p\text{sinc}\left\{K_rT_p\left(t-\frac{2\sqrt{r_a^2+(y-y_a)^2}}{c}\right)\right\} \quad (1.35)$$

In the second step, range migration is compensated using shifts in the range directions. These shifts change the location of the sinc function in equation 1.35 from $\sqrt{r_a^2+(y-y_a)^2}$ to a fixed position r_a resulting in[5]

$$s_{ad}(r,y) = E_r(r-r_a)E_y(y-y_a)\sigma(r_a,y_a)\exp\left\{-j4\pi f_c\frac{(r_a+y^2/2r_a)}{c}\right\} T_p\text{sinc}\left\{\frac{2K_rT_p}{c}(r-r_a)\right\} \quad (1.36)$$

where $E_r(r) = \text{rect}(\frac{r}{cT_p})$. Finally, azimuth compression is carried out to obtain the corresponding image given by equation 1.37.

$$i(r,y) = \int_{-\infty}^{\infty} s_{ad}(r,y))\exp\left\{j2\pi\frac{f_c(y-u)^2}{cr_a}\right\}du = E_r(r-r_a)E_y(y-y_a)\sigma(r_a,y_a) \exp\left\{-j4\pi\frac{f_cr_a}{c}\right\} T_p\text{sinc}\left\{\frac{2K_rT_p}{c}(r-r_a)\right\}\Delta Y\text{sinc}\{K_y\Delta Y(y-y_a)\} \quad (1.37)$$

This processing chain is summarized in figure 1.9.

1.5.2 Focusing Multiple Points Response

A complex scene can be considered to be made up of a number of targets/point scatterers. The received signal can be described as the superposition of the signal received from all

[5] In the final synthesized image, point scatterers are represented by their fixed nearest slant-range position r, hence t is replaced by r and not the time-varying $d(y)$

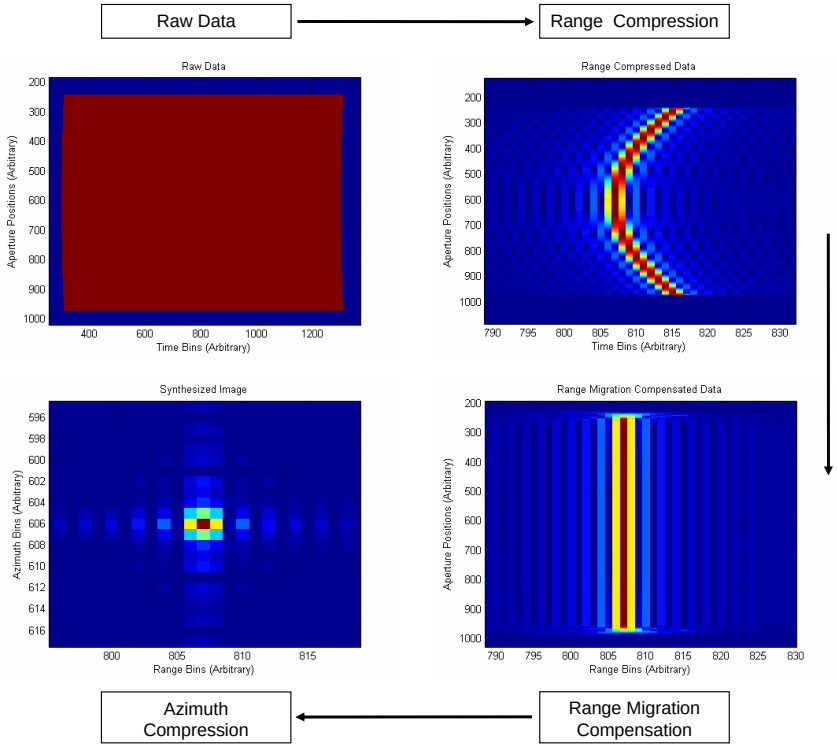

Figure 1.9: Example of Data Processing for a Single Point

these points and is given by the following expression:

$$s(t,y) = \sum_{m,n} E_y(y-y_n)\sigma(r_m,y_n)p\left(t - \frac{2\sqrt{r_m^2+(y-y_n)^2}}{c}\right) \tag{1.38}$$

Note that in this case, the process described in the previous section cannot be applied as range migration changes with scatterer positions, and each trajectory cannot be compensated individually without affecting the others.

The most straightforward and accurate technique to achieve image formation is the extension of matched filtering in two dimensions [2]. This can be carried out by filtering the received signal with the transmitted signal for each position. For a point given by position (r_a, y_a)[(6)], this is given as

$$i(r_a,y_a) = \int_{-\infty}^{\infty}\int_{-\infty}^{\infty} s(t,y)p^*\left(t - \frac{2\sqrt{r_a^2+(y-y_a)^2}}{c}\right)dtdy \tag{1.39}$$

Thus, this process is a two-dimensional integration, and takes care of all the three processing steps described in the preceding section. Note that for a fixed aperture position y,

[(6)] In this thesis, the position of a point scatterer is given by shortest slant-range position, azimuth position

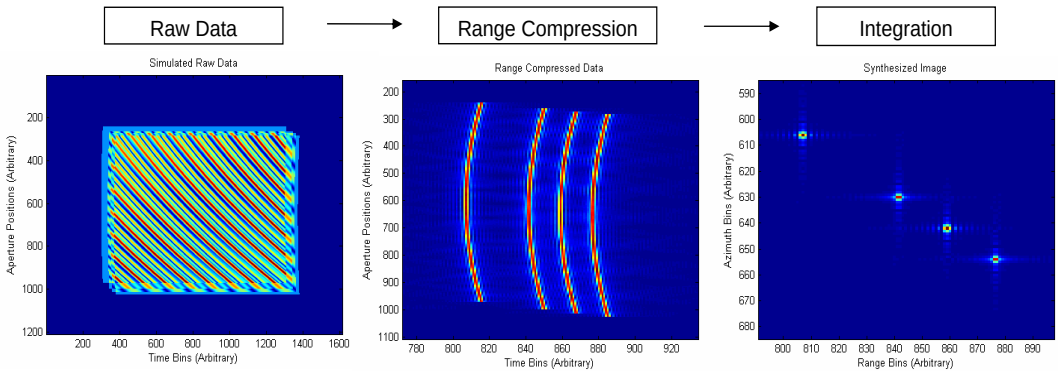

Figure 1.10: Example of Data Processing for Multiple Points

the above expression can be rewritten as

$$i(r_a, y_a) = \int_{-\infty}^{\infty} E_t\left(t - \frac{2\sqrt{r_a^2 + (y-y_a)^2}}{c}\right) E_y(y-y_a) \exp\left(-j4\pi f_c \frac{2\sqrt{r_a^2 + (y-y_a)^2}}{c}\right) \sigma(r_a, y_a) T_p \text{sinc}\left\{K_r T_p \left(t - \frac{2\sqrt{r_a^2 + (y-y_a)^2}}{c}\right)\right\} dy \quad (1.40)$$

that can be recognized as the integral of range-compressed signal along the aperture positions. Thus, the above expression may be modified as

$$i(r_a, y_a) = \int_{-\infty}^{\infty} s_{cd}\left(t - \frac{2\sqrt{r_a^2 + (y-y_a)^2}}{c}, y\right) dy \quad (1.41)$$

where $s_{cd}\left(t - \frac{2\sqrt{r_a^2+(y-y_a)^2}}{c}, y\right)$ is the range-compressed signal. By inspecting equation 1.41, it can be concluded that image at a certain point can be obtained by summing the range-compressed data along all the azimuth positions corresponding to that point. This process is known as the Backprojection algorithm [2] and is a standard time-domain image formation algorithm. Figure 1.10 shows an example of processing of data received from four point scatterers. The range compressed data illustrate the problem of range migration compensation. Even when there is not much difference in the range migration trajectories, each of them is centered at a different range and azimuth positions, which hampers the compensation procedure. Note that this image synthesis is exact and straightforward to implement. It constructs the final image gradually, for each sensor position [6]. Thus, there is a gradual improvement of resolution that can be useful for certain applications [6]. However, it suffers from two disadvantages:

- The integration is carried out in the discrete domain: In order to maintain accuracy, the range compressed signal should be upsampled, which increases the number of computations.

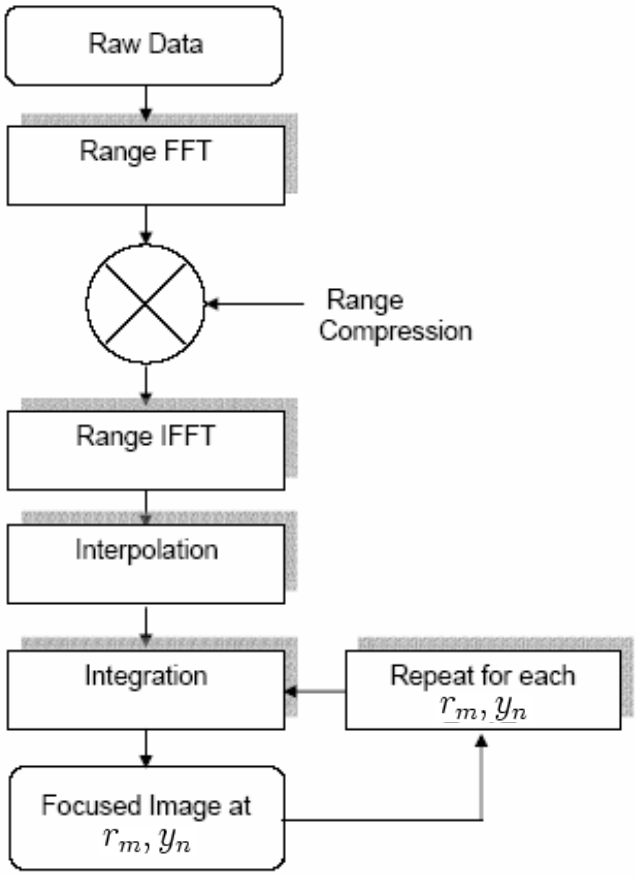

Figure 1.11: Block diagram of the Backprojection Algorithm (r_m and y_n represent the m^{th} range and n^{th} azimuth bin, respectively)

- The process has to be repeated for every range and azimuth position in the image. Thus, this process is computationally very intensive.

These disadvantages can be overcome by either dividing the data in subpatches and processing them in parallel (backprojection algorithm is suitable for parallel processing [6]) or carrying out the process in frequency domain. These frequency domain image formation/processing algorithms will be described in the next chapter.

Note
A realistic scene may be modeled as a collection of scatterers having a size comparable to the wavelength. The reflected field from each cell is the result of a "random walk", and provided the number of scatterers in each resolution cell is large, has real and imaginary parts that are independent, zero-mean, identically distributed gaussian variables [26]. This is called speckle and due to its presence, a SAR image can be considered to be composed of a random process.

1.6 Introduction to Polarimetry

An electromagnetic (EM) plane wave emitted by a sensor has time-varying Electric ($\overrightarrow{E}$) and Magnetic ($\overrightarrow{H}$) field components in a plane perpendicular to the direction of propagation. The two fields are orthogonal to one another, and described by Maxwell's equations using dielectric constant (or permittivity)-ϵ', permeability-μ' and conductivity-σ':

$$\nabla^2 \overrightarrow{E} + k^2 \overrightarrow{E} = 0 \tag{1.42}$$

where $k = \omega_c \sqrt{\epsilon' \mu'}$ is the wavenumber.

$$\nabla \times \overrightarrow{E} = j\omega_c \mu' \overrightarrow{H}. \tag{1.43}$$

For a plane wave propagating in the direction $\overrightarrow{k} = k\hat{k}$, the values of $\overrightarrow{E}$ and $\overrightarrow{H}$ at a position vector $\overrightarrow{r}$ are given as [18]

$$\overrightarrow{E}(\overrightarrow{r}) = \hat{E}_0 \exp(j \overrightarrow{k} \cdot \overrightarrow{r}) \tag{1.44}$$

$$\overrightarrow{H}(\overrightarrow{r}) = \hat{H}_0 \exp(j \overrightarrow{k} \cdot \overrightarrow{r}) \tag{1.45}$$

with

$$\hat{H_0} = \frac{1}{\eta} \hat{k} \times \hat{E_0} \tag{1.46}$$

and $\eta = \sqrt{\mu'/\epsilon'}$. Thus, the magnetic field component can be calculated from the electric field.

Polarization is a property of the EM waves that refers to the locus of the tip of the electric (or magnetic) field component of the wave "traced out" in a plane perpendicular to the direction of propagation. The two most common polarization basis are horizontal (H), and vertical (V) that can be used to create a wave with an arbitrary polarization, i.e.,

$$\overrightarrow{E^t}(\overrightarrow{r}) = E_h^t \overrightarrow{h} + E_v^t \overrightarrow{v} \tag{1.47}$$

Due to the backscattering properties of a scatterer, the polarization of the reflected wave can be different from the polarization of the incident wave and there can be four different combinations:

- HH - horizontal transmit and horizontal receive.
- VV - vertical transmit and vertical receive.
- VH - horizontal transmit and vertical receive.
- HV - vertical transmit and horizontal receive.

The first two combinations are known as co-polarized and the last two are known as cross-polarized channels. The backscattering properties can be completely described by a scattering matrix, S, which describes the transformation of the incident electrical field into the backscattered one as follows:

$$\begin{pmatrix} E_h^r \\ E_v^r \end{pmatrix} = \begin{pmatrix} S_{hh} & S_{hv} \\ S_{vh} & S_{vv} \end{pmatrix} \begin{pmatrix} E_h^t \\ E_v^t \end{pmatrix} \tag{1.48}$$

Normally, $S_{hv} = S_{vh}$, known as reciprocity that means the scattering matrix is symmetrical and has only 3 independent elements. The scattering properties may also be represented by a coherency vector using the Pauli spin elements as follows [34]:

$$k_T = \frac{1}{\sqrt{2}} \begin{pmatrix} S_{hh} + S_{vv} \\ S_{hh} - S_{vv} \\ 2S_{hv} \end{pmatrix} \tag{1.49}$$

Each element of this vector represents a particular scattering mechanism:

- $S_{hh} + S_{vv}$ - odd bounce scattering.
- $S_{hh} - S_{vv}$ - even bounce scattering.
- S_{hv} - even bounce with $\pi/4$ orientation or random volume scattering.

It is convenient to construct a power-domain representation of the scattering properties, which is done by forming the product of this vector with itself that results in the covariance matrix that also fully describes the scattering properties of a target [34].

$$T = E[k_T k_T^*]^{(7)} \tag{1.51}$$

In order to analyze the received data, a number of parameters may be computed for physical interpretation. One of these parameters is the co-polarized correlation coefficient. It is the average of the product between the complex amplitude of the HH channel and the conjugate of the complex amplitude of the VV channel. It is further normalized by the square root of the product of the powers in the HH and VV channels.

$$\gamma_p = \frac{E[S_{hh} S_{vv}^*]}{\sqrt{E[|S_{hh}|^2] E[|S_{vv}|^2]}} \tag{1.52}$$

Its magnitude and phase may be useful in classifying the scatterers as odd-bounce, even bounce, etc. Owing to the random nature of SAR images, and the reason that the correlation cannot be estimated from a single pixel [27], [28], the operation $E[.]$ should be carried out in a small subpatch/estimation area [27].

(7)

$$T = \frac{1}{2} E \begin{bmatrix} |S_{hh}|2 + 2\Re|S_{hh}S_{vv}^*| + |S_{vv}|^2 & |S_{hh}|2 - 2j\Im|S_{hh}S_{vv}^*| - |S_{vv}|^2 & 2S_{hh}S_{hv}^* + 2S_{vv}S_{hv}^* \\ |S_{hh}|2 + 2j\Im|S_{hh}S_{vv}^*| - |S_{vv}|^2 & |S_{hh}|2 - 2\Re|S_{hh}S_{vv}^*| + |S_{vv}|^2 & 2S_{hh}S_{hv}^* - 2S_{vv}S_{hv}^* \\ 2S_{hv}S_{hh}^* + 2S_{hv}S_{vv}^* & 2S_{hv}S_{hh}^* + 2S_{hv}S_{vv}^* & 4|S_{hv}|^2 \end{bmatrix} \tag{1.51}$$

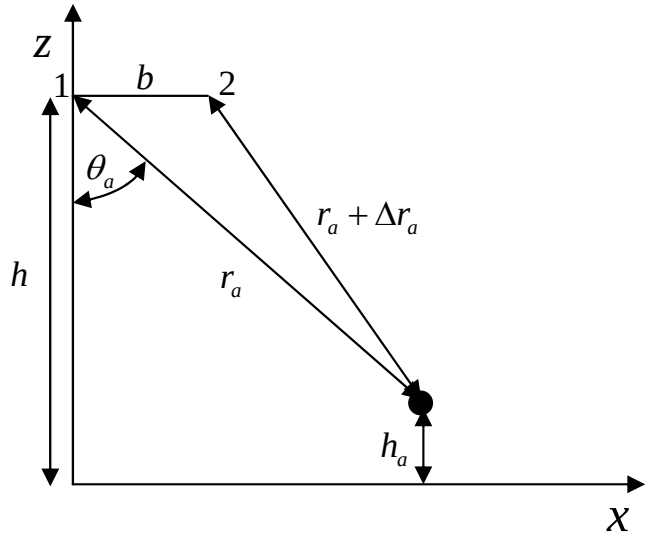

Figure 1.12: Interferometric Imaging Geometry

1.7 Introduction to Interferometry

Interferometric SAR (InSAR) is a technique used to calculate heights in an observed scene by acquiring data from two different sensor incidence angles. This can be carried out in two ways: Single-pass, which consists of two sensors mounted on the same platform thus gathering data from two angles in parallel, and dual-pass, which consists of a single sensor making acquisitions at two different times along two different trajectories. The difference between the sensor positions in both these cases is known as baseline (b), shown in figure 1.12. The acquired raw data (RD) is processed separately resulting in two focused images that are called master and slave images.

Considering a scene consisting of a single point at range and azimuth position of r_a and y_a, respectively, and having a height h_a, the corresponding data are given as:

$$s_1(t, y) = \sigma(r_a, y_a) p\left(t - \frac{2\sqrt{r_a^2 + (y - y_a)^2}}{c}\right) \tag{1.53}$$

$$s_2(t, y) = \sigma(r_a, y_a) p\left(t - \frac{2\sqrt{(r_a - \Delta r_a)^2 + (y - y_a)^2}}{c}\right) \tag{1.54}$$

The subscripts 1 and 2 represent master and slave configuration, respectively and Δr_a represents the difference of the location of the point in the master and slave images. This difference in case of dual-pass is [1]

$$\Delta r_a = b \sin \theta_a \tag{1.55}$$

whereas in case of single pass, it is halved [1]. If its value is known, the incidence angle θ_a can be calculated using equation 1.55 that may be used for calculation of height according to

$$h_a = h - r_a \cos\theta_a \tag{1.56}$$

Δr_a itself can be estimated by measuring the phase difference of the master and slave images. For demonstrating this, the corresponding focused images are described as follows:

$$i_1(r,y) = \sigma(r_a,y_a)\exp\left\{-j4\pi\frac{f_c r_a}{c}\right\}T_p\text{sinc}\left\{\frac{2K_rT_p}{c}(r-r_a)\right\}\Delta Y\text{sinc}\left\{K_y\Delta Y(y-y_a)\right\} \tag{1.57}$$

$$\begin{aligned} i_2(r-\Delta r_a,y) &= \sigma(r_a,y_a)\exp\left\{-j4\pi\frac{f_c(r_a-\Delta r_a)}{c}\right\}T_p\text{sinc}\left\{\frac{2K_rT_p}{c}(r-r_a+\Delta r_a)\right\} \\ &\quad \Delta Y\text{sinc}\left\{K_y\Delta Y(y-y_a)\right\} \end{aligned} \tag{1.58}$$

It is clear that the same point is located at a different location in both the images. In a complex scene, there is misalignment throughout whole of the master and slave images, and to rectify this, subpatches in the slave image are shifted such that they are at the same position compared to their counterparts in the master image. This is a very important step called coregistration [19], [20] and in order to measure the phase difference correctly, it should be carried out with sub-pixel precision [1]. After registration, the next step consists of multiplying the master image by the complex conjugate of the slave image that results in an interferogram that is written as (the bandwidth is assumed to be infinite and thus sinc functions are replaced by dirac pulses).

$$\mathrm{i}_{12}(r_a,y_a) = i_1(r_a,y_a)i_2^*(r_a-\Delta r_a,y_a) \tag{1.59}$$

The third step is to measure the phase of the product that is given as follows:

$$\phi_w(r_a,y_a) = \arg\mathrm{i}_{12}(r_a,y_a) = 4\pi\frac{f_c\Delta r_a}{c} \tag{1.60}$$

This phase difference is called wrapped phase as it is in the range of $-\pi$ to π, while the actual phase difference may be beyond this limit. Phase unwrapping techniques [1] may be used to recover the complete phase. However, before this step, a phase term corresponding to the flat earth is removed by multiplying equation 1.59 by $\exp(j4\pi\frac{f_c\Delta r_m}{c})|_{h_m=0}$ that facilitates the phase unwrapping process. The unwrapped phase $\phi(r_a,y_a)$ may be used to calculate the range difference Δr_a, and hence the height using equations 1.55 and 1.56. Figure 1.13 shows the ideal interferometric "fringes", as well as the phase for an azimuth position, before and after flat earth phase removal.

A measure for the quality of the interferogram is the correlation between the two images:

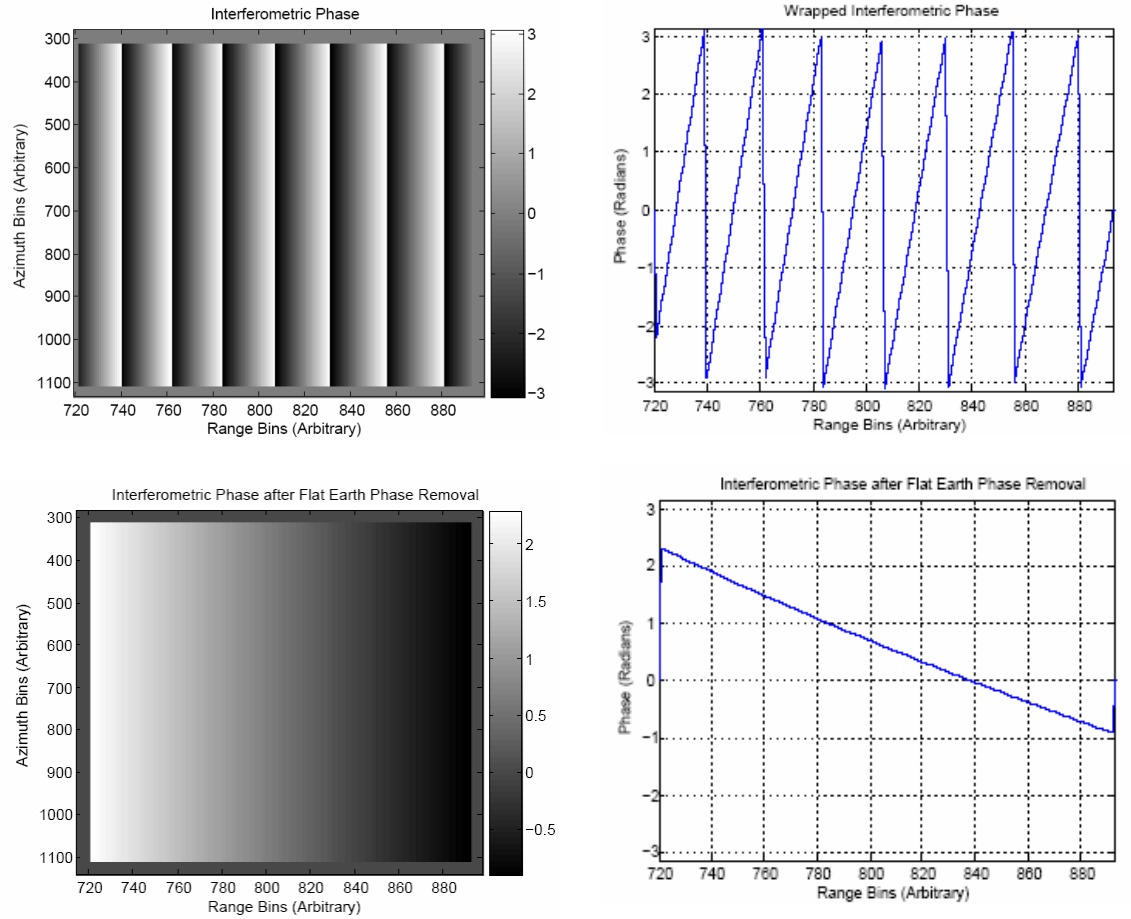

Figure 1.13: Interferometric Phase (before and after Flat Earth Phase Removal)

$$\gamma_i(r_m, y_n) = \frac{\mathrm{E}[i_1(r_m, y_n) i_2^*(r_m - \Delta r_m - \Delta r_r, y_n)]}{\sqrt{\mathrm{E}[|i_1(r_m, y_n)|^2]\mathrm{E}[|i_2(r_m, y_n)|^2]}} \tag{1.61}$$

Δr_r represents the misregistration error in the range direction. The amplitude of $\gamma_i(.,.)$ is between 0 and 1, where 0 means complete decorrelation (rendering any information retrieval impossible) and 1 means complete correlation, and its phase gives the interferometric phase. As mentioned previously, $E[.]$ should be carried out in a small subpatch.

Chapter 2

Frequency Domain SAR Image Formation

2.1 Outline of the Chapter

As described in the previous chapter, time domain processing represents the exact form of SAR image formation. However, it involves a very high calculation time and an alternative may be to perform the processing in the frequency [(1)] domain, which is described in this chapter. As a first step, expressions for the received SAR signal in different domains are presented, followed by an introduction to the principle of stationary phase. The Omega-k and the Chirp Scaling processing algorithms are also described alongwith examples using simulated data for a few points.

2.2 Introduction to Frequency Domain Processing

For the sake of convenience, the following substitutions will be used:

- **Carrier Wavenumber**
  $k_c = \frac{w_c}{c}$, where $w_c = 2\pi f_c$.
- **Transmitted Wavenumber**
  $k = k_c + \Delta k$, or $\Delta k = k - k_c$ where $\Delta k = \frac{\Delta w}{c}$ and $\Delta w = [-\pi B_t, +\pi B_t]$. B_t is the total bandwidth of the transmitted chirp signal in the across-flight direction.
- **Azimuth Wavenumber**
  $k_y = [-2k \sin\theta_{as}(\Delta Y/2), +2k \sin\theta_{as}(\Delta Y/2)]$, where ΔY is the aperture length/azimuth swath and $\theta_{as}(\Delta Y/2)$ is the maximum aspect angle, which is equivalent to half of the azimuth aperture angle θ_y.

The expressions in the transmitted wavenumber-azimuth/-azimuth wavenumber domain and 2D wavenumber domain for the received RD calculated using the Principle of Stationary Phase (POSP) (details are given in Appendix A) are given as

[(1)] The terms frequency and wavenumber are used interchangeably

$$S(k,y) = C_1 P(\Delta k) \sum_{m,n} \sigma(r_m, y_n) \exp(-j2k\sqrt{r_m^2 + (y-y_n)^2}) \tag{2.1}$$

where $P(\Delta k)$ is given by the Fast Fourier Transform (FFT) of the transmitted chirp signal in the transmitted time direction and is described as

$$P(\Delta k) = \exp\left(-j\frac{\Delta k^2 c^2}{4\pi K_r}\right) \tag{2.2}$$

$$S(k,k_y) = C_2 P(\Delta k) \sum_{m,n} \sigma(r_m, y_n) \exp\left(-jr_m\sqrt{4k^2 - k_y^2} - jy_n k_y\right) \tag{2.3}$$

$$\begin{aligned} S(t,k_y) &= C_3 \sum_{m,n} \sigma(r_m, y_n) \exp\left\{j\pi K(r_m,k_y)\left(t - \frac{2d(r_m,k_y)}{c}\right)^2\right\} \exp\{-j2k_c r_m a(k_y)\} \\ &\quad \exp(-jk_y y_n) \end{aligned} \tag{2.4}$$

where

$$d(r_m, k_y) = r_m(1 + b(k_y)) \tag{2.5}$$

is the radar-target distance in the azimuth-frequency domain and

$$K(r_m, k_y) = \frac{K_r}{1 - \{k_y^2 K_r \pi r_m)/(k_c^3 a^3(k_y) c^2\}} \tag{2.6}$$

with $b(k_y) = 1/a(k_y) - 1$ and $a^2(k_y) = 1 - (k_y/2k_c)^2$. C_1, C_2 and C_3 are all constant terms. Note that all these Fourier transforms are summation terms of $n = n_r n_y$ unique exponential functions, where n_r and n_y are the number of scatterer position in slant-range and azimuth directions, respectively. In order to process the data, a matched filter for each point in the frequency domain can be generated, which is the complex conjugate of the each of the above equations. The compressed image for each point can be obtained by multiplying the RD with a matched filter and taking an Inverse Fast Fourier Transform (IFFT-1D or 2D, depending on the equation) of the matched filtering operation result. In the following, image formation in different domains for every point in the imaged scene, using equations 2.1, 2.3 and 2.4 is discussed:

For the first equation, a matched filter has to be generated for each and every point consisting of different range and/or azimuth positions, e.g., a matched filter needed to focus a point at a position of r_a, y_a is

$$F_a(k,y) = P(\Delta k)^* \exp(j2k\sqrt{r_a^2 + (y-y_a)^2}) \tag{2.7}$$

The computational complexity for this equation can be decreased by dividing the RD in subpatches and generating a matched filter only for the center position of this subpatch.

The same applies to the remaining two equations. However, they show the presence of a linear phase in azimuth direction, which reveals an important characteristic useful for image formation: The matched filter will vary only with range position, as the linear phase in azimuth position enables focusing by means of a simple IFFT, thus increasing the computational efficiency. Equation 2.4 makes use of certain approximations, thus equation 2.3 will be considered further as it is more accurate. The matched filter for a position (r_m, y_n) is given as

$$F_m(k, k_y) = P(\Delta k)^* \exp\left(jr_m\sqrt{4k^2 - k_y^2} + jy_n k_y\right) \tag{2.8}$$

Equation 2.8 has to be changed for every range position in the image. As stated above, a subpatch approach can be used for processing [10]. It consists of dividing the RD in subpatches, and applying the matched filter for the center of each subpatch. Note that this method is approximate as the matched filter corresponds only to the center range position of each subpatch. A range mismatch of δr in the matched filter will lead to a phase error in the final processed image. In order to find an approximate limit of the size of the subpatch in the range direction, it is necessary to have an expression for the phase error that can be calculated by approximating the first exponential part in equation 2.8 as follows:

$$\exp\left(jr_m\sqrt{4k^2 - k_y^2}\right) \simeq \exp\left\{j2kr_m - \left(\frac{k_y^2}{4k_c}\right) r_m\right\} \tag{2.9}$$

The first part of the above exponential term will generate simply a linear phase in case of a mismatch, leading to a position shift, whereas the second part will generate a quadratic phase error in case of a range mismatch of δr leading to defocusing of the compressed image. A limit on the maximum allowed range mismatch (Δr) can be obtained by using the following relation:

$$\frac{k_y^2}{4k_c}|\Delta r| \ll 1 \tag{2.10}$$

$$\begin{aligned} |\Delta r| &\ll \frac{8\pi f_c/c}{(2\pi f_c \theta_y/c)^2} \\ |\Delta r| &\ll \frac{8\delta y^2}{\lambda_c \pi} \end{aligned} \tag{2.11}$$

and assuming $k_{ymax} \approx 2k_c \sin(\theta_y/2)$ and $\sin(\theta_y/2) \approx \theta_y/2$.

The subpatch size is $2|\Delta r|$ and decreases with an increase in azimuth resolution (δy) and carrier wavelength. The condition given by equation 2.10 is very restrictive and can be relaxed in order to gain computational efficiency at the expense of increased phase error.

In the following subsections, more accurate frequency domain processing algorithms will be presented, along with examples using the scene layout for nine point scatterers as shown

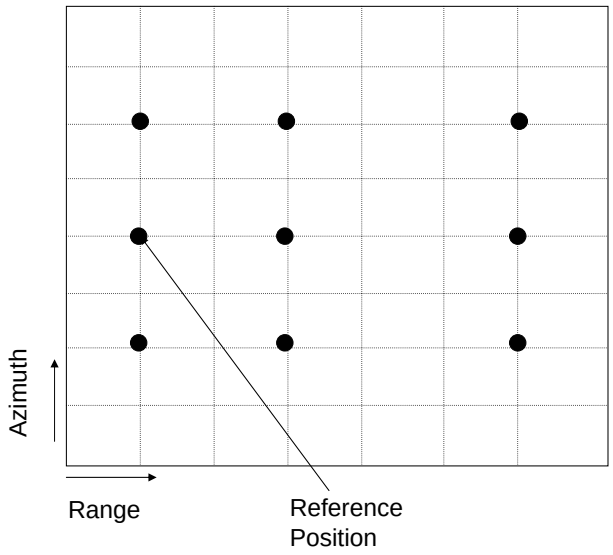

Figure 2.1: Scene Layout

in figure 2.1. Figure 2.2 shows the corresponding RD (generated using a time-domain simulator) that will be used to present the processing results.

2.3 The Omega-k Algorithm

The Omega-k algorithm (OKA) is the most exact form of frequency domain processing algorithms. It is carried out in the 2D wavenumber domain and allows the processing of very large azimuth aperture data [3], [5]. It is also known as wavefront reconstruction algorithm [2] or range migration algorithm [6]. [23] presents an approximate form of this algorithm that uses a parabolic approximation [24]. This approach can be derived using directly equation 1.4 or making an analogy with seismic signal processing (considering the exploding reflector's model as in [5]).

As a first step, the received RD is converted into 2D frequency domain[(2)]. A matched filter is generated for a reference position (r_{ref}, y_{ref}), which is given as follows:

$$F_{ref}(k, k_y) = P(\Delta k)^* \exp\left(jr_{ref}\sqrt{4k^2 - k_y^2} + jy_{ref}k_y\right) \text{ (3)} \tag{2.12}$$

The reference position is normally chosen to be at the center of the scene and thus $y_{ref} = 0$. This matched filter is multiplied with the 2D FT of the received data that focuses the points correctly for a reference range (on the left hand side). All the other points are partially focused and this defocusing increases with the distance from the reference range towards the right hand direction. The result of this operation is shown in range azimuth domain

[(2)] See subsection A.2.1

[(3)] In case of range compressed data, $F_{ref}(k, k_y) = \exp\left(jr_{ref}\sqrt{4k^2 - k_y^2} + jy_{ref}k_y\right)$

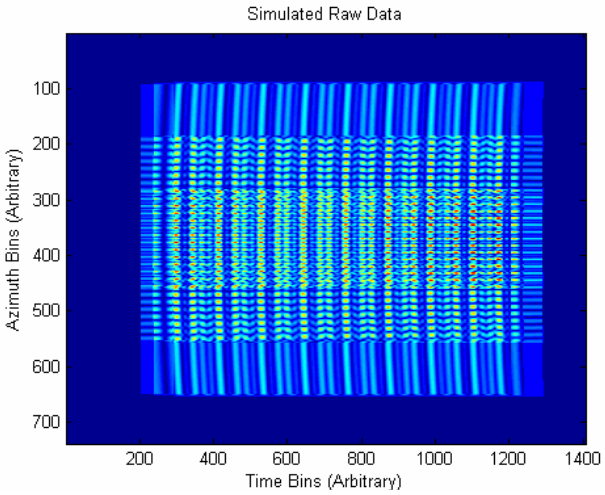

Figure 2.2: Simulated Raw Data used for Processing

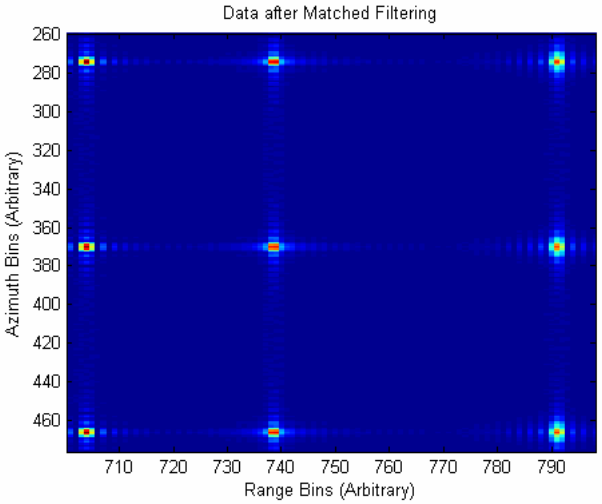

Figure 2.3: Data after Filtering matched to a Reference Position

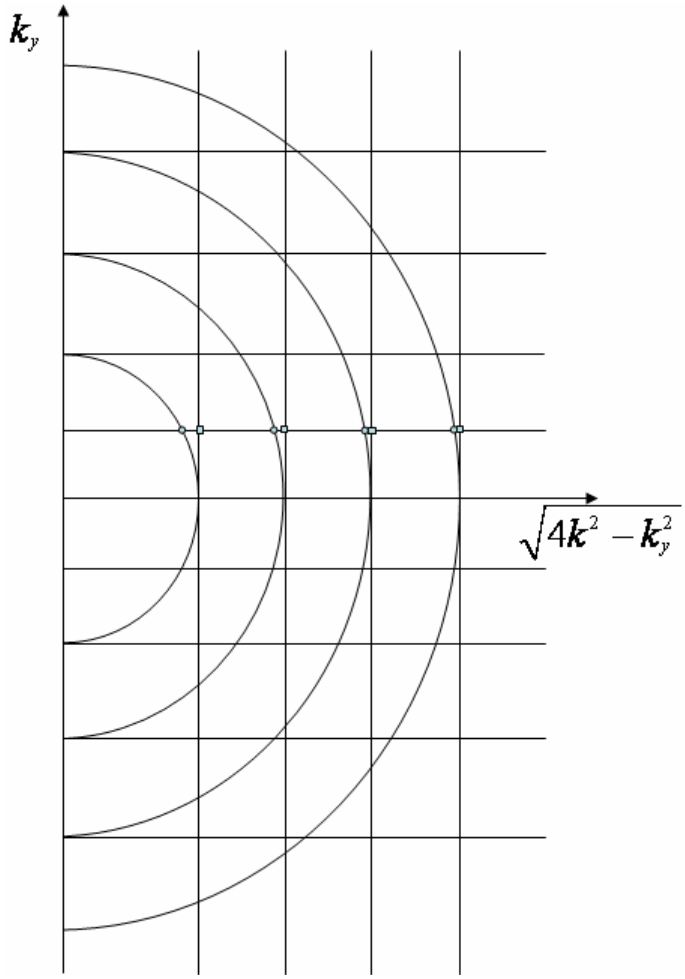

Figure 2.4: Stolt Interpolation

in figure 2.3 and given in equation 2.13.

$$\begin{aligned} S_1(k, k_y) &= S(k, k_y) F_{ref}(k, k_y) \\ &= C_2 |P(\Delta k)|^2 \sum_{m,n} \sigma(r_m, y_n) \exp\left(-j\sqrt{4k^2 - k_y^2}(r_m - r_{ref}) - j k_y y_n\right) \end{aligned} \tag{2.13}$$

It can be seen that point scatterers at the reference range are well focused, while for the other range positions, defocusing is evident. The next step is to interpolate $S_1(k, k_y)$ in the transmitted wavenumber direction, in order to focus the remaining points. This step is known as Stolt interpolation and converts the signal into a linear phase grating for scatterers at all ranges [6]. It is described as

$$k_r = \sqrt{4k^2 - k_y^2} \tag{2.14}$$

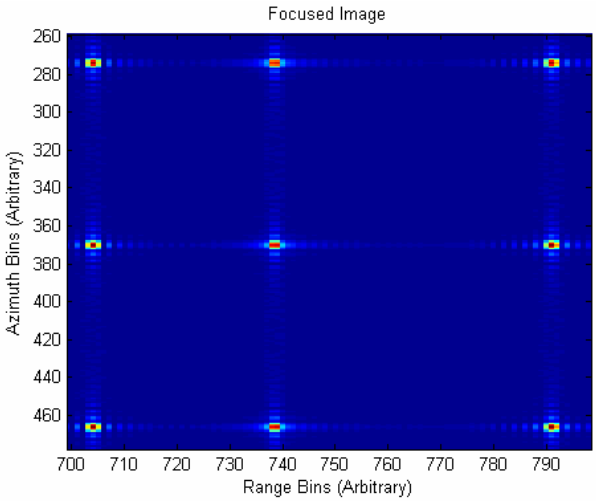

Figure 2.5: Focused Image

Thus, the signal is interpolated from unequally spaced $\sqrt{4k^2 - k_y^2}$ values to equally spaced k_r values as demonstrated in figure 2.4 resulting in

$$S_2(k_r, k_y) = C_2|P(\Delta k)|^2 \sum_{m,n} \sigma(r_m, y_n) \exp\left(-jk_r(r_m - r_{ref}) - jk_y y_n\right) \tag{2.15}$$

The data are non uniformly arranged in the horizontal direction as shown by the semi-circles and after the interpolation, they are arranged on the uniformly spaced vertical lines. The interpolated k_r values can be written as $k_r = 2k_c + 2\Delta k_r$ and a 2D IFT (Inverse Fourier Transform) gives the compressed SAR image that is shown in figure 2.5.

$$i(r, y) = C_4 \sum_{m,n} \sigma(r_m, y_n) \exp\{-j2k_c(r_m - r_{ref})\} \text{sinc}\left\{2B_r \frac{(r - r_m + r_{ref})}{c}\right\} \text{sinc}\{B_y(y - y_n)\} \tag{2.16}$$

where C_4 is a constant. The process is summarized by the block diagram shown in figure 2.6. Note that the interpolation (called Stolt interpolation) is a very important step that impacts the quality of the processed image. Moreover, for a correct inclusion of the interferometric phase in the image, the data should be multiplied by $\exp\{-j2k_c r_{ref}\}$.

There is another version of OKA that has been borrowed from seismic processing. It can be understood by considering the phenomenon of transmission and reception of an electromagnetic pulse, which is emitted from the radar, travels with a speed c to a scatterer and is reflected back. The same scenario can also be interpreted as the "explosion" of the scatterer after which the pulse travels from the exploded scatterer to the radar, traveling only one-way distance from the scatterer to the radar with half the speed $c/2$. This is known as the exploding reflectors model. It is widely used in seismic migration for removing distortions from reflection records by moving events to their actual spatial locations.

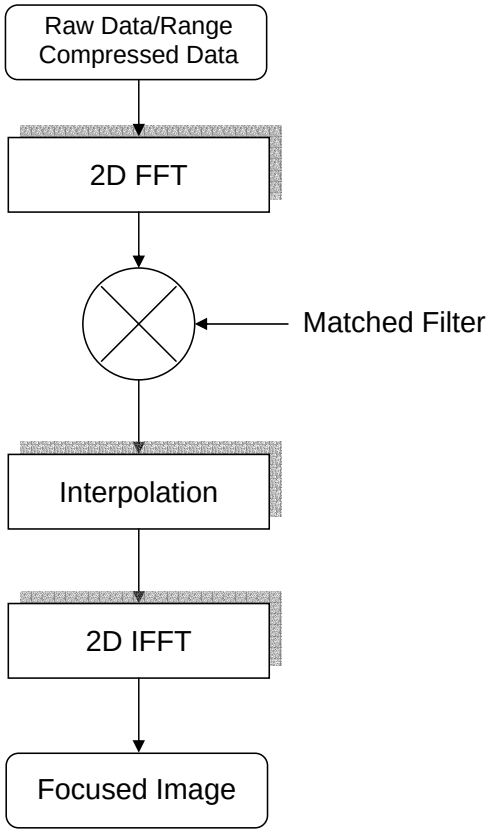

Figure 2.6: Block Diagram of the Omega-k Algorithm

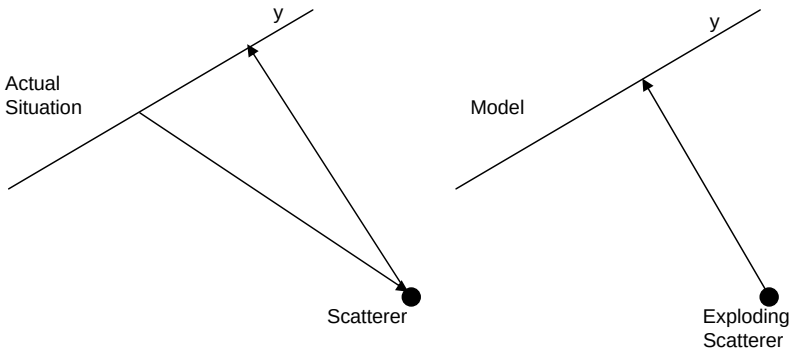

Figure 2.7: Exploding Reflector Model

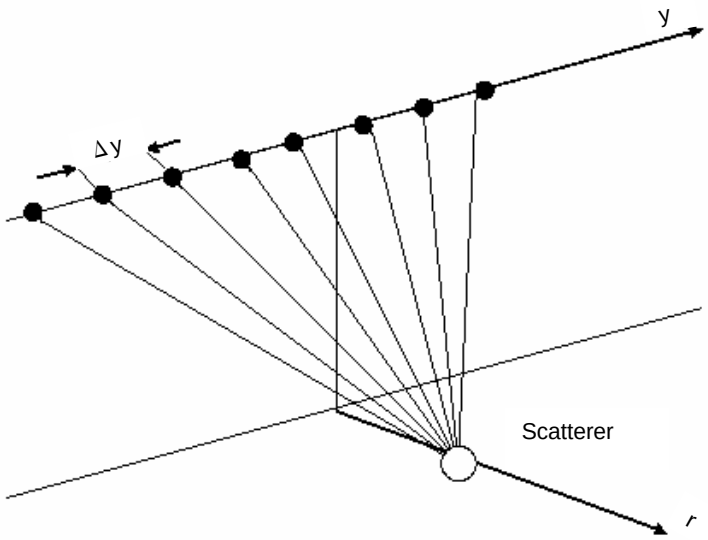

Figure 2.8: SAR Acquisition Geometry as a Network of Antennas

Considering the exploding reflectors model, the system can be considered as a network of antennas, which are situated along the flight path at a distance of $\Delta y = v_{SAR}/f_{PRF}$.

However, there are differences between this model and the actual situation. The first difference is that sensor motion during the pulse time of the flight has been neglected, i.e., it has been assumed that there is no movement during the transmission and reception. In reality, the transmitter travels a short distance during the pulse travel time and it also moves during the transmission and reception. The second difference is that the received signal amplitude in the case of the model is proportional to $1/r$ due to one-way propagation path, while in the actual case, it is proportional to $1/r^2$, where r is the sensor-target distance.

In the following, it is assumed that the RD is already compressed in the time direction. Its expression (assuming $r = 0$ at the sensor)is given as follows:

$$s_c(t, y) = \frac{1}{(2\pi)^2} \int \int S_c(\Delta\omega, k_y) \exp\{j(\Delta\omega t + k_y y)\} d\Delta\omega dt \tag{2.17}$$

where $S_c(\Delta\omega, k_y)$ is the 2D FT of the range compressed signal and $\Delta\omega$ is given as:

$$\Delta\omega = \frac{c}{2}\sqrt{k_r^2 + k_y^2} \tag{2.18}$$

In order to find the source values, we have to backpropagate the received signal to its location. This can be achieved by using phase shifts. For example, in order to backpropagate a signal to range r_0, the required phase shift (ϕ) is given by

$$\phi = k_r r_0 = \frac{2\omega}{c}\sqrt{1 - \frac{k_y^2}{(2\Delta\omega)^2}r_0} \tag{2.19}$$

With the help of this expression, the signal at range r can be expressed as

$$S_c(\Delta w, k_y)_r = S_c(\Delta w, k_y)\exp(jk_r r) \tag{2.20}$$

The corresponding signal in the time-azimuth domain for time $t = -t_0$ (The origin of time is taken as the time when the data collection starts, therefore, the time for the source explosion can be taken as the time corresponding to the minimum distance of the sensor from the scene) is given by

$$s(t = -t_0, y)_r = \frac{1}{(2\pi)^2}\int d(\Delta\omega)\int S_c(\Delta w, k_y)\exp\{j(-\Delta\omega t_0 + k_y y)\}\exp\{jk_r r\}dk_y \tag{2.21}$$

The above equation can be given the form of a 2D FT by the following change of variables:

$$\Delta\omega = \frac{c}{2}\sqrt{(2k_c + 2\Delta k_r)^2 + k_y^2} \tag{2.22}$$

that leads to

$$\begin{aligned} s(t = -t_0, y)_r &= \frac{1}{(2\pi)^2}\int d(\Delta k_r)\int S_c\left(\frac{c}{2}\sqrt{(2k_c + 2\Delta k_r)^2 + k_y^2}, k_y\right)\frac{c|2k_c + 2\Delta k_r|}{(2k_c + 2\Delta k_r)^2 + k_y^2} \\ &\quad \exp\left\{j\left(-\frac{c}{2}\sqrt{(2k_c + 2\Delta k_r)^2 + k_y^2}t_0\right)\right\}\exp\{jk_r r + jk_y y\}dk_y \end{aligned} \tag{2.23}$$

As a final step, the origin of the variable r is changed to the minimum sensor-target distance r_0 by means of the substitution $r' = r - r_0$, because it is useless to search for scatterers at a distance smaller than that due to their absence. The final expression is given as follows:

$$\begin{aligned} s(t = -t_0, y)_{r'} &= \frac{\exp(j2k_c r')}{(2\pi)^2}\int d(\Delta k_r)\int S_c\left(\frac{c}{2}\sqrt{(2k_c + 2\Delta k_r)^2 + k_y^2}, k_y\right)C(\Delta k_r, k_y) \\ &\quad \exp\left\{j(-\frac{ct_0}{2}\sqrt{(2k_c + 2\Delta k_r)^2 + k_y^2} - (2k_c + 2\Delta k_r)r_0)\right\} \\ &\quad \exp\{jk_r r' + jk_y y\}dk_y \end{aligned} \tag{2.24}$$

where $c(\Delta k_r, k_y) = \frac{c|2k_c + 2\Delta k_r|}{(2k_c + 2\Delta k_r)^2 + k_y^2}$. The main steps of this process are shown in figure 2.9.

Even though there are slight differences in processing steps for both these forms, they are shown to be more or less equivalent [24].

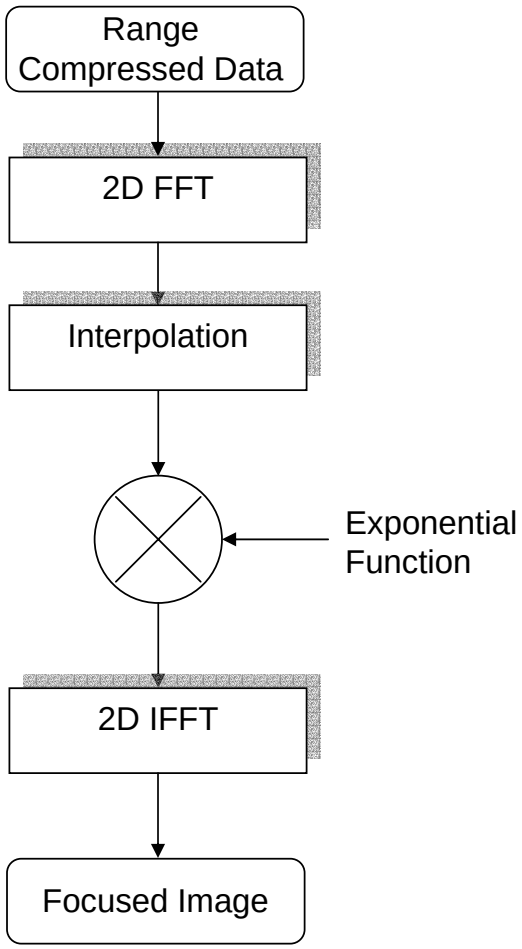

Figure 2.9: Block Diagram of the Alternative Form of Omega-k Algorithm

2.4 The Chirp Scaling Algorithm

Range Cell Migration (RCM) Compensation is an important and a complicated step in SAR image formation as the migration effect varies with the range position of each scatterer. If it can be equalized for all the possible range values, a single shift in the range direction is enough to compensate it. The Chirp Scaling algorithm (CSA) [4] achieves this by multiplying the SAR data in the azimuth-frequency time domain by a quadratic phase function (a chirp function), which changes the RCM to that of a reference range, thus equalizing the range cell migration.

The basic idea of CSA is curvature equalization, so that all of the RCM trajectories have the same curvature as that of a scatterer at a reference range. As this curvature is known at the reference range, it can be compensated by a phase multiplication. This curvature equalization is carried out in azimuth wavenumber time domain as, in this domain, range curvature depends only on the range position of the individual scatterers and

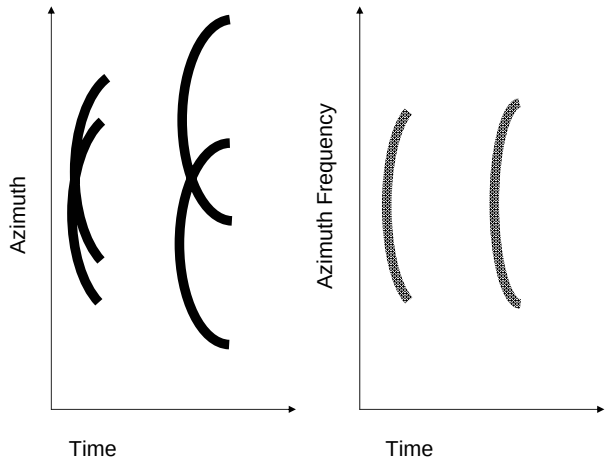

Figure 2.10: Range Migration Trajectory in Time Azimuth and Time Azimuth-Frequency Domains

is centered around the same frequency for different azimuth positions. This is elaborated in figure 2.10, where four RCM trajectories for scatterers at two different range positions are shown. In the time azimuth domain, they are centered at different positions, however, in 1D frequency domain, the trajectories of the scatterers at the same range position are overlapping, irrespective of their azimuth positions.

RCM for different nearest slant-range positions is depicted in figure 2.11. The solid lines show the actual range migration for three different range positions while the dotted lines show the modified range migration after curvature equalization. In order to equalize the trajectory curvature, it should be equal to $r_{ref}(r_m, f_c)$ at all the range positions.

This trajectory equalization can be achieved by considering the multiplication of two chirp signals of different chirp rates and different phase centers as described by equations 2.25 and 2.26. Note that the two chirps have phase centers of t_1 and t_2, respectively.

$$\text{chirp}_1 = \exp\{j\pi k(t-t_1)^2\} \tag{2.25}$$

$$\text{chirp}_2 = \exp\{j\pi ak(t-t_2)^2\} \tag{2.26}$$

$$\begin{aligned} \text{chirp}_1\text{chirp}_2 &= \exp\{j\pi k(t-t_1)^2\}\exp\{j\pi ak(t-t_2)^2\} \\ &= \exp\left\{j\pi k(1+a)(t-\frac{t_1+at_2}{1+a})^2\right\} \\ &\quad \exp\left\{j\pi k\frac{(1+a)(t_1^2+at_2^2)-(t_1+at_2)^2}{1+a}\right\} \end{aligned} \tag{2.27}$$

Thus it can be seen from the first term in equation 2.27 that the chirp rate and the phase center of the resulting signal have been modified to $k(1+a)$ and $\frac{t_1+at_2}{1+a}$, respectively. The second term is a residual phase that can be eliminated by simple multiplication. This concept can be used to equalize RCM by using a chirp signal to scale the signal in the

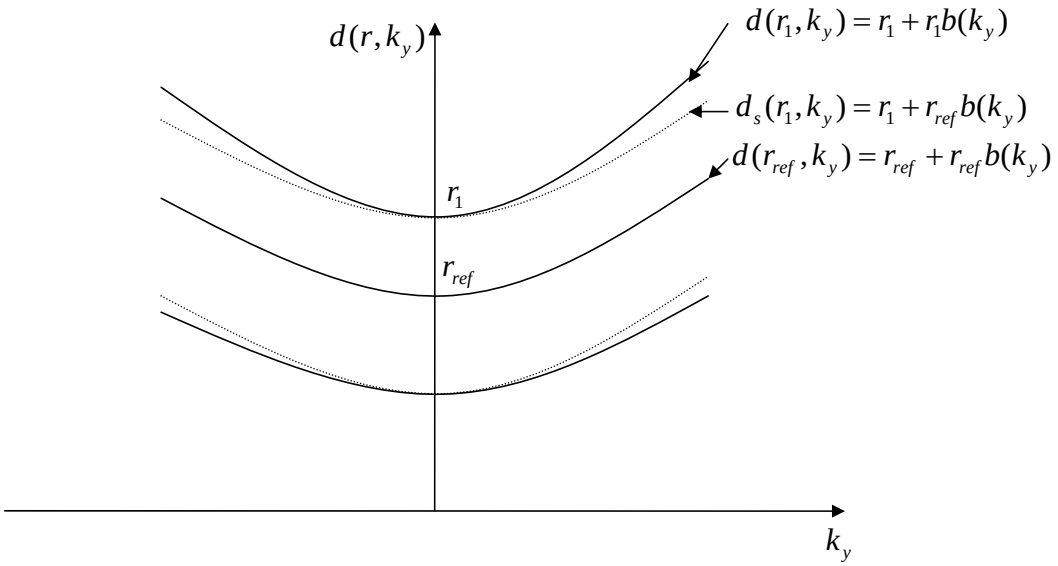

Figure 2.11: Equalization of Range Migration

slant-range direction.

Taking into account figure 2.11, it can be seen that the total trajectory after RCM compensation is given as $r + r_{ref}b(k_y)$. Using this concept, the phase multiplier required for trajectory equalization at a range position r_1 can be calculated as

$$\frac{t_1 + at_2}{1+a} = \frac{2}{c}\left\{r_1 + r_{ref}b(k_y)\right\} \tag{2.28}$$

Substituting $t_1 = \frac{2}{c}\left\{r_1 + r_1 b(k_y)\right\}$ and after some simple manipulations, the following expression for t_2 can be obtained:

$$t_2 = \frac{2}{c}\left\{r_{ref}\frac{b(k_y)}{a} + r_{ref}b(k_y) + r_1 - r_1\frac{b(k_y)}{a}\right\} \tag{2.29}$$

By choosing $a = b(k_y)$, the above expression can be simplified to

$$t_2 = \frac{2}{c}\left\{r_{ref} + r_{ref}b(k_y)\right\} \tag{2.30}$$

Using the above value, making use of the assumption $K(r,k_y) \approx K(r_{ref},k_y)$, the required phase multiplier to achieve trajectory equalization for a reference range is given by

$$F_{sc}(t,k_y) = \exp\left\{-j\pi K(r_{ref},k_y)b(k_y)\left(t - \frac{2d(r_{ref},k_y)}{c}\right)^2\right\} \tag{2.31}$$

Multiplying $S(t,k_y)$ in equation 2.4 by this function causes a time and azimuth-frequency dependent deformation of each range chirp phase structure so that all the signals follow

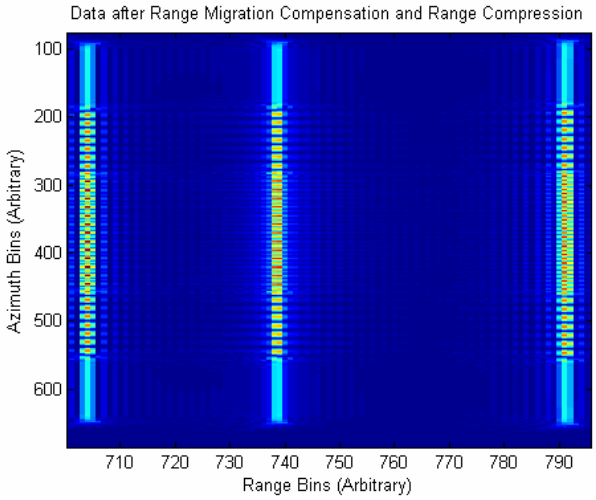

Figure 2.12: Data after Range Migration Compensation and Range Compression

the same reference trajectory. The next step is to take a FT in the range direction. The resulting expression in 2D frequency domain is

$$S_1(k, k_y) = C_5 \sum_{m,n} \sigma(r_m, y_n) \exp\{-j2k_c r_m a(k_y) - j\phi(r_m, k_y)\}$$
$$\exp\left\{ j \frac{c^2 b(r_m, k_y) \Delta k^2}{4\pi K(r_{ref}, k_y)} \right\} \exp\left[-j2\Delta k \left\{ r_m + r_{ref} b(k_y) \right\}\right] \tag{2.32}$$

where

$$\phi(r, k_y) = \frac{4\pi}{c^2} K(r_{ref}, k_y)(1 - a(k_y) \left(\frac{r - r_{ref}}{a(k_y)} \right)^2 \tag{2.33}$$

The third exponential term in equation 2.32 represents the range cell migration. It can be seen that due to chirp scaling, the curvature is $r_{ref} b(k_y)$, which has the same value for all ranges. Thus RCM can be compensated by applying a bulk shift to the scaled signal using the function given in equation 2.34.

$$F_{rcm}(k, k_y) = \exp\{j2\Delta k r_{ref} b(k_y)\} \tag{2.34}$$

The second exponential term in equation 2.32 represents the effective range chirp modulation with a modified chirp rate of $\frac{K(r_{ref})}{b_y}$. The range compression can be implemented by multiplying 2.32 by the function given by

$$F_{rc}(k, k_y) = \exp\left\{ -j \frac{c^2 b(k_y) \Delta k^2}{4\pi K(r_{ref}, k_y)} \right\} \tag{2.35}$$

An IFT (in the range direction as after RCM removal and range compression, time can be

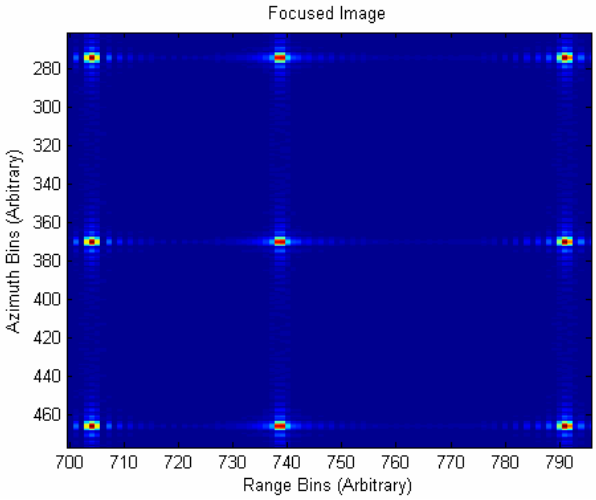

Figure 2.13: Focused Image

substituted by range positions) of the range migration compensated and range compressed data is shown in figure 2.12 and given as

$$S_2(r, k_y) = C_6 \sum_{m,n} \sigma(r_m, y_n) \exp(-j2k_c r_m a(k_y) - j\phi(r_m, k_y)) \text{sinc}\left\{2B_r \frac{(r - r_m)}{c}\right\} \quad (2.36)$$

The first exponential term represents the azimuth chirp and the residual phase arising due to the scaling operation. The term required for azimuth compression and the phase correction is given as

$$F_{acpc}(r, k_y) = \exp[+j2k_c r_m \{a(k_y) - 1)\} + j\phi(r_m, k_y)] \quad (2.37)$$

There is an extra term $\exp(-j2k_c r_m)$ in equation 2.37, needed because this phase term has been canceled during the processing operation [3]. Its "reinsertion" may be necessary for interferometric applications. The use of IFT in azimuth direction gives the required image shown in figure 2.13.

$$i(r, y) = C_7 \sum_{m,n} \exp(-j2k_c r_m) \sigma(r_m, y_n) \text{sinc}\left\{2B_r \frac{r - r_m}{c}\right\} \text{sinc}\{B_y(y - y_n)\} \quad (2.38)$$

The whole process is summarized by the block diagram given in figure 2.14. Note that the CSA requires the presence of chirp in the time direction, i.e., data without any range compression.

CSA is faster than OKA as the interpolation operation is carried out by exponential multiplications. However, this is at the cost of two approximations:

- Taylor series approximation in order to find the expression of the received signal in time azimuth-frequency domain. However, this approximation does not introduce considerable phase error in case of low resolutions [6].
- The second approximation is ignoring the dependence of range r on $K(r, k_y)$ for the scaling operation as well as range compression. The use of this approximation for range compression is one of the major sources of phase error. This phase error remains small if the scene size is small, as in this case, there is not a lot of variation of range values from the selected reference range. However, in the case of a large scene, this approximation is a major source of phase error and has to be compensated by using the Extended Chirp Scaling method [25].

Comments

The 2D spectrum for RD and for the focused image (produced using OKA or CSA) is shown in figure 2.15. It can be seen that the 2D spectrum is shifted in the range frequency direction. In order to take this shifting into account correctly avoiding any wrap around errors, the RD must be upsampled in the range direction. A typical upsampling factor is 1.1.

This shift is necessary in order to focus all the points in a scene. If there were a single scatterer in a scene, RD could have been focused using a matched filter for that point without any interpolation. In OKA, this shift is caused by Stolt interpolation given by equation 2.14, whereas, in CSA, this shift is approximated by a linear scaling and shift operation given by equations 2.31 and 2.37 [6].

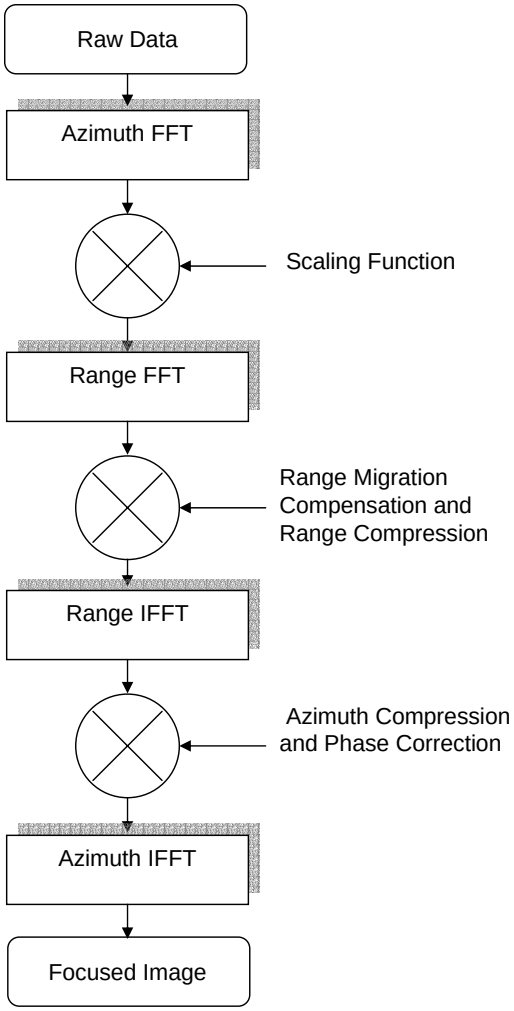

Figure 2.14: Block Diagram of the Chirp Scaling Algorithm

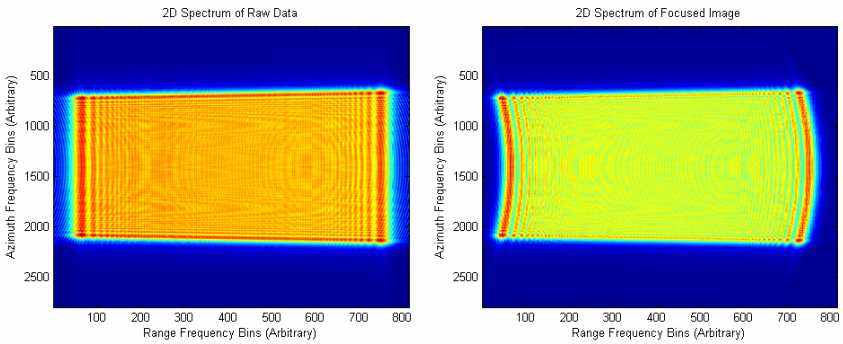

Figure 2.15: 2D Spectrum, before and after Interpolation

Chapter 3

SAR Raw Data Generation for Ideal Sensor Trajectories

3.1 Outline of the Chapter

This chapter concerns SAR RD simulation corresponding to ideal sensor trajectories, i.e., having no deviations from a straight path, for a scene containing single or multiple point scatterers. Two cases are considered: Static and moving points. In both cases, time domain simulation is described followed by the proposed efficient simulation schemes, that consist of a partial summation or 2D frequency domain multiplication, followed by interpolation. Different examples are presented, that compare the results of the proposed schemes with those of the reference time domain simulation. Analysis are also made to determine the computational complexity and accuracy of the proposed schemes, in cases where approximations are used.

3.2 Static Point Scatterers

3.2.1 Time Domain Raw Data Simulation

A scene can be divided into cells comprising a finite number of scatterers whose properties are given by an electromagnetic model [18] and described in a reflectivity map. SAR RD simulation can be carried out in a straightforward manner by using this reflectivity map and considering the following equation[(1)]:

$$s(t,y) = \sum_{m,n} \sigma(r_m, y_n) p\left(t - \frac{2\sqrt{r_m^2 + (y-y_n)^2}}{c}\right) \tag{3.1}$$

In words, the above equation can be described as the coherent summation of the transmitted chirp pulse delayed by the time corresponding to the position of each scatterer in a scene. The amplitude and phase of the scatterer are given by $\sigma(r_m, y_n)$ and multiplied by each pulse. This process is carried out for all the scatterers in the scene and for all the along-flight positions. In literature, this type of simulator has been presented by [29].

[(1)] Ignoring multipath effects

Table 3.1: Simulation Parameters (Stripmap SAR without any Squint)

Carrier Frequency	1.3 GHz	Center Slant Range	2611 m
Bandwidth	100 MHz	Sensor Velocity	100 ms^{-1}
Azimuth Aperture	4°	Sensor Height	2000 m
Scene Size (Ground Range)	400 m	Pulse Repetition Frequency	200 Hz
Scene Size (Azimuth)	400 m	Pulse Duration	5 μs

This simulation can be used for a few point scatterers as it is not difficult to deduce that it becomes computationally complex for a realistic scene consisting of a large number of scatterers. In order to quantify this complexity, a scene comprising of n_r and n_y pixels in the range and azimuth directions, respectively, is considered. From equation 3.1, it can be seen that RD computation consists of $n_r n_y$ summations of the transmitted pulses for one scatterer over all the aperture length. These pulses consist of n_t and n_a pixels in the time and azimuth directions, respectively, thus giving a computational complexity of $n_t n_a$ per scatterer, whence the total number of multiplications is given by $n_r n_y n_t n_a$. The block diagram of this time domain simulator is shown by figure 3.1.

In the next subsection, efficient frequency domain simulation schemes are described for a scene consisting of multiple point scatterers imaged with an ideal trajectory, i.e., having no platform deviations. Examples are also given by comparing the phases of RD generated by the proposed simulation schemes, and the time domain simulator ([31] uses the quality of final images for comparison, which can also be considered). The simulated RD is judged to be accurate enough, if this phase difference is less than $\pi/4$ radians (a coarse criterion based on the discussion in [3], [6]). The simulation parameters are shown in table 3.1.

3.2.2 Wavenumber Domain Raw Data Simulation

In order to carry out simulation in the wavenumber/frequency domain, the equations for RD in different wavenumber domains are recalled ignoring constant terms as well as range and azimuth envelopes:

$$S(k, y) = P(\Delta k) \sum_{m,n} \sigma(r_m, y_n) \exp\left\{-j2k\sqrt{r_m^2 + (y - y_n)^2}\right\} \tag{3.2}$$

$$S(k, k_y) = P(\Delta k) \sum_{m,n} \sigma(r_m, y_n) \exp\left(-j\sqrt{4k^2 - k_y^2} r_m - jk_y y_n\right) \tag{3.3}$$

$$\begin{aligned} S(t, k_y) &= \sum_{m,n} \sigma(r_m, y_n) \exp\left\{j\pi K(r_m, k_y)\left(t - \frac{2d(r_m, k_y)}{c}\right)^2\right\} \exp\{-j2k_c r_m a(k_y)\} \\ &\quad \exp(-jk_y y_n) \end{aligned} \tag{3.4}$$

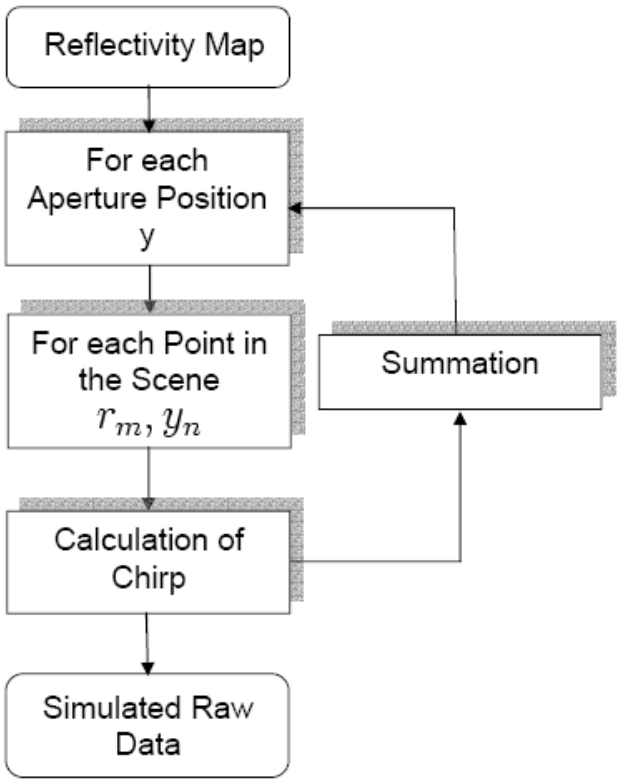

Figure 3.1: Block Diagram of the Time Domain Simulator (r_m and y_n represent the m^{th} range and n^{th} azimuth bin, respectively)

Equation 3.2 shows that in the transmitted wavenumber-azimuth domain, the RD generation consists of summation of $n_r n_y$ exponential terms. In any realistic configuration, there is no particular computational efficiency gain as compared to the time domain simulation.

Equations 3.3 and 3.4 have a similar feature related to the presence of an exponential term in the azimuth direction. The latter equation involves approximations, and hence it will no longer be considered.

3.2.2.1 Simulation with Partial Summation

The exponential term in equation 3.3 can be manipulated so that the summation process has to be carried out only for range positions. The summation process for all the azimuth positions at each range position can be replaced by a convolution operation that can be done efficiently using FFTs. This approach has been modified by [32], [33] for RD simulation in case of non-linear trajectories. [30], [31] also uses an approach of partial summation called a "hybrid" approach for spotlight SAR RD simulation. The formulation for this type of simulation is described by the next expressions.

The summation process in equation 3.3 can be rewritten by dividing the exponential in

two parts, i.e., a range position dependant part and an azimuth position dependant part.

$$S(k, k_y) = P(\Delta k) \sum_m \exp(-j\sqrt{4k^2 - k_y^2} r_m) \sum_n \sigma(r_m, y_n)\delta(r - r_m) \exp(-jk_y y_n) \quad (3.5)$$

where $\delta(.)$ represents a Dirac pulse. The reflectivity map or an ideal target function [2] can be considered as

$$\sigma(r, y) = \sum_{m,n} \sigma(r_m, y_n)\delta(r - r_m, y - y_n) \quad (3.6)$$

For a single range position r_m, equation 3.6 may be rewritten in azimuth wavenumber domain as

$$\Gamma(r_m, k_y) = \sum_n \sigma(r_m, y_n) \exp(-jk_y y_n)\delta(r - r_m) \quad (3.7)$$

where $\Gamma(r_m, k_y)$ is the 1D FT of the reflectivity map in azimuth direction. Thus equation 3.5 becomes

$$S(k, k_y) = P(\Delta k) \sum_m \exp\left(-j\sqrt{4k^2 - k_y^2} r_m\right) \Gamma(r_m, k_y) \quad (3.8)$$

It is evident that n_y summations (carried out by the second summation term in equation 3.5) have been replaced by an FFT resulting in computational savings. Figure 3.2 shows the block diagram for this simulation scheme. Its computational complexity[(2)] can be calculated by considering its main steps:

- 1D FFT of the reflectivity map for a range position r_m consisting of $n_y log_2(n_y)$ computations.
- Multiplication by $P(\Delta k) \exp\left(-j\sqrt{4k^2 - k_y^2} r_m\right)$ leading to $n_r n_y$ computations.
- Summation for all the range positions n_r giving a total number of $n_r\{n_r n_y + n_y \log_2(n_y)\}$ computations
- A 2D IFFT of the result of the summation taking $n_r n_y \log_2(n_r n_y)$ operations.

The approximate number of total multiplication operations is given by $n_r^2 n_y$, instead of $n_r n_y n_t n_a$ for a time domain simulator [33]. Since n_t is usually the same size or even greater than n_r, it is straightforward to observe that the computational savings are of the order of n_a. One point that should not be ignored is to consider the azimuth bandwidth to be limited as $k_y = [-2k \sin\theta_{as}(\Delta Y/2), +2k \sin\theta_{as}(\Delta Y/2)]$. This can be taken into account easily by multiplying $\exp\left(-j\sqrt{4k^2 - k_y^2} r_m\right)$ with an envelope function in the 2D

[(2)] Unless mentioned otherwise, the computations needed for the reflectivity map calculations are not considered, as this step is common for both time and frequency domain RD simulation

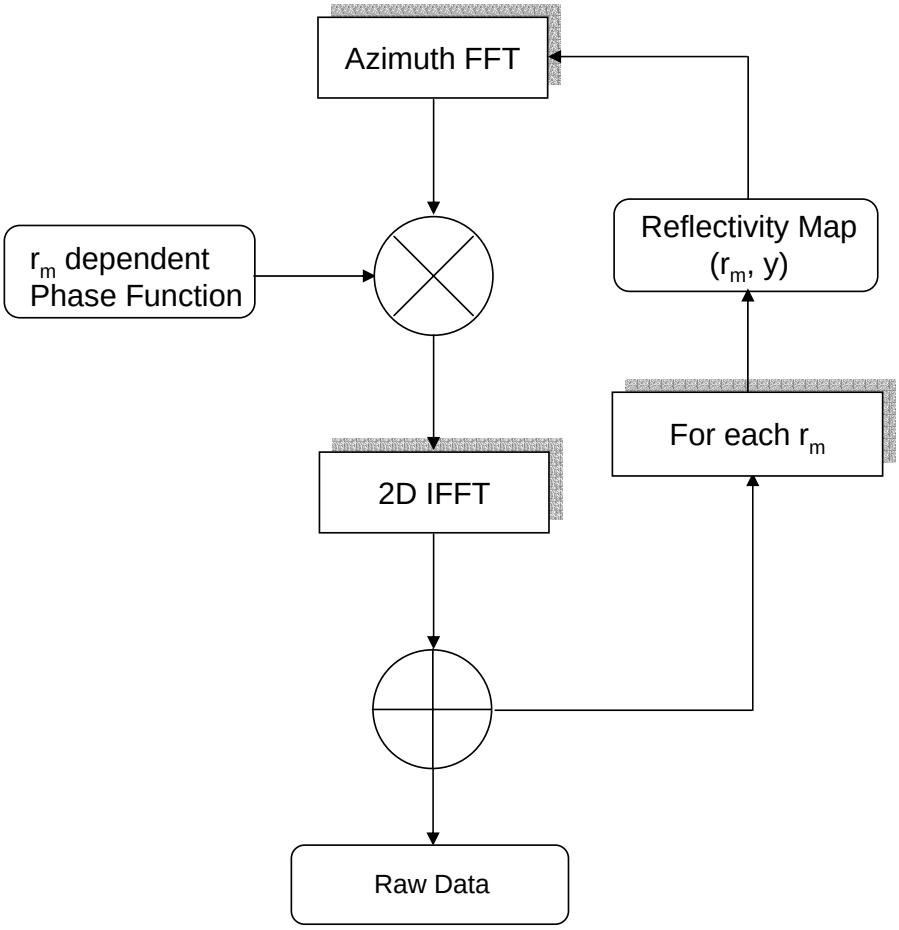

Figure 3.2: Block Diagram of the Partial Summation Simulator (r_m represents the m^{th} range bin)

wavenumber domain that is given as

$$f_e(k, k_y) = \text{rect}\left(\frac{k_y}{4k\sin(\theta_y/2)}\right) \tag{3.9}$$

for $k_c - \pi B_t/c \leq k \leq k_c + \pi B_t/c$. It has the form of a trapezium due to the transmitted wavenumber varying nature of the azimuth wavenumber. In order to compare the accuracy of the simulation, RD is generated for a point at the edge of the scene in range and azimuth by this method and the time domain simulator according to the parameters given in the preceding table. The resulting phase difference between the two RDs in the time and azimuth directions for selected bins are shown in figures 3.3 and 3.4. It can be seen that the error in time direction is very small, as an exact expression for the RD in the 2D wavenumber domain has been used. In the azimuth direction, the phase error is larger as the POSP is less exact at low TBP, which in this case is about 100. The phase error in

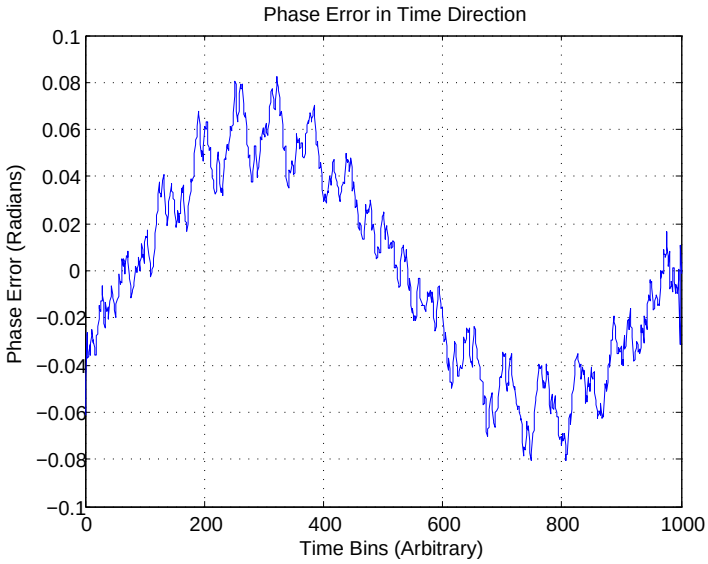

Figure 3.3: Phase Error in Time Direction

the azimuth direction for a higher aperture angle of 10°, and thus a higher TBP is shown in figure 3.5 that is overall much smaller (excluding the edges) than that in figure 3.4.

3.2.2.2 2D Wavenumber Domain Simulation

The above simulation improves the computational efficiency due to the use of 1D FFTs. If the summation operation can be further changed into a 2D FT formulation, the efficiency will be improved even further. This can be carried out by writing equation 3.3 as

$$S(k, k_y) = S_{ref}(k, k_y)\Delta S(k, k_y) \tag{3.10}$$

where

$$S_{ref}(k, k_y) = P(\Delta k)\exp(-j\sqrt{4k^2 - k_y^2}r_{ref}) \tag{3.11}$$

is a reference function and

$$\Delta S(k, k_y) = \sum_{m,n} \sigma(r_m, y_n)\exp\{-j\sqrt{4k^2 - k_y^2}(r_m - r_{ref}) - jk_y y_n\} \tag{3.12}$$

y_{ref} is assumed to be zero. By means of a change of variables, or Stolt interpolation described in the previous chapter, the preceding expression can be written as

$$\Delta S(k_r, k_y) = \sum_{m,n} \sigma(r_m, y_n)\exp\{-jk_r(r_m - r_{ref}) - jk_y y_n\} \tag{3.13}$$

that can be seen as a 2D FT of the reflectivity map (equation 3.6), multiplied by extra

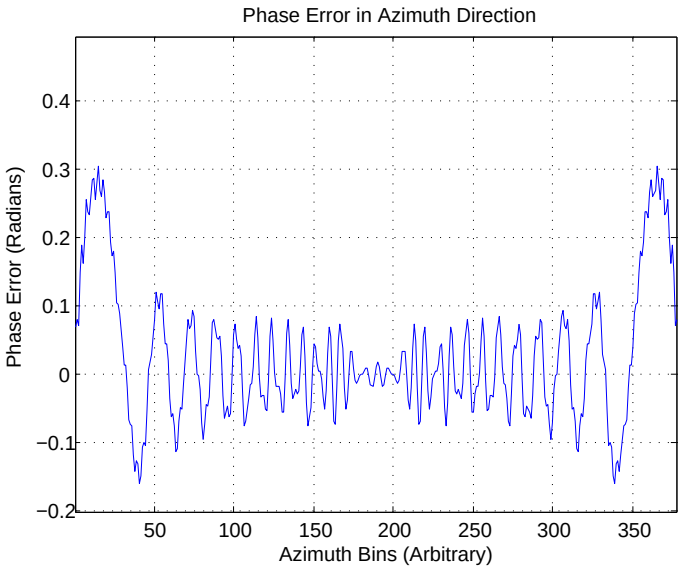

Figure 3.4: Phase Error in Azimuth Direction

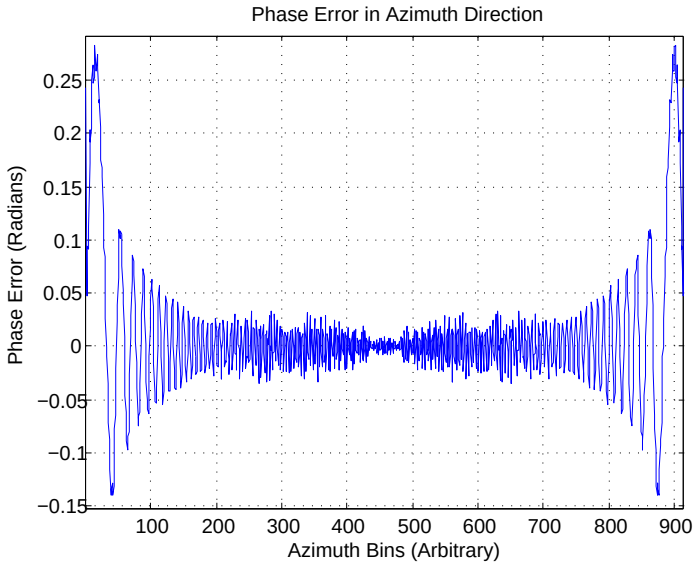

Figure 3.5: Phase Error in Azimuth Direction (10° Aperture)

term of $\exp\{j2k_c r_{ref}\}$ and the origin in the range axis shifted to the reference range shown below.

$$\Gamma(k_r, k_y) = \sum_{m,n} \exp\{-j2k_c(r_m - r_{ref})\}\sigma(r_m, y_n) \exp\{-j2\Delta k_r(r_m - r_{ref}) - jk_y y_n\} \quad (3.14)$$

Thus, RD simulation can be made more efficient by taking 2D FT of this modified reflectivity map, then interpolating it so that it is non-linearly sampled in the range wavenumber domain. This interpolation can also be seen as inverse Stolt interpolation. The resulting expression is multiplied with a reference function to generate RD[3] in 2D wavenumber domain as shown in equation 3.15.

$$S(k, k_y) = S_{ref}(k, k_y)\{\Gamma(k_r, k_y)\}_{k_r \to k} \quad (3.15)$$

As mentioned earlier, the bandlimiting effect of a SAR system should also be taken into account, by using an envelope in the 2D frequency domain. This is equivalent to multiplying equation 3.15 with the 2D FT of a reference image at the reference range and azimuth positions (this reference image can be generated either in the frequency domain by directly using equation 2.13 or in the time domain using a time domain simulator followed by processing with OKA) ,i.e.,

$$\Gamma'(k_r, k_y) = \Gamma(k_r, k_y) S_2(k_r, k_y)|_{r_m = r_{ref}, y_n = y_{ref} = 0} \quad (3.16)$$

where $S_2(k_r, k_y)$ given by equation 2.15, is the 2D FT of an image at positions (r_{ref}, y_{ref}). In fact this process[4] is more convenient and accurate as it already contains the effects of processing,and resembling the actual physical phenomenon of band-limiting in the time azimuth distance domain. Comparing equations 2.13 and 3.15, it can be seen that equation 3.15 actually describes Inverse Omega-k algorithm (IOKA), that leads to some comments: SAR image formation process performs compression of RD giving an image, and thus their inversion can generate RD from this image [86],[87] and [88]. [35], [36] present a space borne RD generator also based on this reasoning. However, a simulator's input is a reflectivity map, which cannot be used directly for RD generation by the inverse image formation algorithms. Bandlimiting effects have to be included in this reflectivity map and the process may be called phase inclusion (actually it is equivalent to the conversion of the reflectivity map to an image), carried out by equation 3.16. Moreover, this process gives the option of generating SAR images from a reflectivity map (besides RD simulation), that may be useful for certain applications.

The relationship between a reflectivity map and an image can also be seen by rewriting equation 2.38 as (ignoring the constant term)

$$i(r, y) = \exp(-j2k_c r)\sigma(r, y) \otimes_r sinc\left\{2B_r \frac{r}{c}\right\} \otimes_y sinc\{B_y y\} \quad (3.17)$$

that is a convolution of the reflectivity map with the bandlimiting factors given by the

[3] See subsection A.2.1

[4] $\Gamma'(k_r, k_y)$ should be used in place of $\Gamma(k_r, k_y)$ in equation 3.15

two sinc functions. Equation 3.17 is accurate as long as B_y is assumed to be constant for all the transmitted wavenumbers, otherwise, there is no equivalent convenient form in the distance domain. Due to this reason, it is not preferable to generate an expression for the reference image using this time domain representation.

This simulation scheme is shown in figure 3.6. Its computational complexity can be calculated by considering the steps involved in the above process:

- 2D FFT of the reflectivity map, the image and their multiplications consisting of $2n_r n_y \log_2(n_r n_y) + n_r n_y$ computations.
- Interpolation in the 2D frequency domain requiring $2(2M_{ker} - 1)n_r n_y$ operations, where M_{ker} is the length of a sinc interpolation kernel [3].
- Multiplication by $S_{ref}(k, k_y)$ that involves $n_r n_y$ operations.
- A 2D IFFT of the result taking $n_r n_y \log_2(n_r n_y)$ operations.

The total number of multiplications involved is given as $n_r n_y(3\log_2(n_r n_y) + 2(2M_{ker} - 1) + 2)$ giving a computational gain as compared to the time domain RD and partial summation approach. Examples are shown for the phase errors for a point at the center of the imaged scene (figures 3.7 and 3.8), as well as for a point at the edge of the scene (figures 3.9 and 3.10). It can be observed that although the phase errors are acceptable in both time and azimuth directions, for the former, the error increases at the edges compared to figure 3.3. This is mainly due to the phase inclusion process, followed by reference function multiplication ($S_{ref}(k, k_y)$). However, in azimuth direction, the error is smaller compared to figures 3.4 and 3.5, as, thanks to the phase inclusion operation, the effects of processing have been included (besides the bandlimiting operation), and IOKA simply reverses these effects. If this bandlimiting operation is carried out by an envelope (equation 3.9), some extra error may arise due to IOKA.

3.2.2.3 Approximate 2D Wavenumber Domain Simulation

Inverse Chirp Scaling algorithm (ICSA) may also be used for RD generation. [37] mentions the use of the scaling operation to replace the interpolation stage as it can be much faster. However, this operation requires a change in the whole formulation, and it is not possible to replace only the interpolation stage with a scaling process. Figure 3.11 shows the block diagram for this process, which consists of addition of range migration, as well as addition of range and azimuth chirps. Its computational complexity can be calculated by considering the steps involved in the above process:

- 2D FFT of the reflectivity map, the reference image, and their multiplication consisting of $2n_r n_y \log_2(n_r n_y) + n_r n_y$ computations.
- IFFT in the range direction, and azimuth decompression taking $n_r n_y \log_2(n_r) + n_r n_y$ computations.

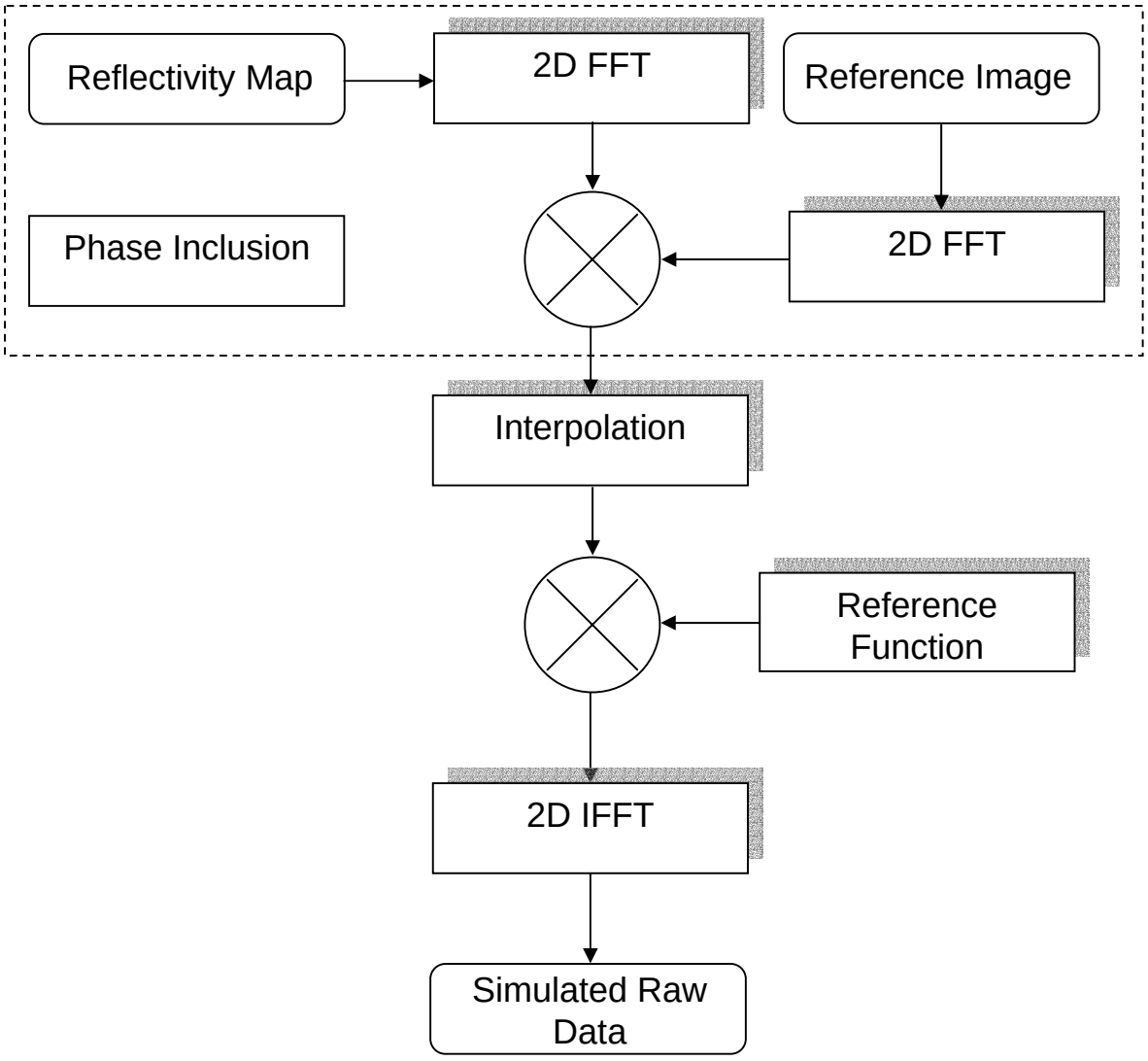

Figure 3.6: Block Diagram of the Inverse Omega-k Simulator

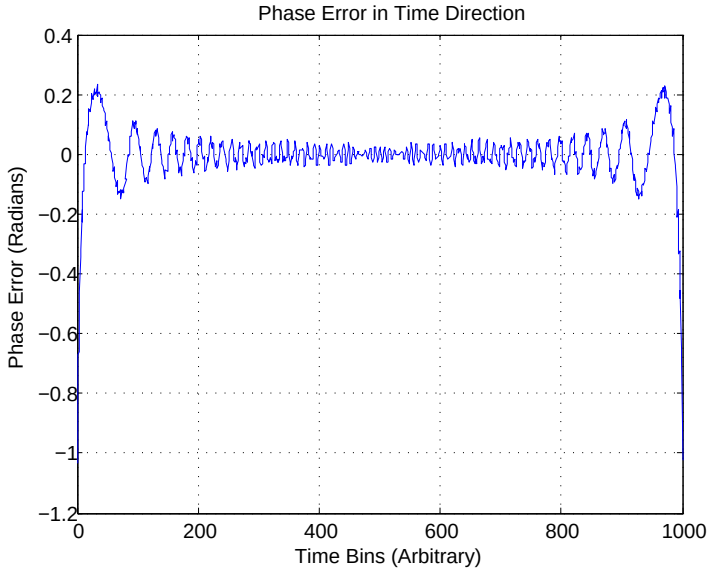

Figure 3.7: Phase Error in Time Direction (Center Point)

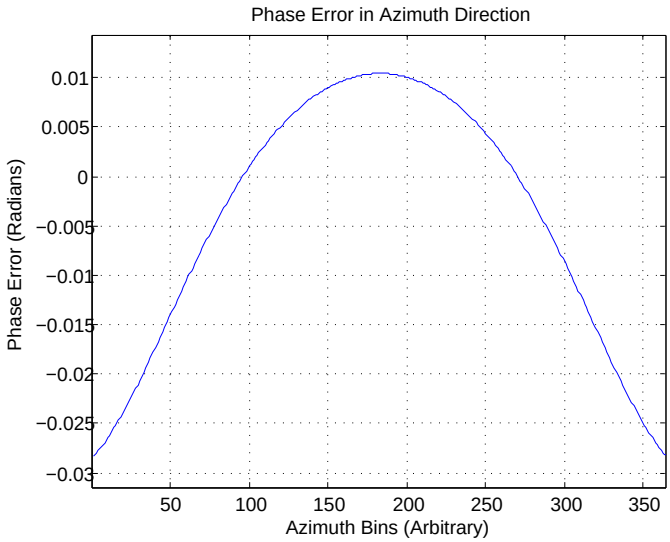

Figure 3.8: Phase Error in Azimuth Direction (Center Point)

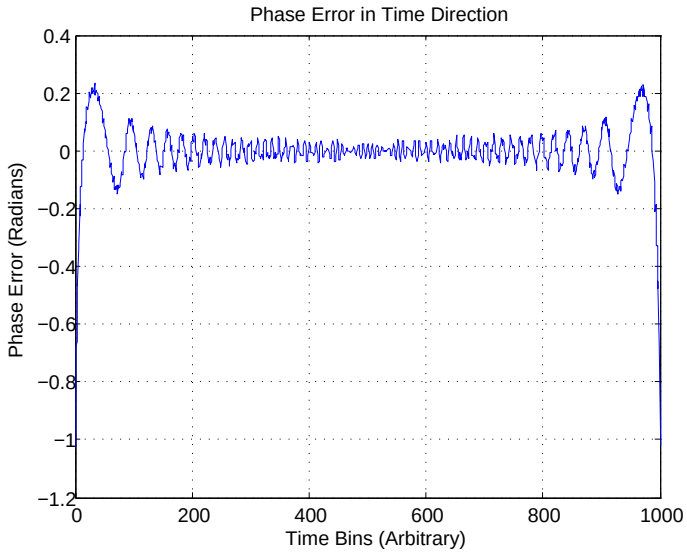

Figure 3.9: Phase Error in Time Direction (Edge Point)

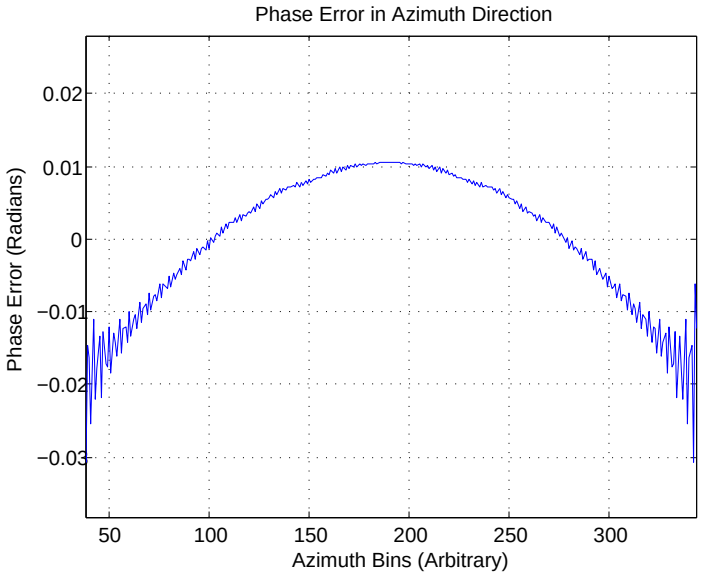

Figure 3.10: Phase Error in Azimuth Direction (Edge Point)

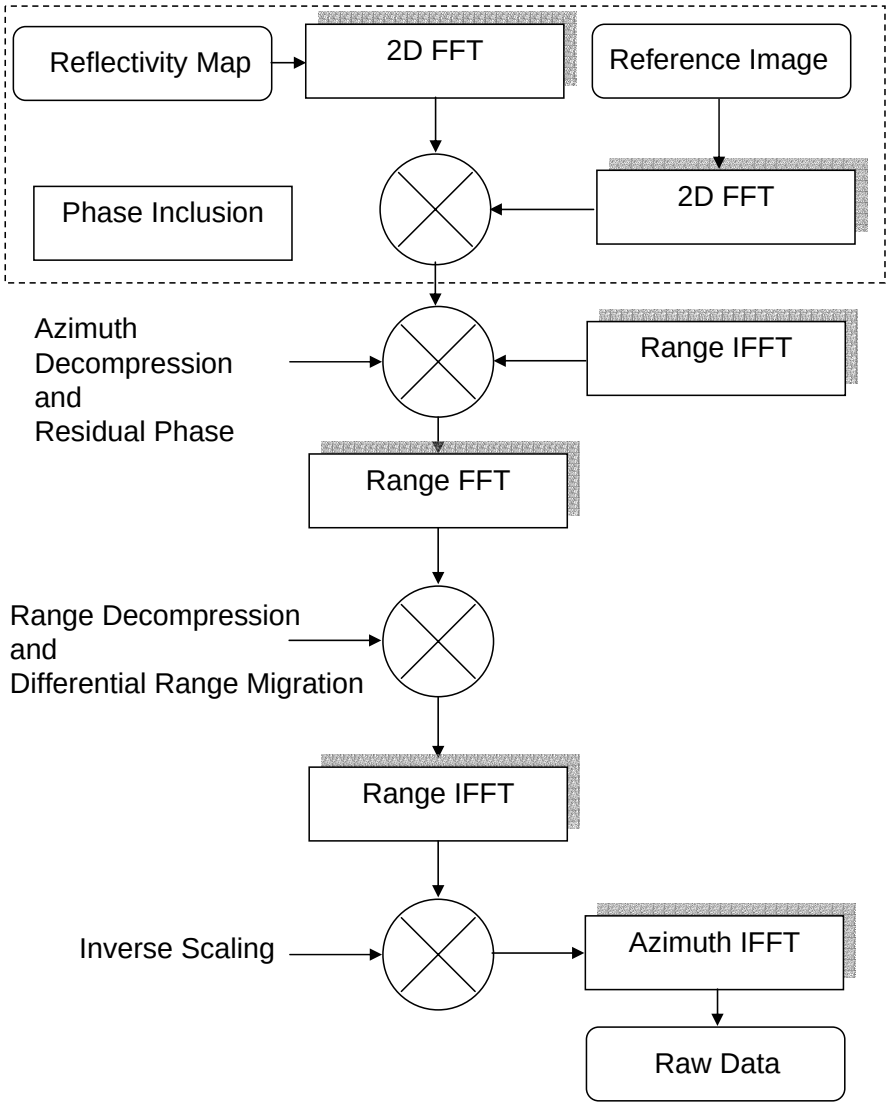

Figure 3.11: Block Diagram of the Inverse Chirp Scaling Simulator

- Range FFT and range decompression taking $n_r n_y \log_2(n_r) + n_r n_y$ computations.
- Time IFFT, followed by inverse scaling operation and finally azimuth IFFT resulting in $n_r n_y + 2 n_r n_y \log_2(n_r)$ operations.

The total number of multiplications are $n_r n_y (2\log_2(n_r n_y) + 4 + 3\log_2(n_r) + \log_2(n_y))$ that are less than those by the IOKA simulator. However, it should not be ignored that this is due to two main approximations:

1. Ignoring the dependance of distance on the modified chirp rate $K(r, k_y)$.
2. Approximating the Stolt interpolation.

These approximations affect the "quality" of the simulated RD (Note that IOKA does not involve any of these approximations and thus gives a very accurate form of RD). The effects due to these approximation should be quantized in order to find the validity domain of ICSA for RD simulation. For that purpose, the phase error effects arising as a result of these approximations will be expressed in terms of the scene and system parameters.

Approximation 1

The modified chirp rate for a range position r_m is described in an approximate but convenient form as

$$\begin{aligned} K(r_m, k_y) &= \frac{K_r}{1 - (k_y^2 K_r \pi r_m / k_c^3 a^3(k_y) c^2)} \\ &\approx K_r + \frac{K_r^2 k_y^2 \pi r_m}{k_c^3 a^3(k_y) c^2} \end{aligned} \tag{3.18}$$

This rate is assumed to be constant for all range positions. The range phase error that can arise due to ignoring the dependence of $K(r_m, k_y)$ on a change of range position of Δr is given by the product of Δr with the derivative of equation 3.18 (with respect to r) and the transmitted time. The maximum phase error $\Delta\phi_r$ arises over half the transmitted pulse length T_p [3] and is given as

$$\begin{aligned} \Delta\phi_r &= \left| \frac{dK(r_m, k_y)}{dr} \Delta r \right| (\frac{T_p}{2})^2 \\ &= \left| \frac{K_r^2 k_y^2 \pi}{k_c^3 a^3(k_y) c^2} \Delta r \right| (\frac{T_p}{2})^2 \end{aligned} \tag{3.19}$$

In order for the phase error to be negligible, i.e. $\Delta\phi_r \ll 1$, the limit on Δr is

$$\Delta r \ll \frac{4 k_c^3 c^2 a^3(k_y)}{T_p^2 K_r^2 k_y^2 \pi} \tag{3.20}$$

Considering only the maximum value of k_y that is approximated by $2k_c \sin\theta_y/2$, $a(k_y) \approx 1$ and $K_r = \frac{B_t}{T_p}$, the limit comes out to be

$$\begin{aligned} |\Delta r| &\ll \frac{k_c c^2}{T_p^2 K_r^2 \sin^2(\theta_y/2)\pi} \\ &\ll \frac{k_c c^2}{B_t^2 \sin^2(\theta_y/2)\pi} \end{aligned} \tag{3.21}$$

Approximation 2

The Stolt interpolation can be approximated by expanding the square root term in the exponential function $\exp\left(-j\sqrt{4k^2 - k_y^2} r_m\right)$ till second order terms. After some manipulations given as

$$\begin{aligned} \sqrt{4k^2 - k_y^2} &= \sqrt{4k_c^2 - k_y^2}\sqrt{1 + \frac{4\Delta k^2}{4k_c^2 - k_y^2} + \frac{8k_c\Delta k}{4k_c^2 - k_y^2}} \\ &\approx \sqrt{4k_c^2 - k_y^2}\left[1 + \frac{1}{2}\left\{\frac{4\Delta k^2}{4k_c^2 - k_y^2} + \frac{8k_c\Delta k}{4k_c^2 - k_y^2}\right\} - \frac{1}{8}\left\{\frac{4\Delta k^2}{4k_c^2 - k_y^2} + \frac{8k_c\Delta k}{4k_c^2 - k_y^2}\right\}^2\right] \\ &\approx \sqrt{4k_c^2 - k_y^2}\left[1 + \frac{2\Delta k^2}{4k_c^2 - k_y^2} + \frac{4k_c\Delta k}{4k_c^2 - k_y^2} - \frac{8k_c^2\Delta k^2}{(4k_c^2 - k_y^2)^2}\right] \end{aligned}$$

the result is

$$\sqrt{4k^2 - k_y^2} \approx \sqrt{4k_c^2 - k_y^2} + \frac{4k_c\Delta k}{\sqrt{4k_c^2 - k_y^2}} - \frac{2k_y^2\Delta k^2}{(4k_c^2 - k_y^2)^{3/2}} \tag{3.22}$$

In case of ICSA, all the terms after the first order term are ignored (similar to CSA). Note that the interpolation serves to correctly defocus all the points away from the reference point, thus any approximation in this process will lead to a phase error in the simulated RD. This phase error increases with the distance Δr from the reference range and can be expressed as

$$\Delta\phi_s = \left| 2\frac{k_y^2\Delta k^2}{(4k_c^2 - k_y^2)^{3/2}}\Delta r \right| \tag{3.23}$$

In order for the effects of this defocusing to be small, one needs $\Delta\phi_s \ll 1$ and thus

$$2\frac{k_y^2\Delta k^2}{(4k_c^2 - k_y^2)^{3/2}}|\Delta r| \ll 1 \tag{3.24}$$

This leads to an expression on the limit of Δr given by

$$|\Delta r| \ll \frac{(4k_c^2 - k_y^2)^{3/2}}{2k_y^2\Delta k^2} \tag{3.25}$$

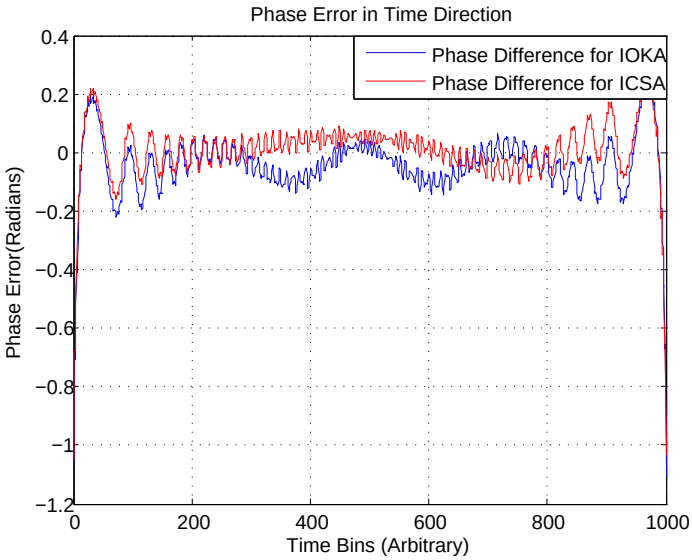

Figure 3.12: Comparison of Phase Errors in Time Direction

Using $4k_c^2 - k_y^2 \approx 4k_c^2$, $k_y = 2k_c \sin(\theta_y/2)$ and maximum value of $\Delta k = \pi B_t/c$, the preceding expression changes to

$$|\Delta r| \ll \frac{k_c c^2}{\sin^2(\theta_y/2)\pi^2 B_t^2} \tag{3.26}$$

Figures 3.12 and 3.13 present the difference between the phase errors for simulated RD for a point placed at a distance of 1350 m from the scene center for the IOKA and ICSA based simulators. It is clear that in the azimuth direction, the latter simulator does not generate accurate RD, as the quadratic phase errors shown in equations 3.21 and 3.26 increase with respect to the azimuth bins. Note that this error varies with the position of a point in the scene.

An efficient frequency domain RD simulator is presented in [11], however, it ignores the first order term and thus there is an additional phase error in this case given by

$$\Delta\phi_s = \left| \frac{4k_c \Delta k}{\sqrt{4k_c^2 - k_y^2}} \Delta r \right| \tag{3.27}$$

Using the constraint

$$\left| \frac{4k_c \Delta k}{\sqrt{4k_c^2 - k_y^2}} \Delta r \right| \ll 1 \tag{3.28}$$

leads to the following limit on Δr:

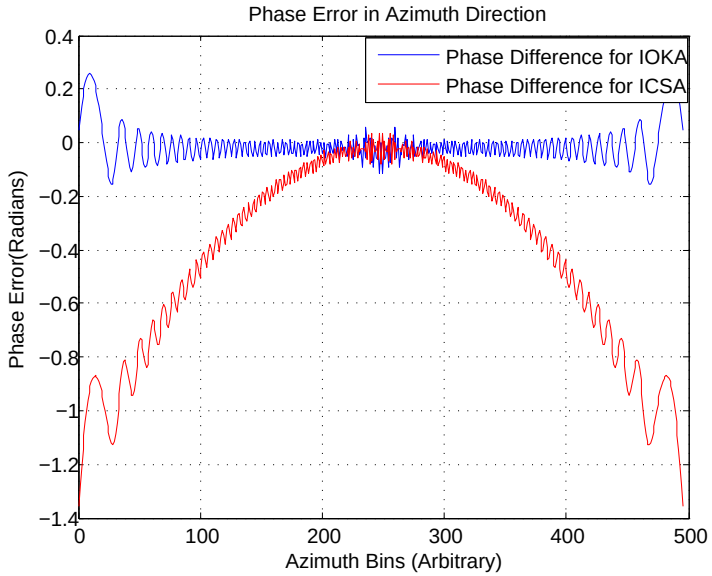

Figure 3.13: Comparison of Phase Errors in Azimuth Direction

$$|\Delta r| \ll \frac{c}{2\pi B_t} \tag{3.29}$$

that is very restrictive and cannot be used for large scene sizes.

3.3 Moving Point Scatterers

3.3.1 Time Domain Raw Data Simulation

In case of a moving point target, the acquired RD for a single point a at a position (r_m, y_n), moving with a slant-range velocity v_{rm} and an azimuth velocity of v_{yn} can be written in time, azimuth-time (τ) as

$$s_a(t,\tau) = \sigma(r_m, y_n) p\left(t - \frac{2\sqrt{(r_m - v_{rm}\tau)^2 + (v_{sar}\tau - y_n - v_{yn}\tau)^2}}{c}\right) \tag{3.30}$$

For time domain simulation, there is no difference as compared to simulation for static point scatterers as it is simply a summation process shown by the next equation.

$$s(t,\tau) = \sum_{m,n} \sigma(r_m, y_n) p\left(t - \frac{2\sqrt{(r_m - v_{rm}\tau)^2 + (v_{sar}\tau - y_n - v_{yn}\tau)^2}}{c}\right) \tag{3.31}$$

As in the preceding section, time domain simulation is used as a reference for comparing the RD simulated by the proposed scheme that follows.

3.3.2 Wavenumber Domain Raw Data Simulation

Equation 3.30 can be rewritten in time azimuth domain as

$$s_a(t,y) = \sigma(r_m, y_n) p\left(t - \frac{2\sqrt{(r_m - \mathbf{v_{rm}}y)^2 + (y - y_n - \mathbf{v_{yn}}y)^2}}{c}\right) \tag{3.32}$$

where $y = v_{sar}\tau$, $\mathbf{v_{rm}} = v_{rm}/v_{sar}$ and $\mathbf{v_{yn}} = v_{yn}/v_{sar}$ are the normalized velocities in range and azimuth directions, respectively.

The case of RD simulation for moving point scatterers in frequency domain can be examined by considering equation 3.32 in transmitted wavenumber azimuth domain, given by

$$\begin{aligned} S(k,y) &= C_1 P(\Delta k) \sum_{m,n} \exp\left[-j2k\sqrt{\{r_m - \mathbf{v_{rm}}(y - y_n)\}^2 + \{y - y_n - \mathbf{v_{yn}}(y - y_n)\}^2}\right] \\ &\quad \sigma(r_m, y_n) \end{aligned} \tag{3.33}$$

The radar-target distance $d_{mov}(y)$ in this case can be approximated by [39], [40]

$$d_{mov}(y) \approx r_m - \mathbf{v_{rm}}(y - y_n) + \left\{\frac{(1 - \mathbf{v_{yn}})(y - y_n)^2}{2r_m}\right\} \tag{3.34}$$

that leads to two main effects:

- A change in location of the scatterer in the azimuth direction of $\Delta y = r_a \mathbf{v_{rm}}$ due to the exponential term
$$\exp(j2k\mathbf{v_{rm}}y) \tag{3.35}$$
that creates a shift in azimuth wavenumber of $\Delta k_y = 2k\mathbf{v_{rm}}$
- A defocusing due to the exponential term
$$\exp\left\{-j2k\frac{(1 - \mathbf{v_{yn}})y^2}{2r_m}\right\} \tag{3.36}$$

There may be an extra defocusing in range direction due to a changed range cell migration. These effects are demonstrated in figure 3.15 for RD corresponding to the scene layout shown in figure 3.14. There are four scatterers at the same azimuth but different range positions. One of them is static, whereas others are moving in range, azimuth or both range-azimuth directions, shown by a vertical, horizontal or both vertical and horizontal arrows, respectively. The scatterer having a range velocity is displaced from its position in the synthesized image with small defocusing, whereas the one having an azimuth velocity is completely defocused. The 4^{th} scatterer having both range and azimuth velocities is displaced as well as defocused. Note that the difference between radar target distance for a moving point target and a static one can be written as:

$$\Delta d(y) = d_{mov}(y) - d(y) \tag{3.37}$$

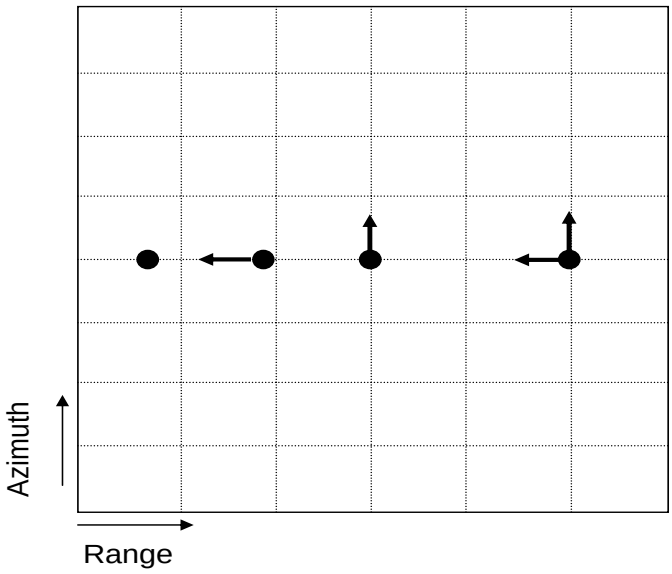

Figure 3.14: Scene Layout for Simulation Example

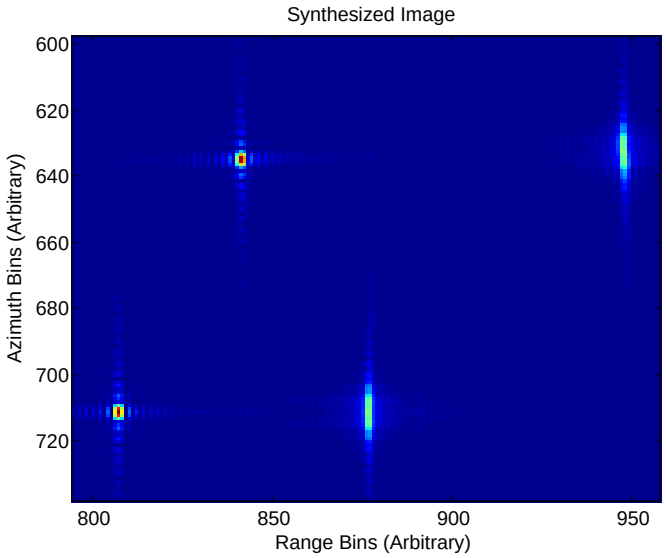

Figure 3.15: Synthesized Image

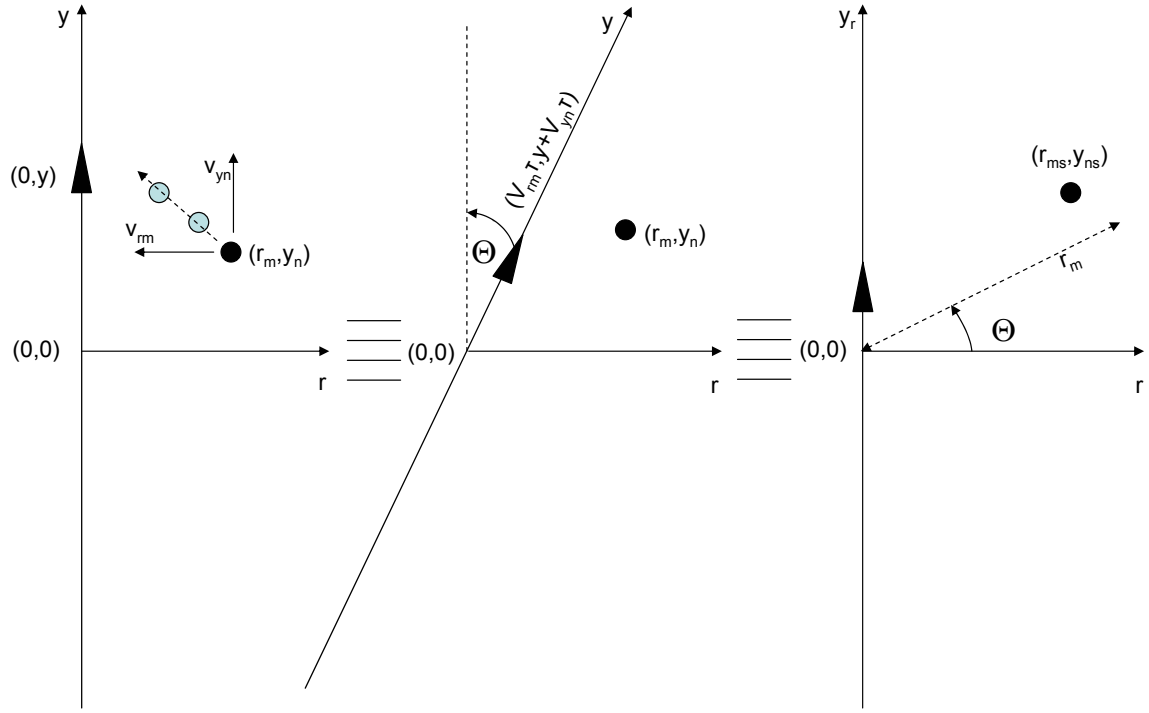

Figure 3.16: Change of Geometry for a Moving Point

Thus, RD of a single moving point scatterer can be generated from that of a static point scatterer by multiplying the latter by

$$\psi(k, y) = \exp\{-j2k\Delta d(y)\} \tag{3.38}$$

However, in case of multiple moving point targets, RD for each individual point scatterer have to be multiplied by an individual phase term and then added together. This holds no advantage as compared to time domain simulation.

By using some constraints, it may be possible to generate RD for multiple moving points in the frequency domain. As a first step, only points in the azimuth direction but at one range position having the same slant-range and azimuth velocity are considered. In this case, RD for moving or static points can be interrelated to one another by means of re-sampling and a change of axes [38]. This change of axes can be formulated by considering that a moving target and a straight sensor trajectory can be considered equivalent to a static target and a sensor having a velocity component of $\mathbf{v_{rm}}$ and $\mathbf{v_{yn}}$, in the slant-range and azimuth directions, respectively. By considering a further rotation by an angle Θ of the axes, the new configuration is shown in figure 3.16. This operation rotates and scales different components as

$$r_{ms} = r_m \cos\Theta + y_n \sin\Theta \tag{3.39}$$

$$y_{ns} = -r_m \sin\Theta + y_n \cos\Theta \tag{3.40}$$

$$\Theta = \arctan\left\{\frac{\mathbf{v_{rm}}}{1-\mathbf{v_{yn}}}\right\} \tag{3.41}$$

$$y_s = y\sqrt{\mathbf{v_{rm}}^2 + (1-\mathbf{v_{yn}})^2} \tag{3.42}$$

$$k_{ys} = \frac{k_y}{\sqrt{\mathbf{v_{rm}}^2 + (1-\mathbf{v_{yn}})^2}} \tag{3.43}$$

Equation 3.33 can be rewritten as

$$S(k,y) = C_1 P(\Delta k)\sigma(r_m, y_n)\exp\left\{-j2k\sqrt{r_{ms}^2 + (y_r - y_{ns})^2}\right\} \tag{3.44}$$

whereas, in 2D frequency domain, the expression is

$$S(k,k_{ys}) = C_2 P(\Delta k)\sigma(r_m, y_n)\exp\left(jr_{ms}\sqrt{4k^2 - k_{ys}^2} + jy_{ns}k_{ys}\right) \tag{3.45}$$

The modified range wavenumber is given as

$$k_{rs} = \sqrt{4k^2 - k_{ys}^2} \tag{3.46}$$

This can be seen as a squint-mode geometry that causes an azimuth phase shift of $2k\sin\Theta$ [38], besides modifications given by equations 3.39-3.43 and 3.46,that can be carried out by interpolations. IOKA can be used for this process by employing the modified reference function given by

$$S_{rref}(k,k_{ys}) = P(\Delta k)\exp\left(-jr_{refs}\sqrt{4k^2 - k_{ys}^2} - jy_{refs}k_{ys}\right) \tag{3.47}$$

where r_{refs} and y_{refs} are given by equations 3.39 and 3.40. The block diagram in figure 3.17 shows this process. Its computational complexity is the same for an IOKA simulator, except for two extra interpolations, resulting in a total number of $n_r n_y(3\log_2(n_r n_y) + 6(2M_{ker}-1)+2)$ multiplications, that may be less than the time domain simulator, depending on the number of simulated points.

This technique can be used for simulating RD for an object moving with a linear velocity and having a small size in the range direction. All the points in the object are considered to have the same velocity, however, the same ground velocity for points at different range position is mapped to different slant-range velocity for each point, thus limiting the size in the range direction. To find out this limit on the size, consider the geometry in figure 3.18 that shows a point (part of an object) moving with a velocity v_{xm} in the ground range direction. The relationship between v_{rm} and v_{xm} is given as

$$v_{rm} = v_{xm}\sin\theta \tag{3.48}$$

Consider another point (on the same object) at a ground range distance of $x + \Delta x$ (and

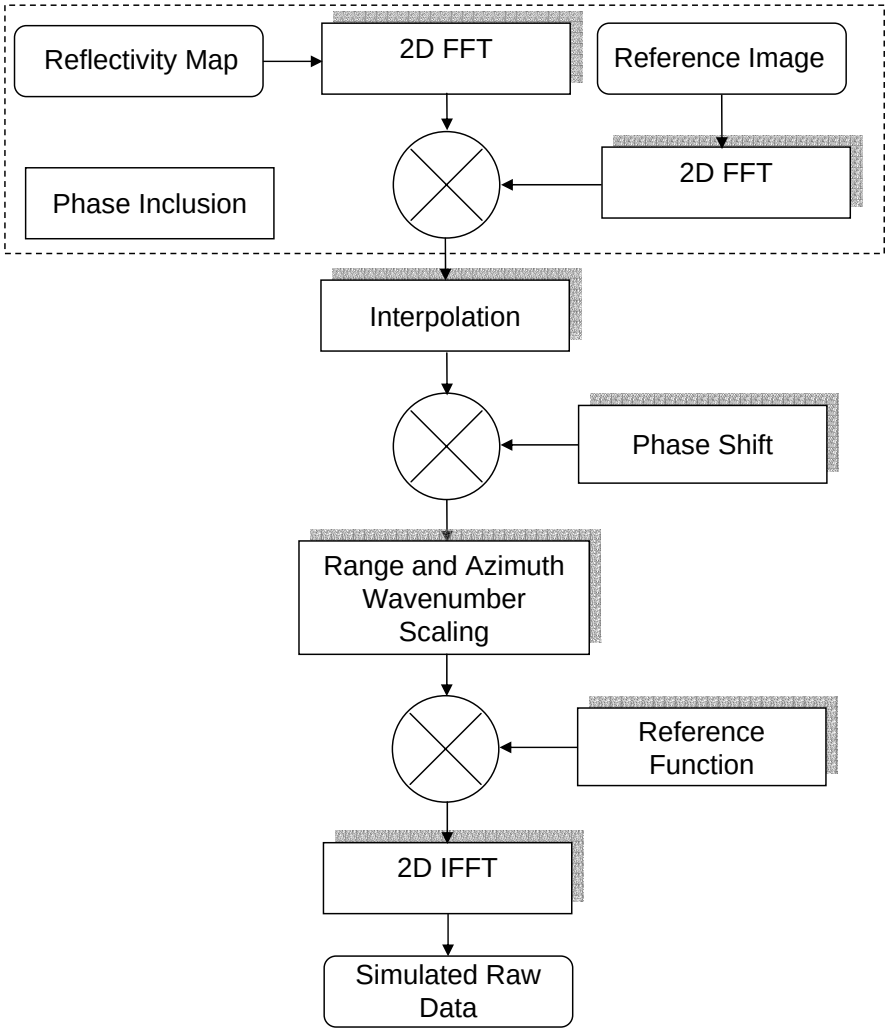

Figure 3.17: Block Diagram of a Moving Point Simulator (Modified IOKA)

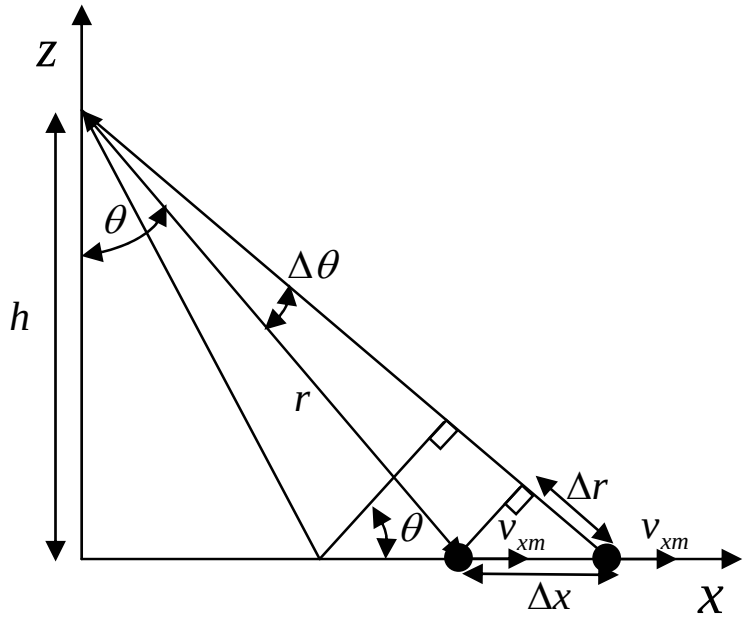

Figure 3.18: Broadside Geometry in Altitude Ground-Range Domain showing a Moving Point

a corresponding incidence angle of $\theta + \Delta\theta$), moving with the same ground range velocity, but having a different slant range velocity of

$$v_{(r+\Delta r)m} = v_{xm} \sin(\theta + \Delta\theta) \tag{3.49}$$

Thus, a change of distance Δx leads to a change of slant-range velocity, even though the ground-range velocity may be the same. Therefore, an object size in ground-range direction needs to be smaller than a certain limit for the simulator proposed in figure 3.17 to be applicable. This limit on the object size can be calculated by considering two constraints:

Constraint 1
The difference in slant-range velocities due to a displacement Δx (Δr) in ground (slant) range should be small that is expressed as

$$\mid v_r - v_{(r+\Delta r)} \mid \ll 1 \tag{3.50}$$

Using equation 3.48, equation 3.50 can be rewritten as

$$\mid v_x \sin\theta - v_x \sin(\theta + \Delta\theta) \mid \ll 1 \tag{3.51}$$

Expanding $\sin(\theta + \Delta\theta)$ and using small angle approximation, the limit on $\Delta\theta$ is

$$\mid \Delta\theta \mid \ll \frac{1}{v_x \cos\theta} \tag{3.52}$$

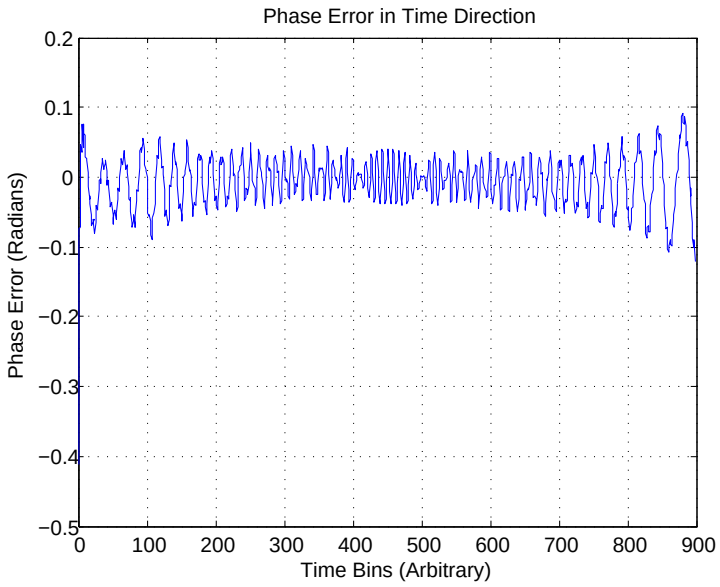

Figure 3.19: Phase Error in Time Direction

The relationship given by equation 1.6 can be used to calculate the maximum allowed object size of $2 \mid \Delta x \mid$, where

$$\mid \Delta x \mid \ll \frac{r}{v_x \cos^2 \theta} \tag{3.53}$$

Constraint 2
Equation 3.35 shows the presence of an azimuth shift that varies with the range position, even though the range velocity may be constant. Thus, another limit on the object size may be obtained by considering the difference in shift due to a different range positions to be less than the azimuth resolution, i.e.

$$\begin{aligned} \left| \frac{v_r r}{v_{sar}} - \frac{v_r (r + \Delta r)}{v_{sar}} \right| &< \delta y \\ \mid \Delta r \mid &< \frac{\delta y v_{sar}}{v_r} \end{aligned} \tag{3.54}$$

Here, it is assumed that constraint 1 is satisfied. Using the relationship between ground range and slant range, the limit is

$$\mid \Delta x \mid < \frac{v_{sar} \delta y}{v_x \sin^2 \theta} \tag{3.55}$$

that is more restrictive than the one given by equation 3.53.

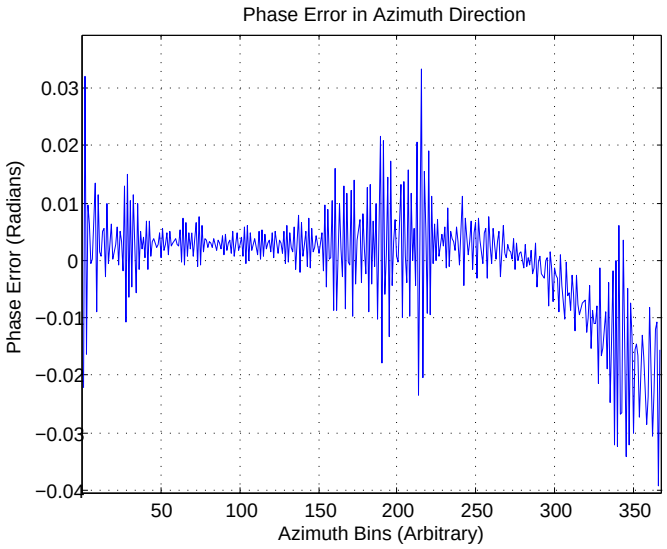

Figure 3.20: Phase Error in Azimuth Direction

Figures 3.19 and 3.20 show the time and azimuth phase errors for the RD simulated by the approach shown in figure 3.17 and a time domain simulator for a point (in order to compare phase errors). The point is at the center of the scene and its range and azimuth velocities are 1.5 ms^{-1} and 2 ms^{-1}, respectively.

The advantage offered by the proposed approach is that RD can be simulated for a moving object having a certain velocity in the range and azimuth directions, if a reference image of a static object is available (unlike time-domain simulator that always requires a reflectivity map). In this case, the input to the simulator will be this image and there will no phase inclusion stage. [41] presents a simulator resembling the one presented here, however it has three major drawbacks:

- It uses approximations to find the scaling and rotation factors (mainly $\sqrt{\mathbf{v_{rm}}^2 + (1 - \mathbf{v_{yn}})^2} \approx 1 - \mathbf{v_{yn}}$).
- It does not include the azimuth frequency shift arising due to the motion.
- No calculations regarding the object size in ground-range directions have been made.

An example for this case is demonstrated in figures 3.21-3.23. Figure 3.21 shows the input image of a static object that is used to simulate RD corresponding to range and azimuth velocities of 2.5 ms^{-1} and 2 ms^{-1}. The simulated RD is used for image formation and the result is shown in figure 3.22. A position shift, as well as defocusing in the azimuth direction can be observed, which are the effects arising due to movement. Figure 3.23 shows the image synthesized by taking into account the movement, that can be achieved by modifying the matched filter and the interpolation stage of the OKA, as described in [2].

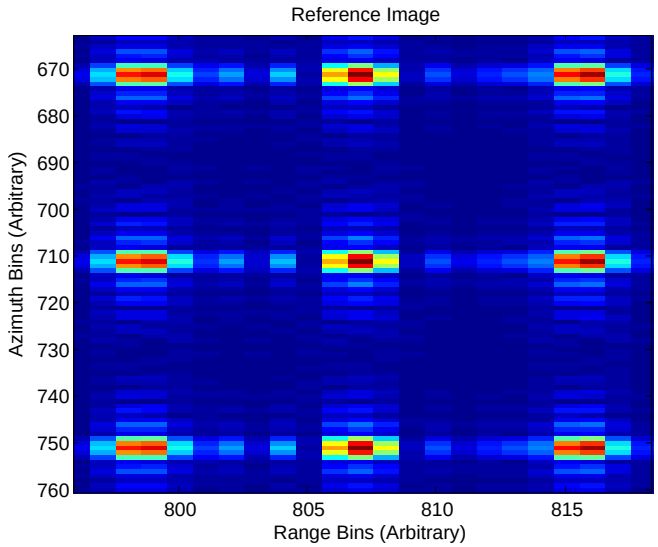

Figure 3.21: Input Image of a Static Object

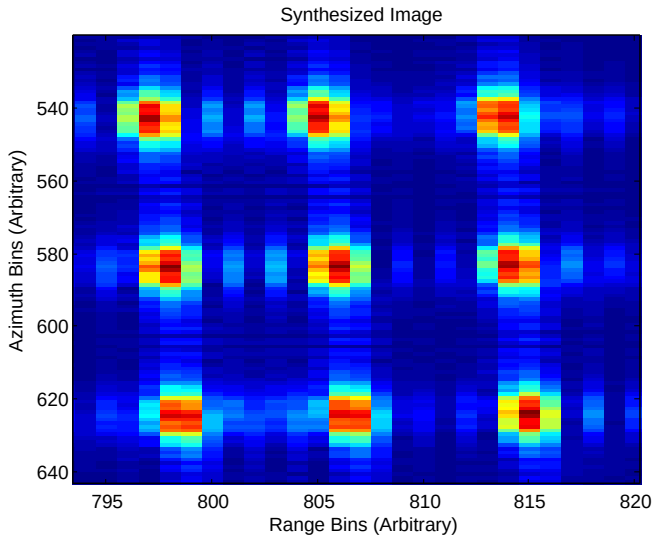

Figure 3.22: Synthesized Image showing Shift and Defocusing

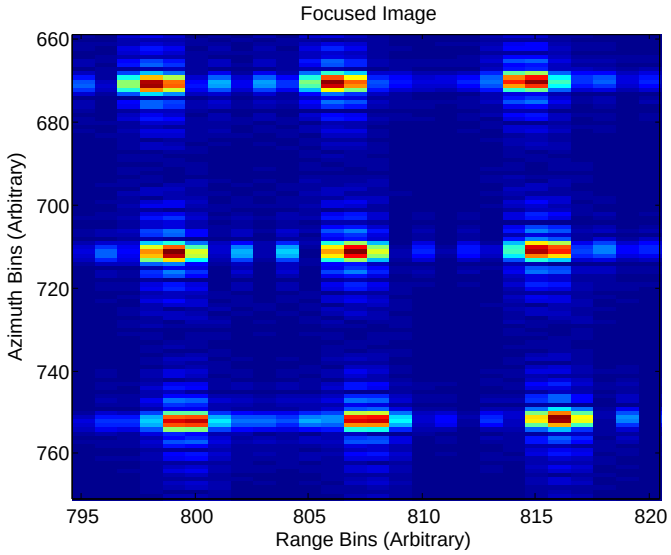

Figure 3.23: Focused Image

Comments

- In this chapter, the reflectivity map is assumed to consist of isotropic points. This may not always be so for a complex object, as its response may vary during the raw data acquisition process. Moreover, the reflectivity map is sampled uniformly.
- The quality of data simulated by IOKA depends on the quality of the interpolator employed. For the examples given here, the interpolator cubic "spline" given in MATLAB has been used, as this type of interpolator is known to perform better even with low degree polynomials, besides being simple to calculate.

3.4 Conclusions

This chapter examined raw data simulation in different domains. It was shown that the two dimensional frequency domain is the best one in terms of accuracy and computational efficiency. Two variants were proposed: The first one uses partial summation, while the second one replaces this summation by an interpolation. A relationship between the reflectivity map and the corresponding SAR image was shown, that actually leads to the conclusion that image formation algorithms can be reversed to generate raw data. Simulation examples using inverse Omega-k and inverse Chirp Scaling algorithms were presented. It was also shown that RD for a moving object can be generated in the wavenumber domain by a geometric transformation and interpolations.

Chapter 4

SAR Raw Data Simulation in case of Sensor Trajectory Deviations

4.1 Outline of the Chapter

This chapter presents SAR raw data simulation in the case where the sensor may undergo trajectory deviations, which is common in airborne SAR systems. It first presents the expressions for the raw data in case of motion errors, followed by image formation that consists of an additional step called motion compensation. Two different raw data simulation schemes are proposed that make use of certain approximations. These approximations are analyzed to estimate their respective validity domains and illustrated by simulation examples.

4.2 Basic Expressions

In the preceding chapter, it was assumed that the RD have been acquired using an ideal flight path, i.e., constant velocity and a linear trajectory. However, in reality, the flight path can be non-linear due to atmospheric disturbance. The 3D geometric configuration of a SAR operating in such a case is shown in figure 4.1. Here, a single point at ground range, azimuth and height positions of x_a, y_a and z_a, respectively is considered. The platform deviates from an ideal straight trajectory by an error of $x_e(y), y_e(y)$ and $z_e(y)$. The radar-target distance in this case as a function of along-flight position is given as:

$$d_a(y) = \sqrt{\{x_a - x_e(y)\}^2 + \{y - y_a - y_e(y)\}^2 + \{h - z_a - z_e(y)\}^2} \tag{4.1}$$

For the moment, the above expression is written as

$$d_a(y) = \sqrt{\{r_a - r_{ea}(y)\}^2 + \{y - y_a - y_e(y)\}^2} \tag{4.2}$$

where r_a is the shortest slant-range distance, and $r_{ea}(y)$ is the effective trajectory error in slant-range (for the point a), to be calculated later. The acquired RD can be described as

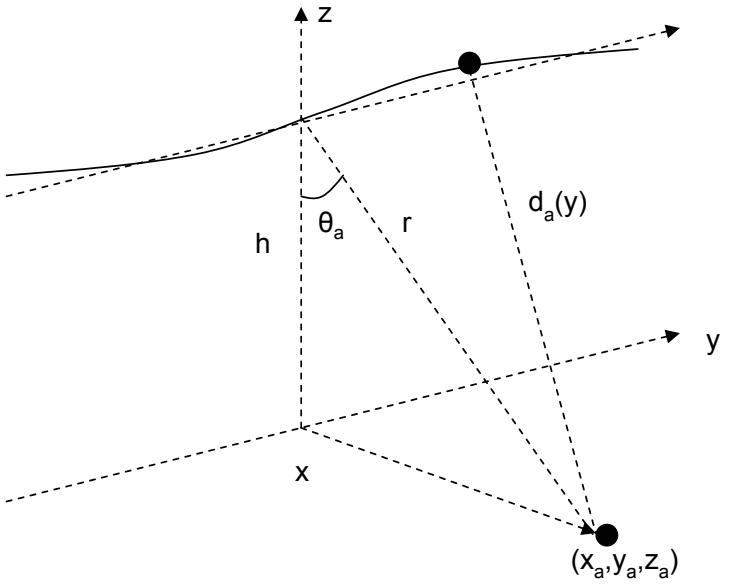

Figure 4.1: 3D Geometry showing Data Acquisition Geometry in case of Motion Errors

$$s_a(t,y) = \sigma(r_a, y_a) p\left(t - \frac{2\sqrt{\{r_a - r_{ea}(y)\}^2 + \{y - y_a - y_e(y)\}^2}}{c}\right) \tag{4.3}$$

$y_e(y)$ represents the distance error (resulting from velocity variation) in the azimuth direction. These variations are usually compensated by an on-line adjustment of the PRF or by resampling of the raw data in the azimuth direction [1]. Thus, it is neglected in the following calculations.

The 1D FT of equation 4.3 in the time direction can be written as

$$S_a(k,y) = P(\Delta k)\sigma(r_a, y_a) \exp\left(-j2k\sqrt{\{r_a - r_{ea}(y)\}^2 + (y - y_a)^2}\right) \tag{4.4}$$

or

$$S_a(k,y) = P(\Delta k)\sigma(r_a, y_a) \exp(-j2k\sqrt{r_a^2 + (y - y_a)^2})\Delta S_{ea}(k,y) \tag{4.5}$$

where

$$\Delta S_{ea}(k,y) = \exp\{j2k\Delta r_{ea}(y)\} \tag{4.6}$$

and

$$\Delta r_{ea}(y) = -\sqrt{\{r_a - r_{ea}(y)\}^2 + (y - y_a)^2} + \sqrt{r_a^2 + (y - y_a)^2} \tag{4.7}$$

is the effective along-flight position-varying error. Note that this error depends on the range and azimuth position of the imaged point in a scene.

The 2D FT of equation 4.3 gives

$$S_a(k, k_y) = P(\Delta k)\sigma(r_a, y_a) \exp\left(-jr_a\sqrt{4k^2 - k_y^2} - jy_a k_y\right) \Delta S_{ea}(k, k_y) \tag{4.8}$$

where $\Delta S_{ea}(k, k_y)$ is a spatially-varying error that is related to $\Delta S_{ea}(k, y)$ via a scale transformation [2] f_a(to be detailed in the next section).

$$f_a : \Delta S_{ea}(k, k_y) \rightarrow \Delta S_{ea}(k, y) \tag{4.9}$$

or

$$f_a : \Delta S_{ea}(k_r, k_y) \rightarrow \Delta S_{ea}(k, y) \tag{4.10}$$

4.3 Image Formation

4.3.1 Time Domain Image Formation

In case of time-domain image formation, Motion Compensation (MoCo) can be easily accommodated according to the following equation:

$$i(r_m, y_n) = \int_{-\infty}^{\infty} s_{cd}\left(t - \frac{2\sqrt{(r_m - r_{em})^2 + (y - y_a)^2}}{c}, y\right) dy \tag{4.11}$$

Thus, the only change compared to motion-error free case is a change in the along-flight summation.

4.3.2 Frequency Domain Image Formation

For frequency domain image formation such as CSA and OKA, MoCo procedures have been presented by [2], [12], [14], [42] and [44]. These procedures can be divided into two main categories: Narrowbeamwidth MoCo and Widebeamwidth MoCo described as follows:

4.3.2.1 Narrowbeamwidth Motion Compensation

By examining equations 4.5 and 4.8, it can be inferred that MoCo consists of canceling the terms $\Delta S_{ea}(k, y)$ or $\Delta S_{ea}(k, k_y)$, depending on whether it is carried out in 1D or 2D wavenumber domain, respectively. For this purpose, one option is to make narrowbeamwidth (Nbw) approximation, which considers the motion errors as depending only on the range position of a point scatterer or the same for the whole azimuth beam as the beam center. Effects of this approximation are studied in [43]. Using this approximation,

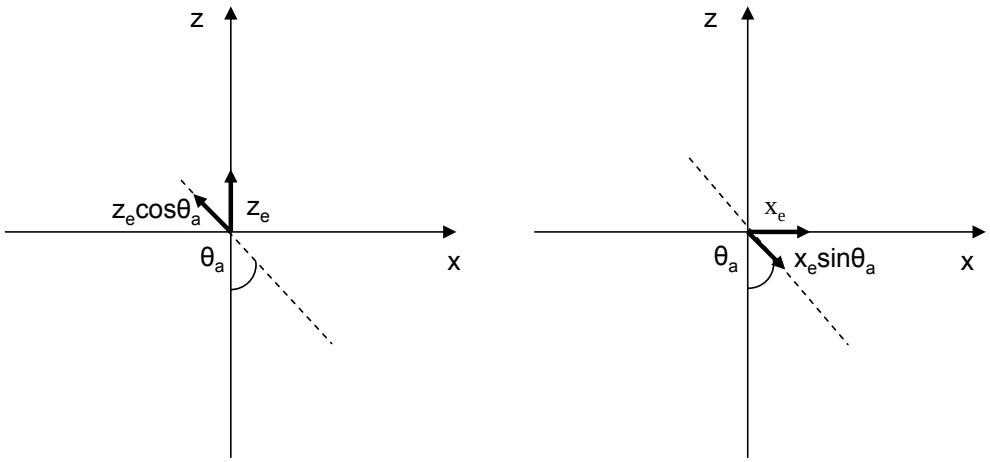

Figure 4.2: Narrowbeamwidth Motion Errors

the motion error in the slant-range $\Delta r_{ea}(k, y)$ can be written as

$$\Delta r_{ea}(y) \approx r_{ea}(y) \tag{4.12}$$

where $r_{ea}(y)$ is given as [1]

$$r_{ea}(y) = x_e(y) \sin\theta_a + z_e(y) \cos\theta_a \tag{4.13}$$

By considering figure 4.2, where $\theta_a = \arccos\left(\frac{h-z_a}{r_a}\right)$, (assuming a flat earth), equation 4.6 can be rewritten as

$$\Delta S_{ea}(k, y) = \exp\{j2(k_c + \Delta k) r_{ea}(y)\} \tag{4.14}$$

It is clear that motion errors cause a phase error due to the term $\exp\{j2k_c\Delta r_{ea}(y)\}$ as well as a displacement in the time direction due to the shift given by $\exp\{j2\Delta k\Delta r_{ea}(y)\}$. In the case of a single scatterer, these terms can be canceled easily by multiplying the RD and the complex conjugate of equation 4.14.

For a real scene consisting of $n_r n_y$ scatterers, this may not be possible because the range position required for calculating the incidence angle θ is not known at the RD stage (as the chirps are spread in the time and azimuth directions). The expression for RD in transmitted wavenumber domain for a scene in this case is given as

$$S(k, y) = P(\Delta k) \sum_{m,n} \sigma(r_m, y_n) \exp\left(-j2k\sqrt{r_m^2 + (y - y_n)^2}\right) \Delta S_{em}(k, y) \tag{4.15}$$

where

$$\Delta S_{em}(k, y) = \exp\{j2kr_{em}(y)\} \tag{4.16}$$

and

$$r_{em}(y) = x_e(y)\sin\theta_m + z_e(y)\cos\theta_m \tag{4.17}$$

In order to circumvent this problem, MoCo is divided in two stages: 1^{st} Order MoCo and 2^{nd} Order MoCo. The former, shown in equation 4.18, corrects the motion errors (both phase and position correction) corresponding to a reference range r_{ref}. Subsequently, range migration compensation and range compression is carried out using CSA. It is assumed that the range-dependent component of motion errors does not effect the range migration process [1].

$$\Delta S^*_{eref}(k, y) = \exp\{-j2kr_{eref}(y)\} \tag{4.18}$$

Before the remaining step of azimuth compression, the azimuth chirps are roughly localized at their respective range positions, and the 2^{nd} Order MoCo consisting of only the phase correction term can be applied for each range position.

$$\Delta S^*_{em}(r_m, y) = \exp[-j2k_c\{r_{em}(y) - r_{eref}(y)\}] \tag{4.19}$$

The resulting data can then be compressed in the azimuth direction. The block diagram for this process is shown in figure 4.3. This procedure, though quite suitable for use with CSA, cannot be applied to OKA, as in this case, the data is range and azimuth compressed in a single step. [14] has proposed a modified OKA to integrate the two-step MoCo procedure.

4.3.2.2 Widebeamwidth Motion Compensation

[2], [14], [42] propose widebeamwidth (Wbm) MoCo, operated in the 2D wavenumber domain that are quite similar to one another. In the following, the method given in [2] will be described as it presents the analytical form for the motion error correction terms. The expression for motion error affected RD in 2D frequency domain is given as

$$S(k, k_y) = P(\Delta k)\sum_{m,n}\sigma(r_m, y_n)\exp\left(-jr_m\sqrt{4k^2 - k_y^2} - jy_nk_y\right)\Delta S_{emn}(k, k_y) \tag{4.20}$$

The motion error for each point at position (m, n) after processing by OKA (or CSA) is

$$\Delta S_{emn}(k_r, k_y) = \exp\{j2k\Delta r_{emn}(y)\} \tag{4.21}$$

where

$$\Delta r_{emn}(y) = -\sqrt{\{r_m - r_{em}(y)\}^2 + (y - y_n)^2} + \sqrt{r_m^2 + (y - y_n)^2} \tag{4.22}$$

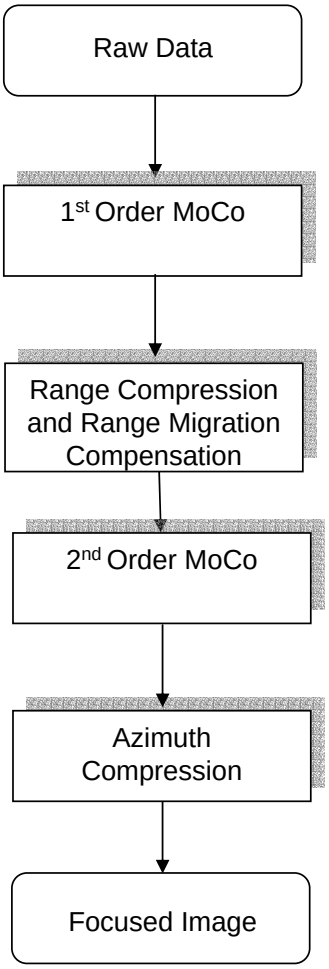

Figure 4.3: Narrowbeamwidth Motion Compensation Procedure

The following transformations map the motion errors from (k, y) domain to (k_r, k_y) domain:

Transformation 1

$$2k = \sqrt{k_r^2 + k_y^2} \tag{4.23}$$

Transformation 2

$$y = y_n - \frac{k_y}{k_r} r_m \tag{4.24}$$

Transformation 1 is quite straightforward and can be derived by using equation 2.14. Transformation 2 can be calculated by considering the fact that the radar wavelength λ_c can be divided into two components: The wavelength in the range direction λ_{cr} and the wavelength in the azimuth direction λ_{cy}. These two wavelengths can be related to the radar wavelength and the aspect angle as

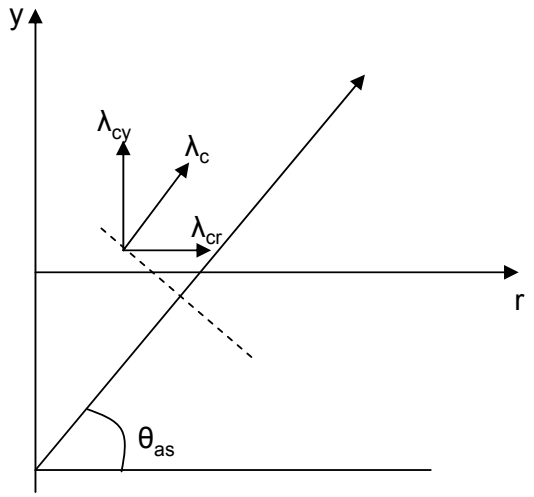

Figure 4.4: Tranmitted Wavelength and its Relationship with Azimuth and Range Wavelengths

$$\lambda_{cr}(y) = \frac{\lambda_c}{\cos\theta_{as}(y)} \tag{4.25}$$

$$\lambda_{cy}(y) = \frac{\lambda_c}{\sin\theta_{as}(y)} \tag{4.26}$$

$$\tan\theta_{as}(y) = \frac{y - y_n}{r_m} \tag{4.27}$$

The relation between the wavenumber and the wavelength gives

$$k_r(y) = 2k\cos\theta_{as}(y) \tag{4.28}$$

$$k_y(y) = 2k\sin\theta_{as}(y) \tag{4.29}$$

leading to

$$\frac{k_y(y)}{k_r(y)} = \tan\theta_{as}(y) = \frac{y - y_n}{r_m} \tag{4.30}$$

that results in transformation 2. If the fluctuations of this motion error phase function are much smaller than those of the SAR signal without motion errors, it can be modeled as a filter in the spatial frequency domain for each point scatterer [2]. This may not be so in realistic cases, but these fluctuations can be reduced by carrying out 1^{st} order MoCo as in Nbw approximation for a reference position, processing the RD by OKA or CSA, followed by dividing the resulting images in subpatches and applying the following spatially-varying error compensation to the center of each subpatch in 2D frequency domain using the two

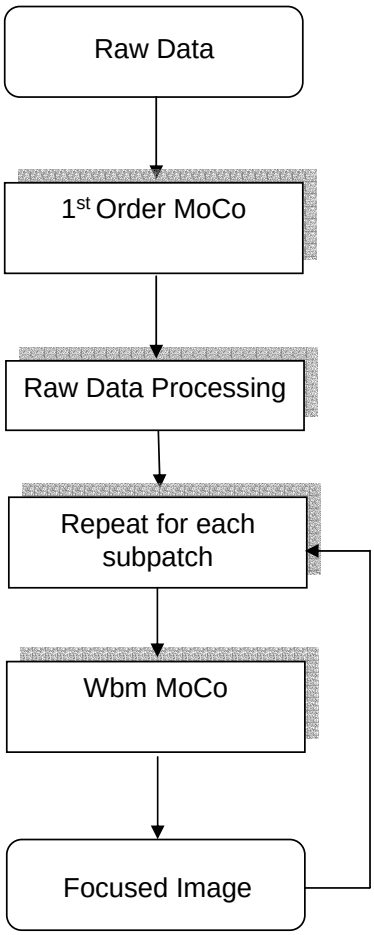

Figure 4.5: Widebeamwidth Motion Compensation Procedure

preceding transformations.

$$\Delta S^*_{emn}(k_r, k_y) = \exp[-j2k\{\Delta r_{emn}(y) - \Delta r_{eref}(y)\}] \tag{4.31}$$

4.3.2.3 Example of Motion Compensation

For demonstrating the MoCo procedure, RD for four points imaged with a sensor having ground range and altitude trajectory errors shown in figure 4.6 are simulated. The sensor parameters are the same as given in table 3.1.The corresponding RD is processed without any MoCo and the result is shown in figure 4.7. It is clear that all the points are defocused and spread in the azimuth direction. Figure 4.8 shows the data after processing by CSA and 1^{st} order MoCo corresponding to the range at the scene center as the reference range. The point at the center is focused but the other points are still partially defocused. Figure 4.9 shows the focused image after 1^{st} and 2^{nd} order MoCo where all the points are focused.

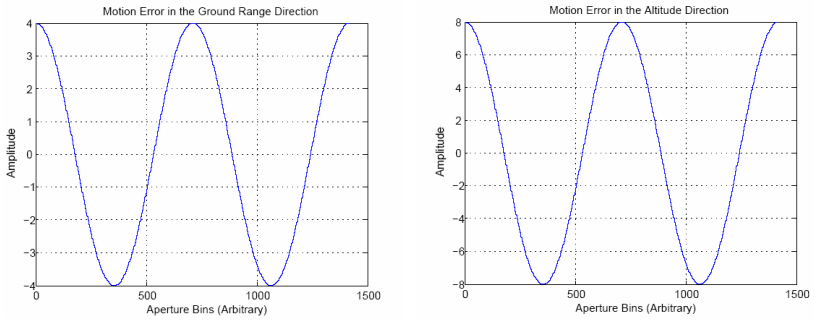

Figure 4.6: Simulated Motion Errors in Ground-Range and Altitude Directions

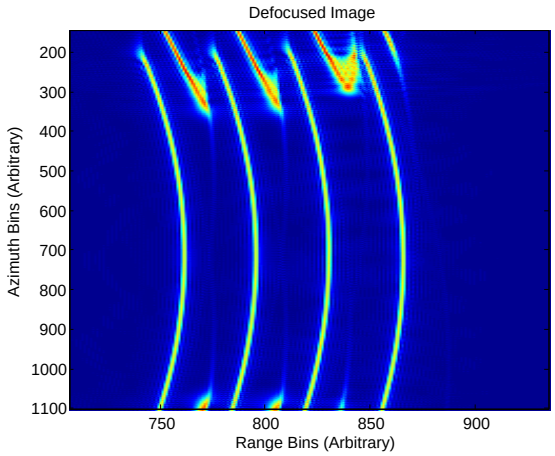

Figure 4.7: Defocused Image in the absence of MoCo

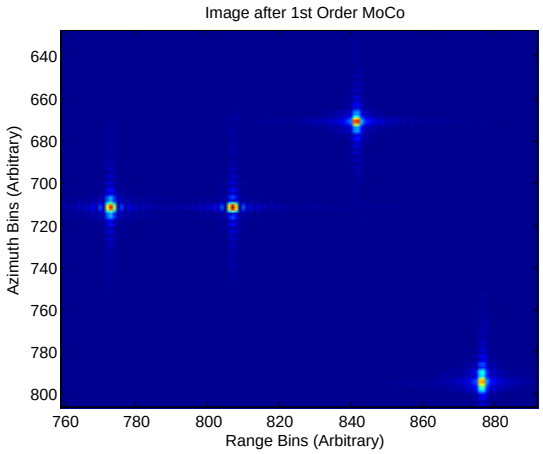

Figure 4.8: Raw Data Processing with 1^{st} order MoCo

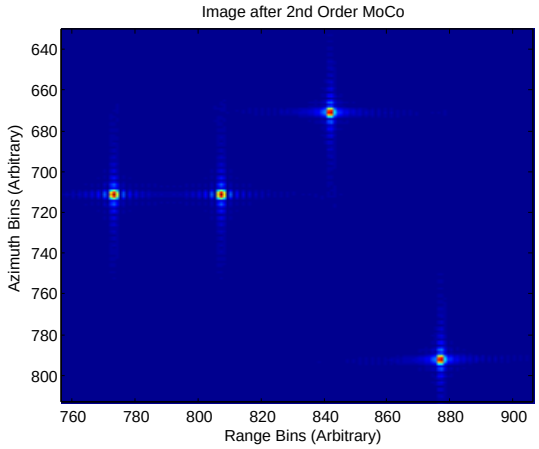

Figure 4.9: Raw Data Processing with 1^{st} and 2^{nd} order MoCo

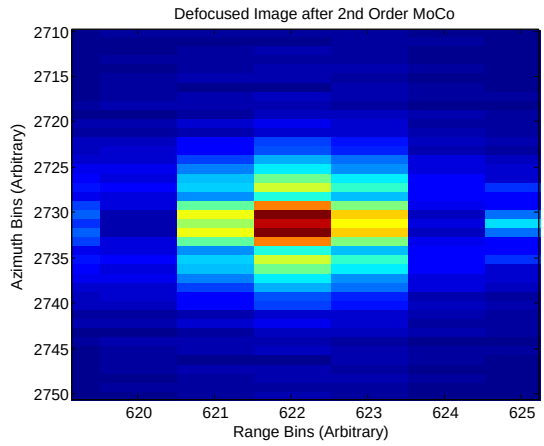

Figure 4.10: Raw Data Processing with 1^{st} and 2^{nd} order MoCo (16° Aperture Angle)

In the second example, a single point at the scene center with an azimuth aperture angle of 16° is simulated to show the utility of Wbw MoCo. Figure 4.10 shows that in case of Nbw 1^{st} and 2^{nd} order MoCo, the image is not completely focused, whereas figure 4.11 shows the image after Nbw 1^{st} order and Wbw MoCo, which is completely focused.

4.4 Motion Error Effects

Motion effects in case of a sinusoidal error have been described in [12] with the help of Nbw approximation and Bessel functions. It is stated that such an error results in spectral replication. Details concerning the loss of image quality are given in [45]. However, these effects can be studied in a more meaningful physical manner, without using a Nbw approximation, by considering a single point as in the preceding section at position a. RD

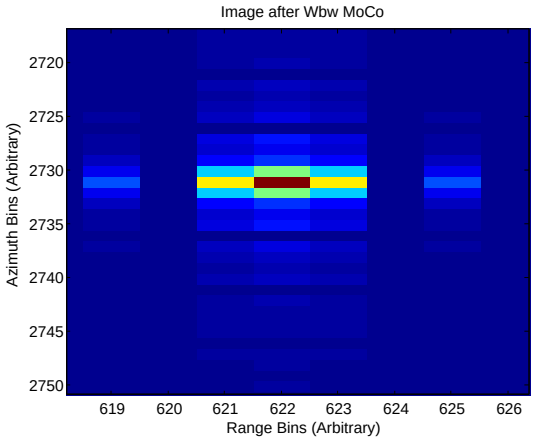

Figure 4.11: Raw Data Processing with Wbw MoCo (16° Aperture Angle)

in slant-range direction $r_{ea}(y)$ can be approximated by dividing the trajectory (y) in a number of linear segments N and to be made up of RD acquired for all these positions, as follows:

$$\begin{aligned} y &= [y_1 .... y_N] \\ s_{an}(y) &= r_{ea}(y_n) + y \tan \Psi_n \end{aligned} \tag{4.32}$$

where

$$\Psi_n = \arctan \left\{ \frac{r_{ea}(y_{n+1}) - r_{ea}(y_n)}{y_{n+1} - y_n} \right\} \tag{4.33}$$

Making use of the transformation shown in figure 3.16, sensor imaging for each linear segment can be seen as equivalent to a squint-mode configuration with an angle Ψ_n. Thus, each linear segment results in an image with a resolution reduced by a factor of N and at a shifted position of

$$r_{an} = r_a \cos \Psi_n + y_a \sin \Psi_n \tag{4.34}$$

$$y_{an} = -r_a \sin \Psi_n + y_a \cos \Psi_n \tag{4.35}$$

In case of a large value for N, the synthesized image consists of multiple copies of low resolution images, that are shifted from the actual position (r_a, y_a). This is demonstrated in figure 4.12, where the trajectory error was approximate by linear segments. RD were simulated using these segments, as well as the actual error and the synthesized images for both these cases are shown. Both of the defocused images resemble each other, meaning that motion error effects can be described physically by linear segmentation and a change of geometry for each segment.

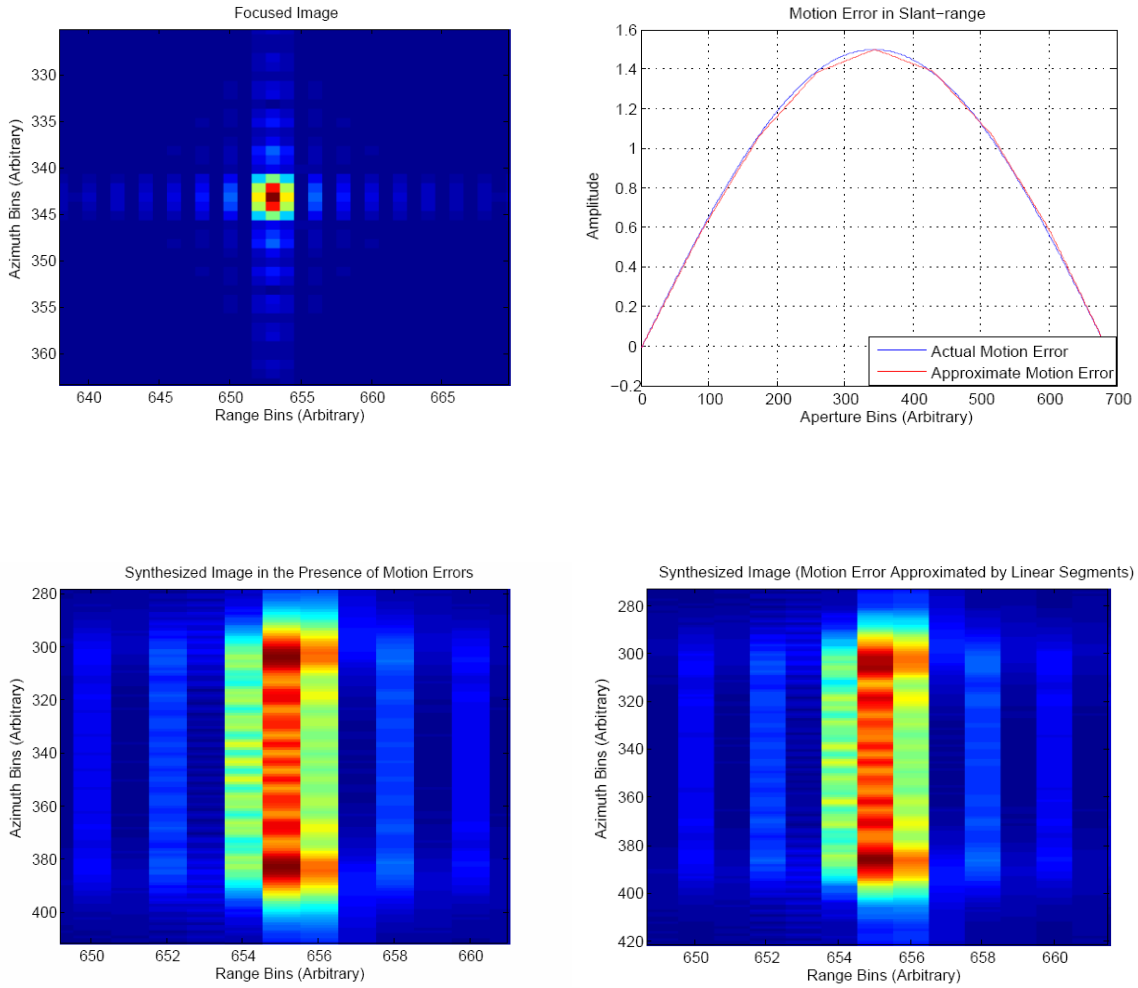

Figure 4.12: A Focused Image, Motion Error in the Slant Range and its Linear Approximations, and Processed Data corresponding to Both Cases

4.5 SAR Raw Data Simulation

SAR RD simulation in the case of sensor motion errors is similar to the one with no motion errors, if the time domain simulation is used. It can be inferred from equation 4.3 that the RD corresponding to an entire scene are the sum of the RD for each point in the scene. Thus, the total number of multiplications required for a scene of dimension $n_r n_y$ is $n_r n_y n_t n_a$ as in chapter 3 that can be too large in case of a realistic case. Hence, efficient RD simulation in the frequency domain is explored.

As discussed in section 4.3, MoCo procedure is integrated with the image formation process to generate focused images. It has already been stated in chapter 3 that RD simulation can be achieved in 2D frequency domain by inverse image formation algorithms, alongwith the phase inclusion process. If the MoCo procedure can also be reversed, it may be integrated with the RD simulation schemes proposed in chapter 3 to generate efficiently the RD. However, it is very easy to see that the Wbw MoCo described in subsection 4.3.2.2 is dependent on the position of each point in the image. Therefore, in order to use it in inverse form, the reflectivity map after multiplication by the reference function has to be divided in subpatches, and each subpatch is subsequently multiplied by motion errors corresponding to the center of the scene in 2D frequency domain. This approach is not appropriate for RD simulation, as each subpatch contains not only the contributions from points in the neighboring subpatches, but the process of making a subpatch causes the loss of a part of the spectrum and leads to phase discontinuities.

The Nbw Moco may seem appropriate for RD simulation using ICSA, as it uses range-varying exponential multiplications before azimuth compression to compensate the whole image. However, this multiplication causes a wavenumber shift in the time direction, that varies with the range positions, described as a residual range-varying phase for the sidelobes in [88]. This shift, for a point at position m, is given by

$$\begin{aligned} \Delta k_m(y) &= k_c \frac{d\{r_{er}(y) - r_{em}(y)\}}{dr} \\ &\approx k_c x_e(y)(\sin\theta_r - \sin\theta_m) + k_c z_e(y)(\cos\theta_r - \cos\theta_m) \\ &\approx k_c x_e(y)(\theta_r - \theta_m)\cos\theta_m - k_c z_e(y)(\theta_r - \theta_m)\sin\theta_m \end{aligned} \tag{4.36}$$

where r in the subscript r_{er} varies from 1 to n_r for each m, and $\sin\theta_r$ and $\cos\theta_r$ have been linearized in the vicinity of θ_m. Thus, this wavenumber shift is actually varying with the range position of the point scatterer. In order to use inverse MoCo, this shift should be first incorporated for each range position separately. Therefore, simulating the RD using directly these algorithms is not feasible. An example for the purpose of illustration is shown in the figures 4.13 and 4.14.

In literature, [31], [33] present RD simulators for stripmap and spotlight modes, respectively that use partial summation operations. The latter uses the approach presented in figure 3.2, using equation 3.8. In the following, other options based on [31] will be examined and improvements will be proposed.

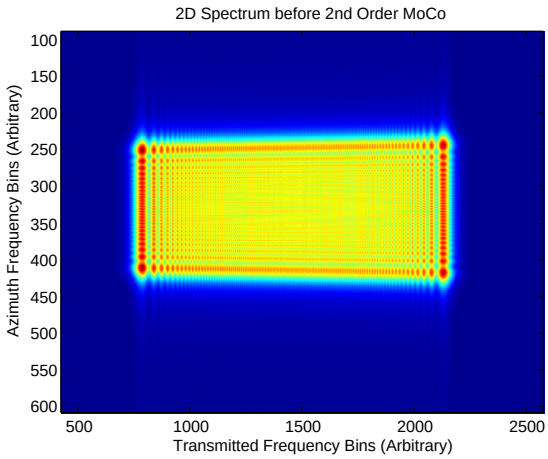

Figure 4.13: 2D Spectrum before 2^{nd} Order MoCo

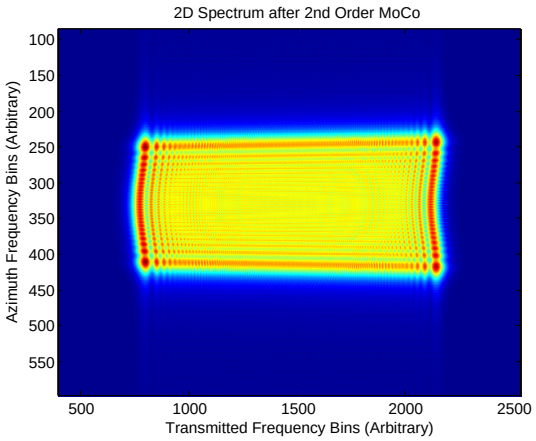

Figure 4.14: 2D Spectrum after 2^{nd} Order MoCo

Considering equation 4.15, it can be seen that RD in 1D range wavenumber domain is actually a summation of RD for each scatterer. Thus RD generation using this property does not hold any advantage compared to the time-domain simulation. However, some efficiency may be achieved by expanding the square root in the exponential term using Taylor series:

$$\sqrt{r_m^2 + (y - y_n)^2} = r_m + \frac{(y - y_n)^2}{2r_m} - \frac{(y - y_n)^4}{8r_m^3} + ... \tag{4.37}$$

Using this expression, equation 4.15 becomes

$$S(k, y) = P(\Delta k) \sum_{m,n} \sigma(r_m, y_n) \exp\left[-j2k\left(r_m + \frac{(y - y_n)^2}{2r_m} - \frac{(y - y_n)^4}{8r_m^3}\right)\right] \Delta S_{em}(k, y) \tag{4.38}$$

that can be rewritten in the form of a convolution as

$$\begin{aligned} S(k, y) &= P(\Delta k) \sum_{m,n} \sigma(r_m, y_n) \exp(-j2kr_m) \left\{\exp\left(-j2k\frac{y^2}{2r_m} + j2k\frac{y^4}{8r_m^3}\right) \otimes \delta(y - y_n)\right\} \\ &\quad \Delta S_{em}(k, y) \end{aligned} \tag{4.39}$$

Using the 1D FT of the ideal target function $\Gamma(r_m, k_y)$ given in equation 3.7, the summation in the azimuth direction can be carried out using FFTs and multiplications as shown below:

$$\begin{aligned} S(k, y) &= P(\Delta k) \sum_{m} \exp(-j2kr_m) F_y^{-1}\left[F_y\left\{\exp\left(-jk\frac{y^2}{r_m} + jk\frac{y^4}{4r_m^3}\right)\right\} \Gamma(r_m, k_y)\right] \\ &\quad \Delta S_{em}(k, y) \end{aligned} \tag{4.40}$$

where F_y and F_y^{-1} represent the FT and IFT in the azimuth direction, respectively. Thus, RD can be generated for each range position using FFTs and IFFTs, and adding the result. Its block diagram is shown in figure 4.15 and its computational complexity can be calculated as follows:

- 1D FFT of the exponential term $\exp\left(-jk\frac{y^2}{r_m} + jk\frac{y^4}{4r_m^3}\right)$, the reflectivity map and their multiplication followed by IFFT resulting in $2n_r n_y log_2 n_y + n_y log_2 n_y + n_r n_y$ computations.
- Multiplication of the result of the preceding step by $P(\Delta k) \exp(-j2kr_m) \Delta S_{em}(k, y)$ taking $n_r n_y$ computations.
- Summation over all the range position taking a total of $n_r(2n_r n_y log_2 n_y + n_y log_2 n_y + 2n_r n_y)$ multiplications.

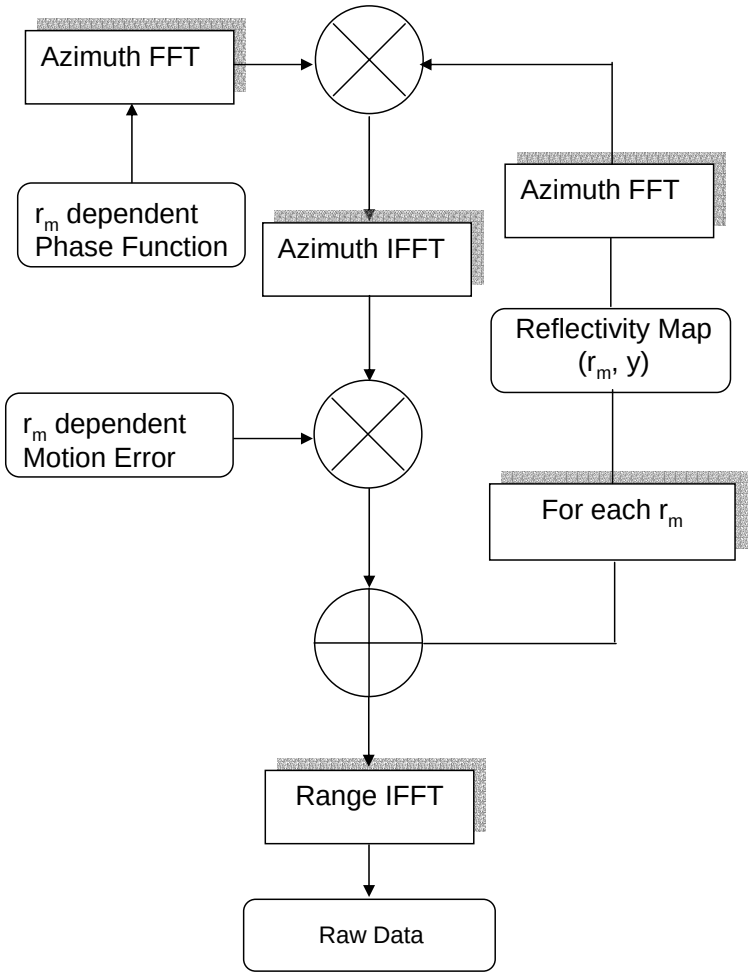

Figure 4.15: Block Diagram for Nbw Simulator

- 1D IFFT of the result taking $n_r n_y log_2 n_y$ operations.

The total number of multiplications needed can be approximated to be $2n_r^2 n_y(1 + log_2 n_y)$ that is slightly more than that in the narrowbeamwidth and arbitrary deviation method of [33]. However, this simulation method avoids calculating an expression of azimuth FT by POSP, which may be less accurate as compared to the range direction, due to a relatively low TBP.

If it is required to increase efficiency at the expense of POSP related approximations, the series expansion in equation 4.37 can be limited to the first-order term (the limit on the aperture angle is given by equation A.29) and the analytical expression for the FT of the exponential term in the azimuth direction is calculated as

$$F_y\left\{\exp\left(-jk\frac{y^2}{r_m}\right)\right\} = \exp\left(-j\frac{k_y^2 r_m}{4k}\right) \tag{4.41}$$

Using the above term in equation 4.40 reduces $n_r^2 n_y log_2 n_y$ computations.

$$S(k,y) = P(\Delta k)\sum_m \exp(-j2kr_m)F_y^{-1}\left\{\exp\left(-j\frac{k_y^2 r_m}{4k}\right)\Gamma(r_m,k_y)\right\}\Delta S_{em}(k,y) \tag{4.42}$$

It is necessary to analyze the preceding method to find its validity limits in terms of the allowed motion errors, given the parameters of the sensor and the scene following the reasoning given in [32] and [33]. For this purpose, the expression for the motion error given by equation 4.22 will be approximated [89], assuming that the motions error in the line of sight direction to be a constant, i.e., $r_{em}(y) = r_{em}$ as only the maximum allowed error is to be calculated. This simplifies the analysis as well.

$$\begin{aligned}
\Delta r_{emn}(y) &\approx r_{em} - \frac{(y_n - y)^2}{2(r_m - r_{em})} + \frac{(y_n - y)^2}{2r_m} \\
&= r_{em} - \frac{(y_n - y)^2 r_{em}}{2(r_m - r_{em})r_m} \\
&\approx r_{em} - \frac{(y_n - y)^2 r_{em}}{2r_m^2}
\end{aligned} \tag{4.43}$$

Ignoring the second part of motion error and using the first part (actually Nbw errors) in equation 4.16, the following criterion of validity is obtained for the Nbw approximation to be valid.

$$\begin{aligned}
\left|\frac{2k(y_n - y)^2 r_{em}}{2r_m^2}\right| &\ll 1 \\
\mid r_{emmax} \mid &\ll \frac{r_m^2}{(k_c + \Delta k_{max})(\Delta Y/2)^2} \\
&\ll \frac{4c}{\pi(2f_c + B_t)\theta_y^2}
\end{aligned} \tag{4.44}$$

The Nbw motion errors can be generalized by a substitution $r_{em} = d_e \sin(\theta_m + \theta_{xz})$, where $d_e(y) = \sqrt{x_e^2(y) + z_e^2(y)}$ and $\theta_{xz}(y) = \arctan\left(\frac{z_e(y)}{x_e(y)}\right)$. Thus, equation 4.44 becomes

$$\mid d_{emax} \mid \ll \frac{4c}{\pi(2f_c + B_t)\theta_y^2} \tag{4.45}$$

A second way to simulate RD is by considering wide beamwidth (Wbw) but assuming narrow bandwidth (Nbaw). For this purpose, equation 4.20 is examined, after image formation, and the Wbw errors are divided into a range position-invariant Nbw error part, and a range position varying Wbw part.

$$I(k_r, k_y) = |P(\Delta k)|^2 \sum_{m,n} \sigma(r_m, y_n) \exp(-jk_r r_m - jk_y y_n) \exp[-j2k\{\Delta r_{emn}(y) - \Delta r_{eref}(y)\}] \tag{4.46}$$

with the two transformations given by equations 4.23 and 4.24 linking the errors in (k, y) to (k_r, k_y) domain. Assuming Nbaw, i.e., $k_r \approx 2k_c$, the preceding equation can be written as

$$I(k_r, k_y) = |P(\Delta k)|^2 \sum_{m,n} \sigma(r_m, y_n) \exp(-jk_r r_m - jk_y y_n) \exp[-j2k_c\{\Delta r_{emn}(y) - \Delta r_{eref}(y)\}] \tag{4.47}$$

where

$$y \approx y_n - \frac{k_y}{2k_c} r_m \tag{4.48}$$

As a result of this approximation, an azimuth FT of the modified reflectivity map at an azimuth position y_n can be written as

$$\begin{aligned} \Gamma_n(r, k_y) \quad = \quad & \exp\left[-j2k_c\left\{\Delta r_{ern}\left(y_n - \frac{k_y}{2k_c} r\right) - \Delta r_{eref}\left(y_n - \frac{k_y}{2k_c} r\right)\right\}\right] \\ & \sigma(r, y_n) \exp(-j2k_c r - jk_y y_n) \end{aligned} \tag{4.49}$$

where

$$\Delta r_{ern}(.) = \sum_m \Delta r_{emn} \delta(r - r_m) \tag{4.50}$$

that results in

$$I(k_r, k_y) = |P(\Delta k)|^2 \sum_n F_r(\Gamma_n(r, k_y)) \tag{4.51}$$

Thus a modified reflectivity map where motion errors are embedded can be generated

according to equation 4.49 and a summing operation in the azimuth direction. This reflectivity map can then be converted into 2D frequency domain, and multiplied with the 2D FT of a reference image for the phase inclusion process. The result can then be used for RD simulation using ICSA/IOKA and the final result is the multiplied by the Nbw motion error for a reference position, i.e., $\exp\{-j2kr_{eref}(y)\}$. This process is shown in figure 4.16 and its computational complexity can be calculated by considering its main step:

- Generation of the modified reflectivity map by $n_r n_y$ multiplications for each azimuth position and taking 1D FFT of the final result requiring $n_r n_y^2 + n_r n_y log_2 n_r$ computations.
- 2D FFT of a reference image and multiplication with the above reflectivity map taking $n_r n_y log_2 n_r n_y + n_r n_y$ computations.
- Using the result for IOKA that takes $n_r n_y(\log_2(n_r n_y) + 2(2M_{ker} - 1) + 1)$ computations.
- Multiplication by the reference Nbw error taking $n_r n_y$ multiplications.

The total number of multiplications is approximated as $n_r n_y^2$, that can be less than that in [33] for Nbw approximation and moderate deviations and the preceding simulation approach as well for $n_y < n_r$. In order to find a validity domain for this simulation method, an analysis is made, making use of equation 4.45. Its second part, i.e., position-varying error is neglected for all the frequencies other than the central frequency, whereas it is the same for Nbw error, except for the reference range. Thus there are two constraints:

$$\begin{aligned} \left|\frac{\Delta k(y_n - y)^2 r_{em}}{r_m^2}\right| &\ll 1 \\ \mid r_{emmax} \mid &\ll \frac{r_m^2}{(\Delta k_{max})(\Delta Y/2)^2} \\ \mid d_{emax} \mid &\ll \frac{4c}{\pi B_t \theta_y^2} \end{aligned} \tag{4.52}$$

and

$$\begin{aligned} \mid 2\Delta k(r_{em} - r_{eref}) \mid &\ll 1 \\ \mid x_e \sin\theta_m + z_e \cos\theta_m - x_e \sin\theta_{ref} - z_e \cos\theta_{ref} \mid &\ll \frac{1}{2\Delta k} \\ \mid d_{em}\{\sin(\theta_m + \theta_{xz}) - \sin(\theta_{ref} + \theta_{xz})\} \mid &\ll \frac{1}{2\Delta k} \\ d_{em}\{\sin(\theta_{ref} + \theta_{xz}) - \sin(\theta_{ref} + \theta_{xz}) + \cos(\theta_{ref} + \theta_{xz})(\theta_m - \theta_{ref})\} \mid &\ll \frac{1}{2\Delta k} \\ \mid d_{em}\cos(\theta_{ref} + \theta_{xz})(\theta_m - \theta_{ref}) \mid &\ll \frac{1}{2\Delta k} \end{aligned} \tag{4.53}$$

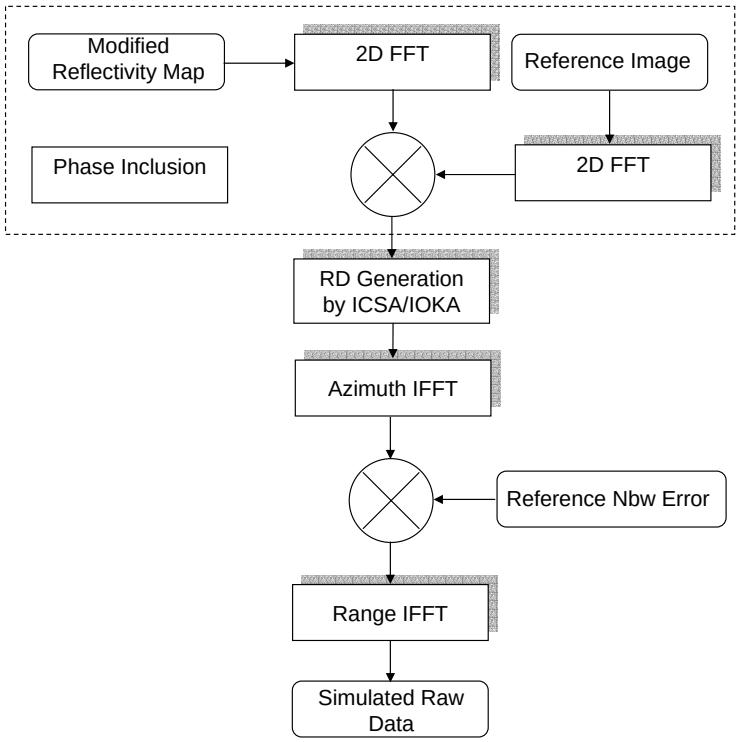

Figure 4.16: Block Diagram for Nba Simulator

$\sin(\theta_m + \theta_{xz})$ has been linearized in the above equation around $\theta_{ref} = \arccos(h/r_{ref})$. The following constraint is observed:

$$\mid d_{emax} \mid \ll \frac{c}{2\pi B_t \mid \theta_m - \theta_{ref} \mid} \tag{4.54}$$

This constraint is more severe than the preceding one and that given for the Nbw approach, however, in case of a high aperture angle, it may be less restrictive, e.g., for an azimuth aperture angle of 4° and 10°, the limits are 29 m and 5 m, respectively for Nbw case, whereas for Nba case, the maximum allowed deviation is 8.5 m for a point at the end of the scene.

4.5.1 Examples

In order to demonstrate the accuracy of the proposed techniques, phase of the simulated RD is compared to the phase of the data from a time-domain simulator. The simulation parameters used are the same as in table 3.1. A point is placed at a slant-range distance of 45 m from the scene center and RD were simulated with a trajectory error in the form of a cosine, having a maximum amplitude of 0.8 m and covering two cycles over the aperture, in the directions of altitude and ground range. The phase difference for both approaches through one range and azimuth position in the RD is shown in figures 4.17 and 4.18, and indicates satisfactory results. In the case of Nbw approach, this error in the azimuth

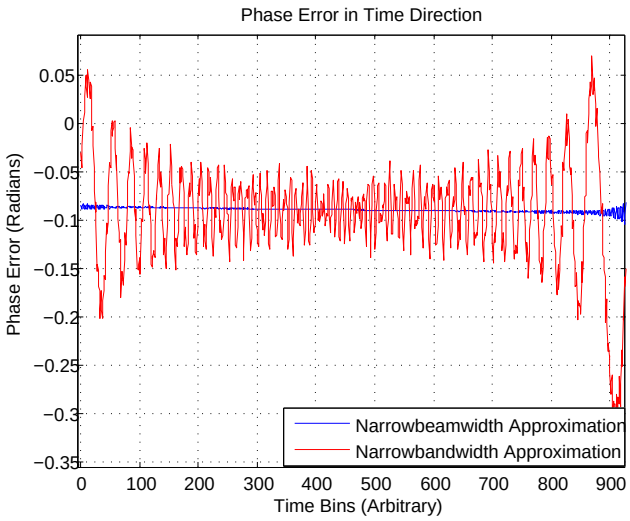

Figure 4.17: Phase Error in Time Direction for a Point at 45 m

direction is slightly less than that generated by Nba (using ICSA) approach as the latter is limited by the distance of a point from the reference range. To reinforce this point, the same process is repeated for a point at the center that is also the reference range and at a slant range distance of 450 m from the center. It is clear that the phase error in the azimuth direction increases for the Nba, as the point moves away from the scene center.

Another point that should be noted is that the use of equation 4.42 induces a limit on the value of the aperture angle. As an example, a point at a distance of 45 m from the scene center is used to simulate RD with an aperture angle of 10° and the corresponding phase errors are plotted in figures 4.23 and 4.24. The phase error using Nbw approach alongwith equation 4.42 is much more than that using Nba approach, especially at the extremes of aperture.

4.6 Conclusions

This chapter has explained image formation and RD simulation in the presence of motion errors. Two different approaches based on narrow-bandwidth and narrow-beamwidth approximations were proposed for this purpose and analyzed to find validity limits in terms of system parameters and motion errors.

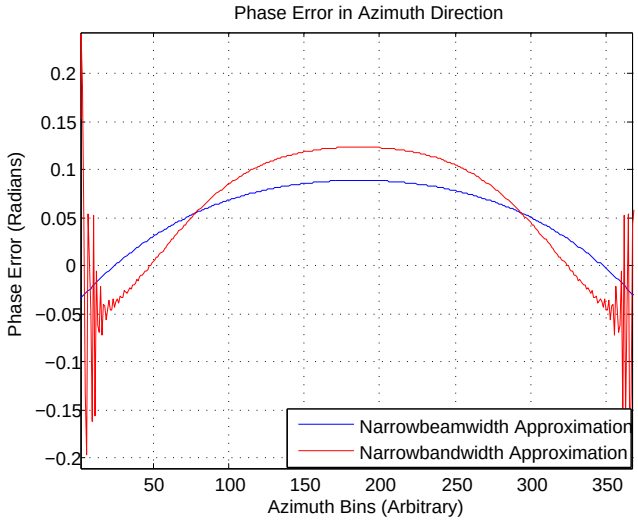

Figure 4.18: Phase Error in Azimuth Direction for a Point at 45 m

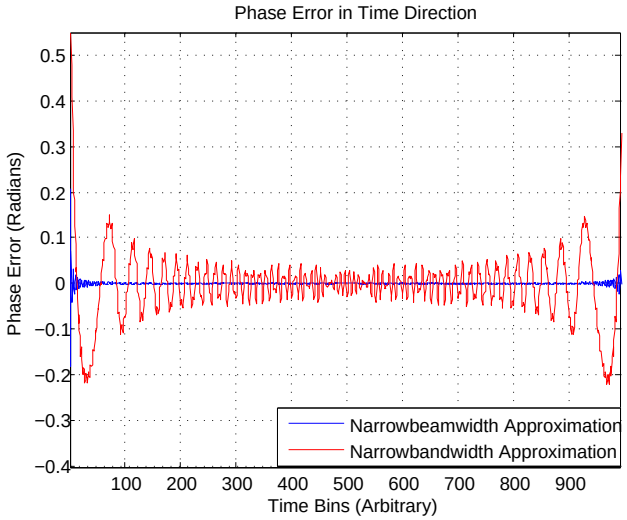

Figure 4.19: Phase Error in Time Direction for the Center Point

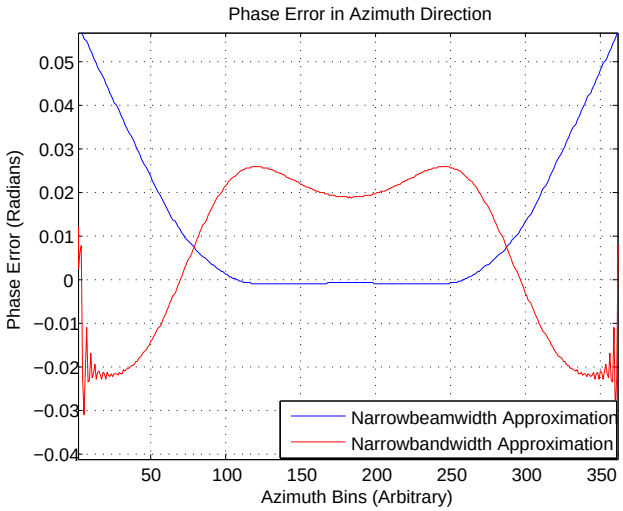

Figure 4.20: Phase Error in Azimuth Direction for the Center Point

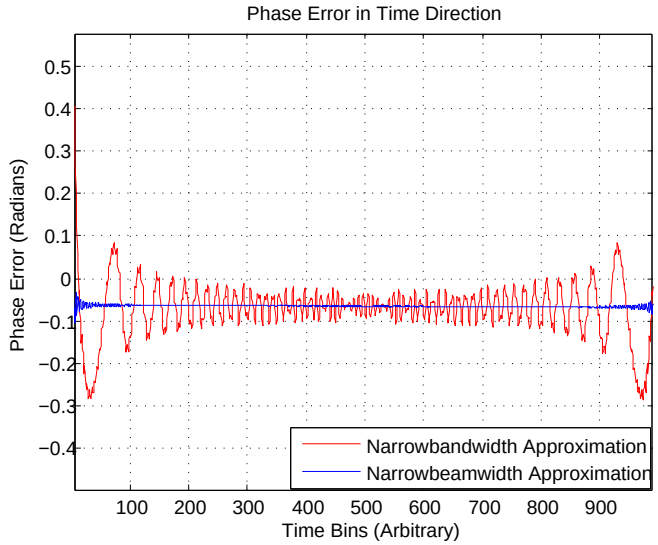

Figure 4.21: Phase Error in Time Direction for a Point at 450 m

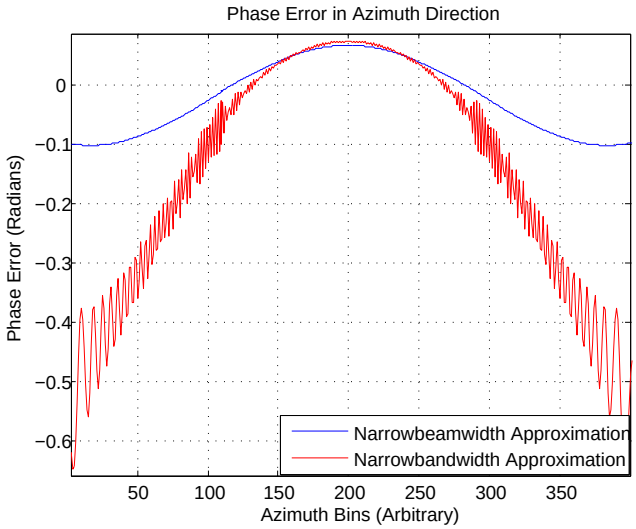

Figure 4.22: Phase Error in Azimuth Direction for a Point at 450 m

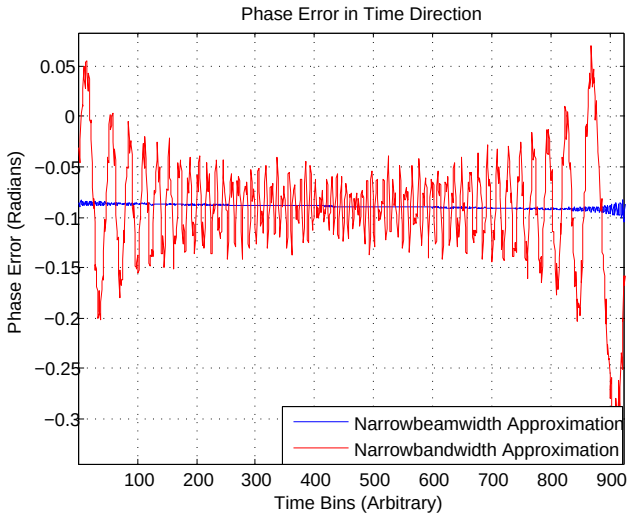

Figure 4.23: Phase Error in Time Direction for a Point at 45 m and 10° Aperture

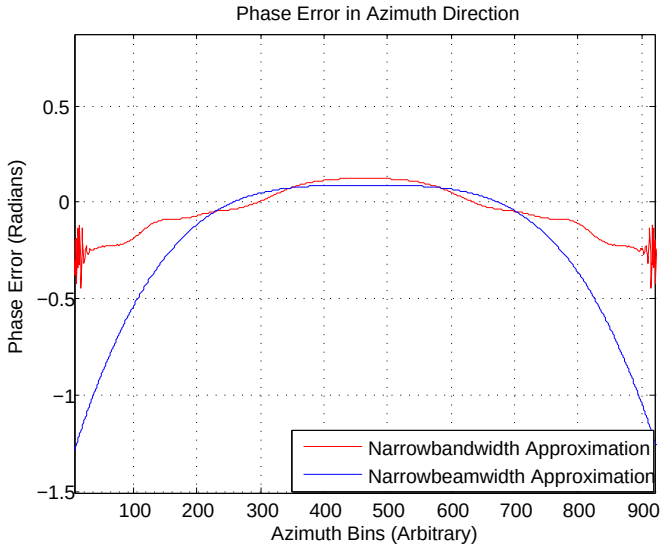

Figure 4.24: Phase Error in Azimuth Direction for a Point at 45 m and 10° Aperture

Chapter 5

Raw Data Simulation for Extended Scenes

5.1 Outline of the Chapter

This chapter discuses RD simulation for extended scenes. The case of an urban scene consisting of buildings placed on a rough terrain is used for simulation examples. The chapter is divided into two parts: The first part presents a description of rough surfaces. An electromagnetic model needed to calculate the reflected field from such an extended scene is also introduced. This model is used to simulate polarimetric data according to different scene parameters. The features of anisotropic building response that has already been reported in the literature, is also included in the simulation. Furthermore, an example in case of such a scene imaged with sensor trajectory deviations is presented. The second part of this chapter introduces RD simulation in an interferometric SAR configuration, alongwith examples concerning a flat surface as well as an urban scene consisting of a single building. Only geometric decorrelation is considered, however, the possibility of taking into account other sources of decorrelation is discussed.

5.2 Introduction to Surfaces

All the simulation examples considered so far consisted of a set of simple point scatterers, having a deterministic amplitude and phase, given in a reflectivity map. This was convenient to check the accuracy of the simulated RD by comparing phase in time and azimuth direction with that generated by a time domain simulator. However, in actual cases, the situation is much more different due to two main reasons:

- There are usually more than one scatterer within a resolution cell.
- A surface may be rough and due to this roughness, superposition of reflections from all these scatterers may result in a varying overall phase and/or amplitude.

Initially, the concept of roughness is explained by considering figure 5.1 that shows a wave impinging at an angle θ_1 on two points located at ground range positions of x_1 and x_2 and heights of z_1 and z_2, respectively, on a rough surface (the two positions can be considered to be inside a resolution cell). The wave is reflected at an angle θ_2 from both positions,

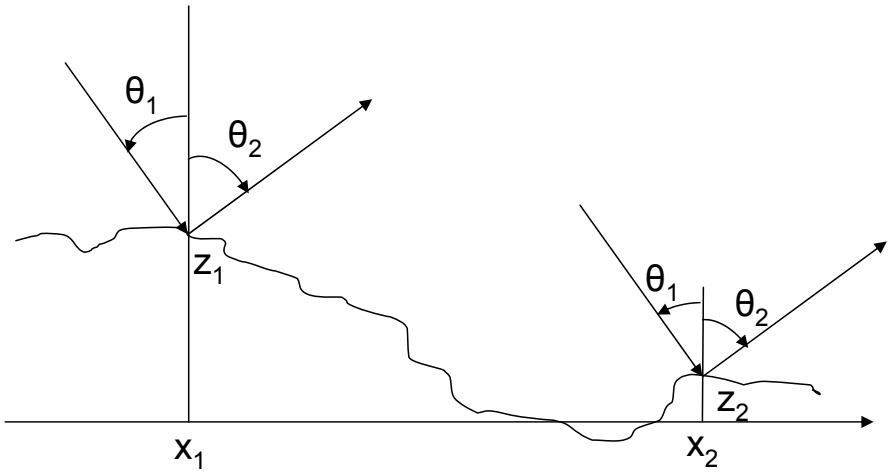

Figure 5.1: Reflection of Waves from a Rough Surface

and the phase difference resulting from the two points can be calculated as [55]

$$\Delta\phi = k_c\{(z_1 - z_2)(\cos\theta_1 + \cos\theta_2) + (x_2 - x_1)(\sin\theta_1 - \sin\theta_2)\} \tag{5.1}$$

where k_c is the wavenumber. The interference between the two reflected waves depends on the magnitude of $\Delta\phi$ compared with π. If it is much smaller that π, the waves will interfere constructively, whereas a phase difference comparable to π will lead to destructive interference. There is a coarse criterion called Rayleigh criterion that categorizes a surface into smooth or rough: If $\Delta\phi < \pi/2$, the surface is smooth, otherwise it is rough [55]. This leads to the conclusion that a surface's roughness depends mainly on the frequency and angle of the incident waves, as $\Delta\theta$ is dependant on these two features. In the following, the two surface categories are explained:

5.2.1 Smooth Surface

For a smooth surface, $z_1 = z_2$ and considering $\theta_1 = \theta_2$ (specular reflection), $\Delta\phi = 0$. There is only constructive interference, thus giving a strong reflection. If $\theta_1 \neq \theta_2$ (other than specular direction), destructive interference takes place as $\Delta\phi$ increases according to the next equation.

$$\Delta\phi = k_c\{(x_2 - x_1)(\sin\theta_1 - \sin\theta_2)\} \tag{5.2}$$

Therefore, the scattered field will be strong in the specular direction, and decreases gradually in other directions, that can be considered as a lobe. This specular field is also known as coherent field, due to its predictable and constant phase compared to the incident field.

5.2.2 Rough Surface

In case of a rough surface $z_1 \neq z_2$, although this difference may be small in case of a slightly rough surface. For the specular direction, the phase difference is given as

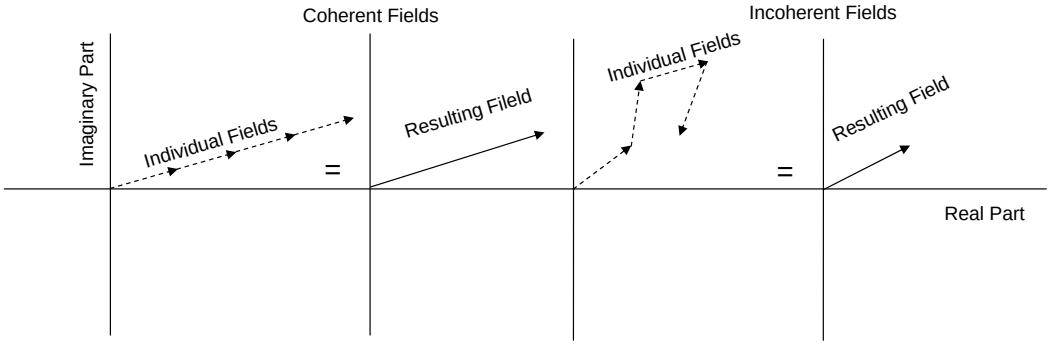

Figure 5.2: Addition of Coherent and Incoherent Fields [55]

$$\Delta\phi = 2k_c(z_1 - z_2)\cos\theta_1 \tag{5.3}$$

As long as it is much smaller than π, there will be constructive interference leading to a strong reflection. However, when it becomes larger (due to height difference $z_1 - z_2$), destructive interference occurs, thus reducing the amplitude of the reflected specular field. For non-specular directions, the phase difference varies over $0 - 2\pi$ for different reflected angles according to equation 5.1, thus giving rise to several reflections having no fixed phase relative to the incident wave phase. This field is also known as incoherent field, due to its lack of phase relationship with the incident field.

The reason for separately describing the coherent and incoherent field is that the two combine differently: Coherent fields add together in phase to give an amplitude that is equal to the sum of the amplitude of the individual components, whereas incoherent fields add together to give an amplitude that may be less than the amplitude of the individual components. This is shown in figure 5.2.

5.2.3 Description of a Rough Surface

A rough surface may be described in terms of its difference from a reference surface that may be chosen based on the surface type [55]. This difference is given by two measures: The spread of height about the reference surface, and its variations. The former may be described by a height probability distribution function $p(z)$ satisfying the following constraint:

$$\langle z \rangle = \int_{-\infty}^{\infty} zp(z)dz = 0 \tag{5.4}$$

where $\langle . \rangle$ is the averaging operation. The standard deviation of the height is given by

$$s_s = \sqrt{\langle z^2 \rangle} \tag{5.5}$$

Usually in the literature, Gaussian distribution having a certain standard deviation s_s is used to describe the height distribution and is given as [55]

$$p(z) = \frac{1}{s_s\sqrt{2\pi}} \exp(-\frac{z^2}{2s_s^2}) \tag{5.6}$$

It is symmetrical about zero meaning that Gaussian surfaces are distributed equally above and below the reference surface [55]. The second measure for surface roughness may be represented by the correlation function that describes the height change with slant-range (or ground-range) distance Δr (or Δx). It is defined as

$$C(\Delta r) = \frac{\langle h(r)h(r+\Delta r)\rangle}{s_s^2} \tag{5.7}$$

This correlation function has the property of $C(0) = 1$, and as Δr increases, $C(\Delta r)$ decreases gradually to zero, with the decay rate depending on the distance over which points become uncorrelated, whereas, the decay shape depends on the surface type. The surface correlation can also be assumed to be Gaussian and is given as

$$C(\Delta r) = \exp\left(-\frac{\Delta r^2}{l_s^2}\right) \tag{5.8}$$

where l_s is called the correlation length and is the distance over which the correlation falls by $1/e$, where $e = \ln^{-1}(1)$. Other types of correlation functions can also be used.

5.3 Total Electromagnetic Field from a Surface

A resolution cell may be considered large compared to the wavelength of the incident waves, and can be divided into a number of scatterers having a size comparable to the wavelength. The reflected echo from each cell is the result of coherent summation (adding both amplitude and phase) from each of them. This result may vary from one resolution cell to another, thus causing a fluctuation over an image and leads to a granular appearance in an image called speckle [26], that can be reduced by speckle filtering [56]. An example is shown in figure 5.3, where the first figure shows a speckled image, while the second image shows the speckle filtered image.

If there is no dominant scatterer in the resolution cell and the total number of scatterers is N, the total reflected signal from a resolution cell at position (r_m, y_n) can be considered as

$$\sigma(r_m, y_n) = \sum_{l=1}^{N} A_l \exp(j\phi_l) \tag{5.9}$$

where $A_l \exp(j\phi_l)$ is the contribution of the l^{th} scatterer. If N is large, then by central limit theorem, $\sigma(r_m, y_n)$ follows a zero-mean complex circular Gaussian distribution. $\Re\{\sigma(r_m, y_n)\}$ and $\Im\{\sigma(r_m, y_n)\}$ are normally distributed according to the following probability distribution:

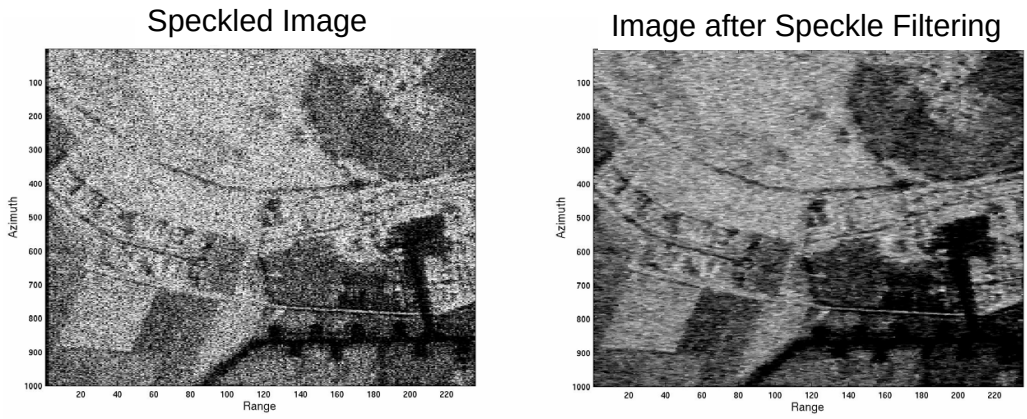

Figure 5.3: Speckled Image and Speckle Filtered Image

$$p[\Re\{\sigma(r_m, y_n)\}] = \frac{1}{s\sqrt{2\pi}} \exp\left[-\frac{\Re\{\sigma(r_m, y_n)\}^2}{s^2}\right] \tag{5.10}$$

$$p[\Im\{\sigma(r_m, y_n)\}] = \frac{1}{s\sqrt{2\pi}} \exp\left[-\frac{\Im\{\sigma(r_m, y_n)\}^2}{s^2}\right] \tag{5.11}$$

where

$$E[\Re\{\sigma(r_m, y_n)\}, \Im\{\sigma(r_m, y_n)\}] = 0 \tag{5.12}$$

and

$$E[\Re\{\sigma(r_m, y_n)\}^2] = E[\Im\{\sigma(r_m, y_n)\}^2] = s^2/2 \tag{5.13}$$

The magnitude and the phase of $\sigma(r_m, y_n)$ can also be considered as Rayleigh and uniformly distributed, respectively [1]. Equation 5.9 actually represents the incoherent part of the field as it is randomly distributed. The coherent part may be represented by a simple mean μ, thus representing the total field given in a reflectivity map as

$$\sigma(r, y) \sim \{\mathbf{N}(\mu_r, s^2/2) + j\mathbf{N}(\mu_i, s^2/2)\} \tag{5.14}$$

where $\mathbf{N}(\mu, s^2/2)$ represents a normal distribution with mean μ and variance $s^2/2$.

Summarizing the preceding discussion, a field reflected from a random rough surface may be considered as Gaussian whose mean and variance can be calculated by an electromagnetic model. This model itself takes as input the surface variance, its correlation length and the angle of incidence. The output mean and variance (included in the S matrix), that actually represent the coherent and incoherent parts, respectively, of the backscattered field are used to calculate the backscattering coefficients (given in the reflectivity

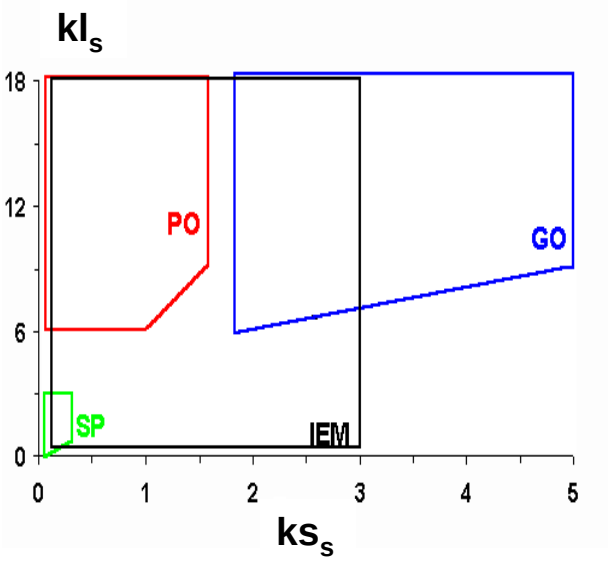

Figure 5.4: Validity Domain of Electromagnetic Models [85]

map) for different polarizations by generating Gaussian variables as follows:

$$\sigma_h(r,y) \sim S_{hh}\{\mathbf{N}(\mu_r,1/2) + j\mathbf{N}(\mu_i,1/2)\} \tag{5.15}$$

$$\sigma_v(r,y) \sim S_{vv}\{\mathbf{N}(\mu_r,1/2) + j\mathbf{N}(\mu_i,1/2)\} \tag{5.16}$$

$$\sigma_{hv}(r,y) \sim S_{hv}\{\mathbf{N}(\mu_r,1/2) + j\mathbf{N}(\mu_i,1/2)\} \tag{5.17}$$

$$\sigma_{vh}(r,y) \sim S_{vh}\{\mathbf{N}(\mu_r,1/2) + j\mathbf{N}(\mu_i,1/2)\} \tag{5.18}$$

The different models existing in literature are Small Perturbation Model (SPM), Integral Equation Model (IEM), Physical Optics (PO) and Geometric Optics (GO) models. Each model has a different validity domain that is shown in figure 5.4, depending on the product of wavenumber and roughness parameters [85].

An important question often ignored is the minimum number of scatterers to be present inside a resolution cell for the presented speckle model to be applicable, as the central limit theorem cannot be applied if N is small. [11] uses the results of [57] to infer this number to be 4, whereas [58] gives this number as approximately greater than 5. From these results, the limiting factor can be seen as the resolution of SAR. In case of a high resolution (less than five times the wavelength), the number of scatterers such that each scatterer's size is comparable to the size of the wavelength may be less than this limit and thus the above mentioned speckle model cannot be applied and alternative models have to be used. Another reason for non-gaussian speckle model is in case the surface correlation length is greater than or comparable to the resolution cell [56] and N may be considered small. This situation is still under investigation for SAR [59].

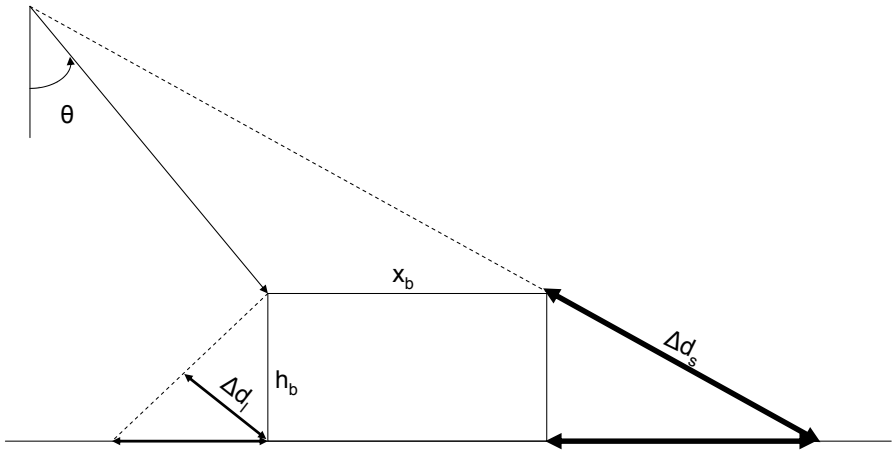

Figure 5.5: Geometry of the Imaged Building in Ground-Range Height Domain

5.4 Extended Scene-Polarimetric Case

An extended scene consisting of a ground surface and a building having a flat roof is used for simulation examples and is shown in figures 5.5 and 5.6.

The building length in the along-flight direction is represented by y_b, its height by h_b, its width in ground-range direction by x_b (in slant-range by r_b), its orientation angle (compared to the along-flight direction) by ψ and the incidence angle at the building wall by θ. There are certain features in a SAR image of such a scene that shall be explained as follows:

Layover

It corresponds to an inversion of geometry [1] and overlap of the points in an image that are at the same slant-range distance but different ground range positions and heights as shown in figure 5.5. In this case, part of the roof and all of the wall fall in front of the building wall and there is an overlap between the ground and the roof. The length in the slant range is given by [60].

$$\Delta d_l = h_b \cos\theta \tag{5.19}$$

Shadow

It corresponds to a region that produces no backscattered signal as shown in figure 5.5. Its length in slant range can be expressed as [60]

$$\Delta d_s = \frac{h_b}{\cos\theta} \tag{5.20}$$

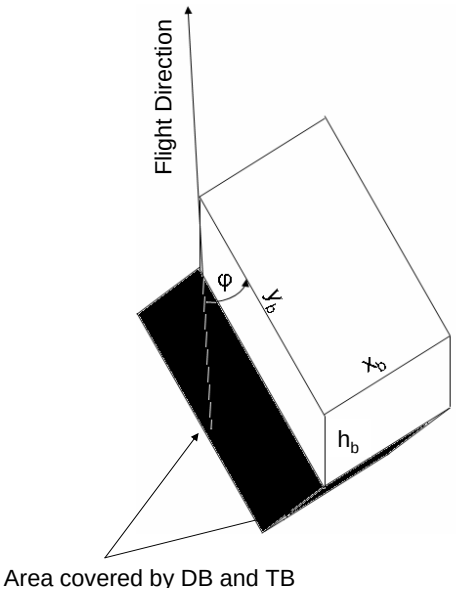

Figure 5.6: Geometry of the Imaged Building showing the Orientation Angle

Foreshortening

This effect leads to dilation and compression of different features in slant range as compared to ground range. It is mainly due to the relationship between slant range and ground range given by equation 1.11 and is dominant for objects near the sensor (near range).

5.4.1 Reflection Phenomena

There are different phenomena arising due to reflection of the incident electromagnetic waves that are considered here:

- Single bounce (SB) from ground, wall and roof.
- Double bounce (DB) due to reflections from wall going towards the ground and reflected towards the sensor (Path A-B-C-D) and vice versa (Path D-C-B-A).
- Triple bounce (TB) from the wall-ground-wall (Path A-B-C-B-A) or ground-wall-ground (Path D-C-B-C-D) reflections towards the sensor.

The area of the wall is $y_b h_b$, whereas the area covered on the ground by both DB and TB is $y_b h_b \tan\theta \cos\psi$ and $x_b h_b \tan\theta \cos(\pi/2 - \psi)$ [15], for the wall facing the sensor and for the wall facing away from the sensor, respectively. The latter part is small if the building is oriented at a small angle ψ. The next figure shows the distribution of DB and TB as described in [61]. Two points should be noticed:

1. The distance traveled by waves from DB is equivalent to the case of the waves incident and reflected from the building-wall interaction point. Thus, all the field reflected from the area is spread over one range bin (represented by O_1 in figure 5.7).

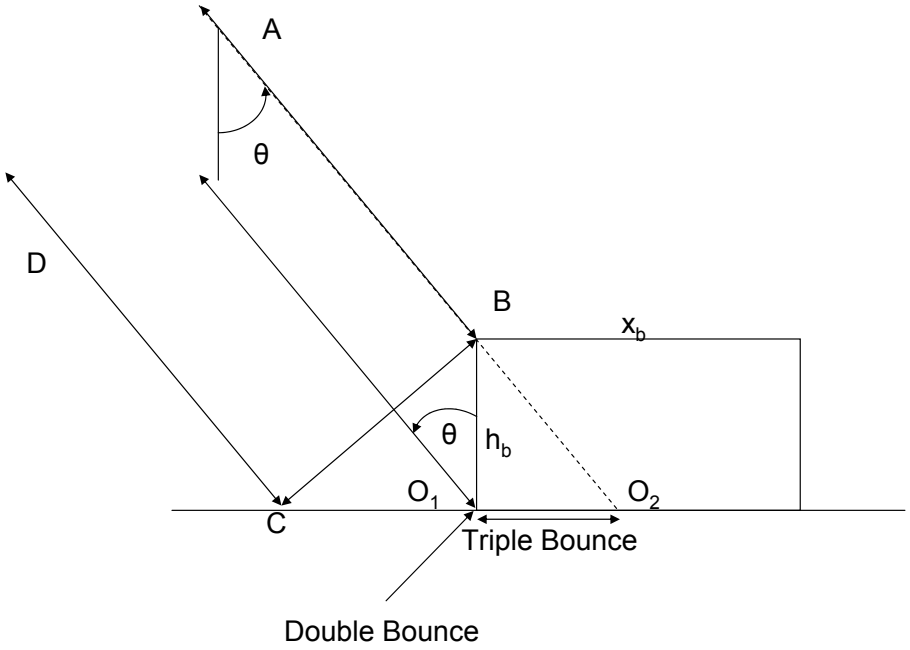

Figure 5.7: Spatial Location of DB and TB

2. The distance traveled by the waves in case of TB varies between the wall-ground interaction point and a point corresponding to the building height projected on ground, as shown in figure 5.7 by O_2. The total reflected field is spread uniformly over the range bins from O_1 to O_2.

An existing model proposed by [15], based on PO and GO model, is used. The wall and the roof are considered to be totally smooth in the model, however, in this thesis, the latter is considered to be slightly rough (as in [62]) and its contributions are also calculated. PO model is preferred, as the GO model is unrealistic in a typical urban environment. However, the wall is assumed to be completely smooth and the field reflected by it is calculated using a GO model. The model gives the coherent (μ) and incoherent part (s) for each of the phenomena considered and calculates the S matrix. These values are recalled here for reference (equations 5.21-5.29). The parameters given in table 3.1 are used for a building with dimensions shown in figures 5.5 and 5.6, placed on a terrain of dimensions x_g and y_g, in the ground-range and azimuth directions, respectively. The subscripts sbw, sbg and sbr represent single-bounce from wall, ground and roof respectively, whereas db and tb represent DB and TB contributions, respectively. s_r^2 and s_g^2 are the roof and ground variance, respectively and l_r and l_g refer to their respective correlation lengths.

$$\mu_{sbw} = y_b h_b \cos\psi \mathrm{sinc}(2k_c y_b \sin\psi) \tag{5.21}$$

$$\mu_{sbg} = \exp(-2k_c^2 s_g^2 \cos^2\theta) y_g x_g \tag{5.22}$$

$$s_{sbg}^2 = \exp(-4k_c^2 s_g^2 \cos^2\theta) y_g x_g \pi l_g^2 \sum_{p=1}^{+\infty} \frac{(2k_c s_g \cos\theta)^{2p}}{p!p} \exp\left\{-\frac{(2k_c l_g \sin\theta)^2}{4p}\right\} \tag{5.23}$$

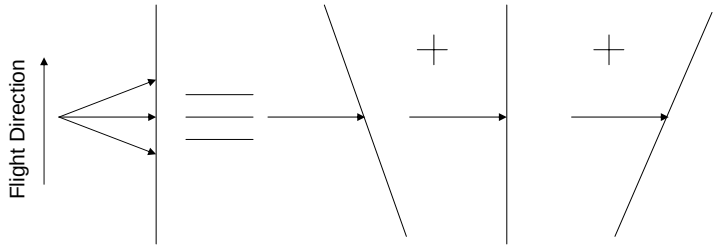

Figure 5.8: Rotation of an Object during the Imaging Process

$$\mu_{sbr} = \exp(-2k_c^2 s_r^2 \cos^2\theta) y_b x_b \tag{5.24}$$

$$s_{sbr}^2 = \exp(-4k_c^2 s_r^2 \cos^2\theta) y_b x_b \pi l_r^2 \sum_{p=1}^{+\infty} \frac{(2k_c s_r \cos\theta)^{2p}}{p!p} \exp\left\{-\frac{(2k_c l_r \sin\theta)^2}{4p}\right\} \tag{5.25}$$

$$\mu_{db} = \exp(-2k_c^2 s_g^2 \cos^2\theta) y_b x_b \tan\theta \cos\psi \mathrm{sinc}(2k_c y_b \sin\psi) \tag{5.26}$$

$$s_{db}^2 = \exp(-4k_c^2 s_g^2 \cos^2\theta) y_b x_b \tan\theta \cos\psi \pi l_g^2 \sum_{p=1}^{+\infty} \frac{(2k_c s_g \cos\theta)^{2p}}{p!p} \exp\left\{-\frac{(2k_c l_g \sin\theta \sin\psi)^2}{4p}\right\} \tag{5.27}$$

$$\mu_{tb} = \exp(-2k_c^2 s_g^2 \cos^2\theta) y_b x_b \tan\theta \cos\psi \mathrm{sinc}(2k_c y_b \sin\psi) \tag{5.28}$$

$$s_{tb}^2 = \exp(-4k_c^2 s_g^2 \cos\theta^2) y_b x_b \tan\theta \cos\psi \pi l_g^2 \sum_{p=1}^{+\infty} \frac{(2k_c s_g \cos\theta)^{2p}}{p!p} \exp\left\{-\frac{(2k_c l_g \sin\theta \sin\psi)^2}{4p}\right\} \tag{5.29}$$

The presence of a sinc function is due to the integration over a rectangular patch, shown in [63]. The model gives values corresponding to the narrowbeamwidth assumption, i.e. all the incident waves in the beamwidth have more or less the same aspect (instantaneous squint) angle at the building wall. In a more accurate representation, this is no longer applicable as the beam consists of angles varying from $-\theta_y/2$ to $\theta_y/2$ that can be seen equivalent to a narrowbeamwidth configuration and a building rotating from $-\theta_y/2$ to $\theta_y/2$ towards the along-flight direction. Note that this is due to the azimuth angular motion of a scene relative to the SAR as described in [64]. The rotation causes the reflection to be maximum, when the incident waves direction and the building wall are orthogonal to each other.

This rotating/widebeamwidth effect can be taken into account by replacing ψ in the above equations by a range of angles varying from $-\theta_y/2-\psi$ to $\theta_y/2-\psi$. It can be demonstrated by calculating values of μ_{db} and s_{db}^2 that are shown in the next figure for angles of $\psi = 0°$ and $\psi = -4°$. It is evident that the coherent part is shifted and centered around ψ. The same sinc function has been reported in [65], [66], [67] for dihedral reflectors that represents double bounce, whereas [62] refers to this as a non-stationary phenomenon present

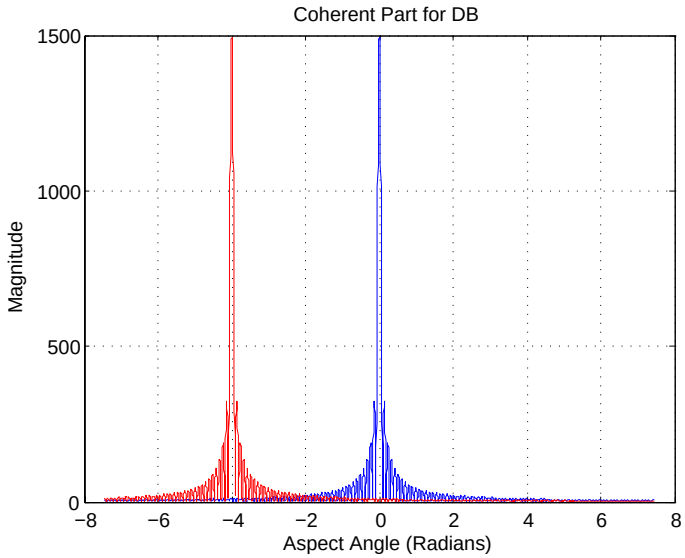

Figure 5.9: Coherent Part of DB for 2 Different Orientations

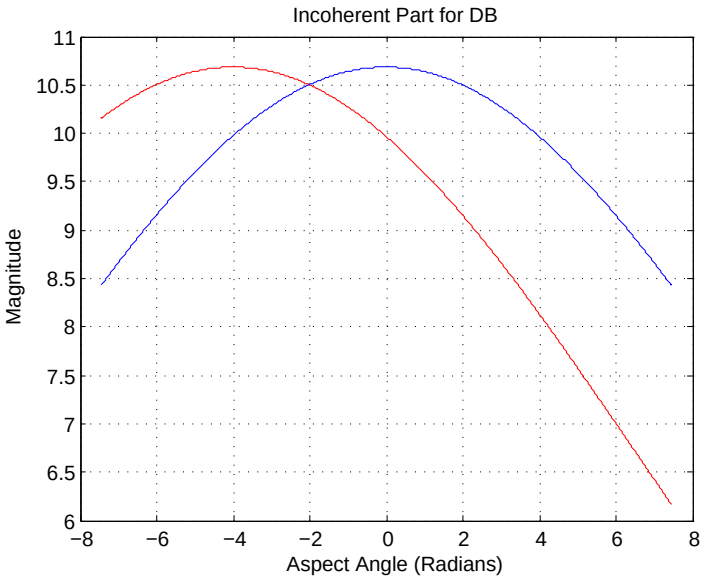

Figure 5.10: Incoherent Part of DB for 2 Different Orientations

in SAR images of urban areas. The incoherent part does not show a big dependance on ψ and hence it is assumed to be constant during the imaging process.

The shifting effect for the coherent part is apparent only in equations 5.21, 5.26-5.29. The reason is that the ground and roof surfaces are assumed to be flat, whereas this effect arises only in case of a sloped surface, which in the above case is a wall. For a tilted roof, it can also appear and in the layover region, it may be present due to single bounce reflections from the wall. Note that the flat surfaces also "rotate" during the imaging process, however, the reflected waves' intensity does not change with the "rotation angle".

5.4.2 Generation of Reflectivity Map

The reflectivity map $\sigma(r, y)$ can be divided into several parts, with each of them corresponding to one phenomenon, and the respective coherent $\sigma^c(r, y)$ and incoherent $\sigma^i(r, y)$ parts, i.e.

$$\begin{aligned}\sigma(r,y) &= \sigma^c_{sbw}(r,y) + \sigma^c_{sbg}(r,y) + \sigma^c_{sbr}(r,y) + \sigma^c_{db}(r,y) + \sigma^c_{tb}(r,y) \\ &\quad + \sigma^i_{sbg}(r,y) + \sigma^i_{sbr}(r,y) + \sigma^i_{db}(r,y) + \sigma^i_{tb}(r,y)\end{aligned} \tag{5.30}$$

Simple geometric relations and equations 5.19-5.20 are used to calculate the area and its position in slant range for each part of the reflectivity map. In case of the building roof, the incidence angle does not change much as the building length is small and hence can be assumed constant. The corresponding coherent and incoherent parts are calculated by means of a PO model for each phenomenon (GO model for the wall) and spread regularly over all the area in a straightforward manner, and then multiplied by a Gaussian variable, [(1)]different for each phenomenon, having a mean of 0 and a variance of 1.

A description for the generation of the incoherent part for SB from roof is as follows:

$$\sigma^i_{sbr}(r,n) = \frac{s_{sbr}}{P_r Q_r \sqrt{2}} \{\mathbf{N}(0,1) + j\mathbf{N}(0,1)\} \sum_{p,q} \delta(r - r_p, y - y_q) \tag{5.31}$$

where P_r and Q_r refer to the total number of bins the roof covers in the slant range and azimuth directions, respectively and the summation term represents the position of the roof. The same process applies for the incoherent part of SB from ground, DB and TB.

For the coherent part, the aspect angle varying feature of the reflected field has to be taken into account. By considering $k_y \approx 2k_c \sin\theta_{as}$, where $\theta_{as} = \arcsin(\frac{k_y}{2k_c})$, the coherent part for the wall such that $\psi = 0$ may be written in frequency domain as

$$\sigma^c_{sbr}(r,k_y) = \frac{\mu_{sbw}}{P_r} \mathrm{sinc}(k_y y_b) \sum_p \delta(r - r_p) \tag{5.32}$$

Thus, it may be generated directly in the frequency domain using the values of θ_{as} given

[(1)] As described in [82], the speckle should be applied at the resolution cell level, otherwise spatial correlation should be taken into account

earlier, to have a linear phase spacing in the frequency domain followed by an IFFT, that leads to

$$\sigma^c_{sbr}(r,y) = \frac{\mu_{sbw}}{P_r Q_r}\text{rect}(\frac{y}{y_b})\sum_p \delta(r-r_p) \tag{5.33}$$

For a building oriented at an angle ψ, $\theta_{as} \Longrightarrow \theta_{as} - \psi$ and equation 5.33 may be modified as

$$\sigma^c_{sbr}(r,k_y) = \frac{\mu_{sbw}}{P_r}\text{sinc}(k_y y_b - k_\psi y_b)\sum_p \delta(r-r_p) \tag{5.34}$$

where

$$k_\psi = 2k_c \sin\psi \tag{5.35}$$

The IFFT of equation 5.34 gives

$$\sigma^c_{sbr}(r,y) = \exp(jk_\psi y)\frac{\mu_{sbw}}{P_r Q_r}\text{rect}(\frac{y}{y_b})\sum_p \delta(r-r_p) \tag{5.36}$$

$\sigma^c_{sbr}(r,y)$ is then rotated by an angle ψ to take into account the geometrical orientation of the building that results in

$$\sigma^c_{sbr}(r,y) = \exp(jk_\psi y)\frac{\mu_{sbw}}{P_r Q_r}\sum_{p,q} \delta(r-r_p, y-y_q) \tag{5.37}$$

The same procedure applies to coherent parts for DB and TB. For SB reflection from the ground and roof, the coherent part can be generated (due to absence of aspect angle dependency) by simply dividing the calculated variance over the area, ignoring any shifted sinc function. The coherent and incoherent parts are calculated for each polarization to give the corresponding reflectivity maps.

A point that immediately comes to mind is that the coherent part can be directly generated using the time domain representation given in equation 5.37. However, an inconvenience may arise as the exponential multiplication gives rise to a circular shift and in case of a large ψ, it will cause the sinc function to wrap around, instead of being shifted "out" of the imaging aperture angle. This can be overcome by high oversampling, however, the simplest and the most accurate way is to generate it in frequency domain as shown in figure 5.11.

5.4.3 Examples

The parameters in table 3.1 are used for simulation examples. A few changes have been made in accordance with the characteristics of a real scene, that are shown in table 5.1 alongwith the roughness parameters. As a first example, a non-oriented building having length, width and height of 70m, 10m and 20 m, respectively is simulated. The reflectivity maps for co-polar polarization channels are depicted in figure 5.12. Note that the intensity level in hh is slightly higher than that in vv. hv and vh polarization channels are not

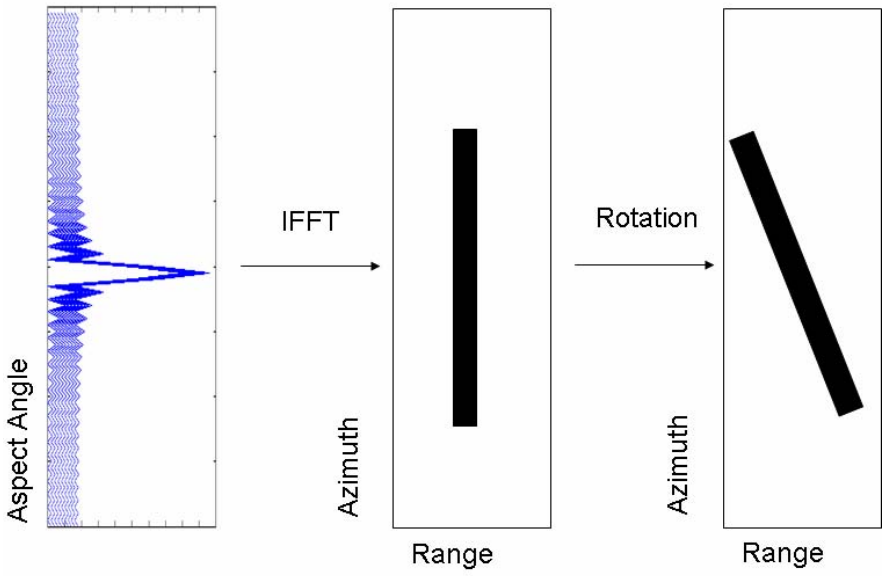

Figure 5.11: Generation of Reflectivity Map

Table 5.1: Scene and Simulation Parameters (Stripmap SAR without any Squint)

Sensor Height	3391 m	Sensor Velocity	89 ms^{-1}
s_g	0.02	l_r	0.25 m
s_r	0.005	l_g	0.06 m

shown, as from the PO model, the contribution from ground, roof and wall is zero. The presence of a high double bounce can be remarked, that is localized at one range position. Raw data is generated using these reflectivity maps and OKA is used to generate the respective images that are shown in figure 5.13. Images can also be generated directly by convolving the reflectivity map with a reference image-phase inclusion operation. Figure 5.14 shows the amplitude and phase of the co-polar coherence that resembles the results given in the literature [18].

In the second example, a building at an orientation of 4° is simulated and all the above mentioned steps are repeated. It can be seen that in this case the intensity levels are slightly lower than those in the case of non-oriented building, as the reflection area for DB and TB decreases.

5.4.4 Subaperture Analysis

The presence of sinc functions in the coherent part of the buildings' response gives rise to an aspect angle changing response, that has been included in the simulation as described in

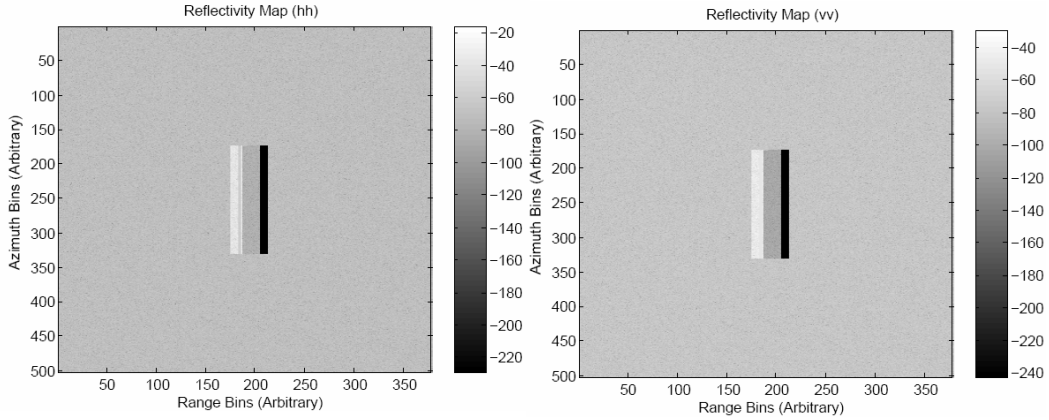

Figure 5.12: Generated Reflectivity Map for a Non-oriented Building

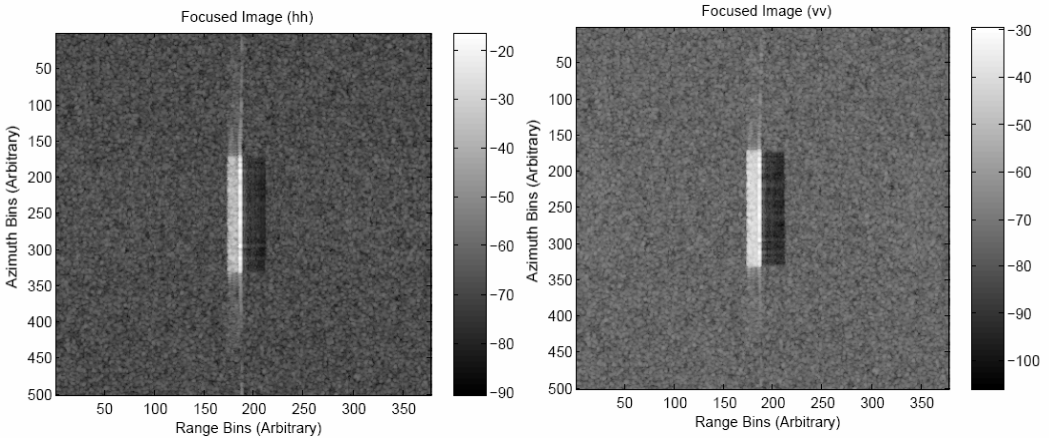

Figure 5.13: Focused Images for a Non-oriented Building

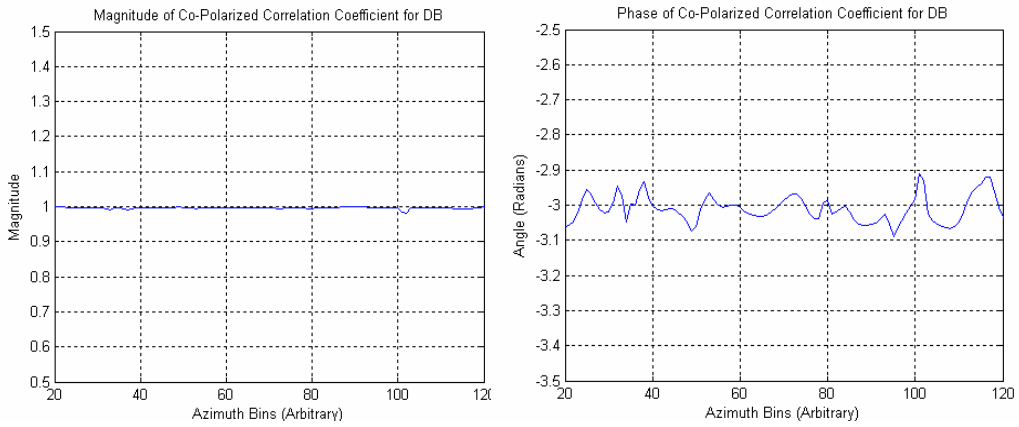

Figure 5.14: Magnitude and Phase of Co-polarized Correlation Coefficient for DB

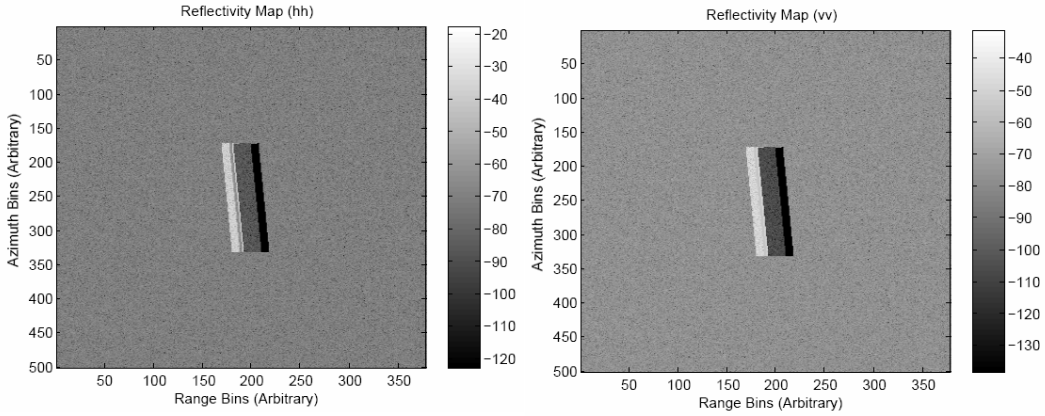

Figure 5.15: Generated Reflectivity Map for an Oriented Building

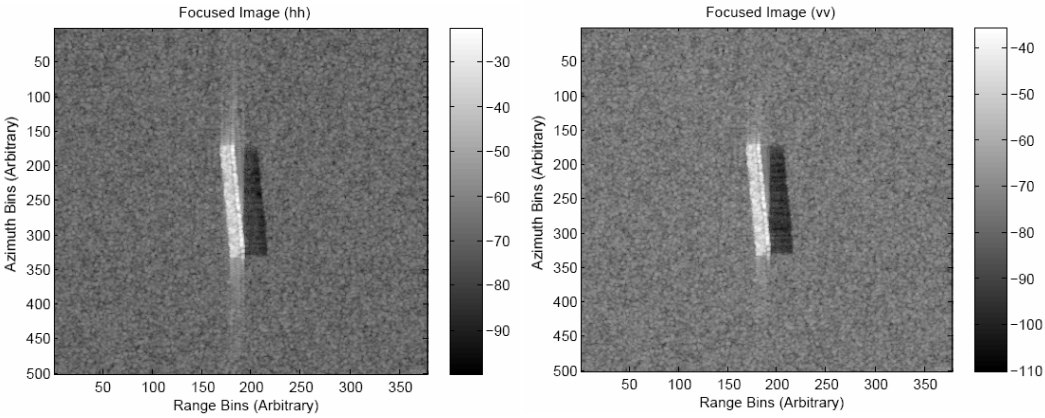

Figure 5.16: Focused Images for an Oriented Building

Table 5.2: Scene Parameters for Subaperture Analysis

Building	y_b	x_b	h_b	ψ
A	70 m	10 m	20 m	0°
B	70 m	10 m	20 m	2°
C	70 m	10 m	20 m	−2°
D	70 m	10 m	20 m	6°
E	70 m	10 m	20 m	−6°

the preceding discussion. In order to check the effectiveness of the simulation, a subaperture analysis is carried out that consists of dividing the azimuth beamwidth in different parts, which is equivalent to imaging the building from different range of aperture angles, but with a lower azimuth resolution [16]. This can be seen by the following relationship between the aspect angle and the azimuth wavenumber:

$$\theta_{as} = \arcsin\left(\frac{k_y}{2k}\right) \tag{5.38}$$

Thus, dividing the azimuth frequency spectrum of RD into N_{sa} parts leads to the following aspect angle ranges:

$$\Delta\theta_{asp} = [\theta_y/2 - (p-1)\Delta\theta_y, \theta_y/2 - p\Delta\theta_y] \tag{5.39}$$

for $p = 1...N_{sa}$ and $\Delta\theta_y = \theta_y/N_{sa}$.

In [16], equation 5.38 has been approximated by

$$\theta_{as} \approx \arcsin\left(\frac{k_y}{2k_c}\right) \tag{5.40}$$

that requires the conditions $\frac{\Delta k}{k_c} << 1$ and $2k\sin\theta_{as} << 1$ to be satisfied. For equal distribution of energy in all the subapertures, the varying transmitted wavenumber should be taken into account as in equation 5.38. This is demonstrated in figure 5.17, where the solid lines show the subaperture formation according to equation 5.38, while the dotted lines show the formation according to equation 5.40. It is apparent that the subapertures formed by solid lines lead to equal distribution of energy, that is important in case of a large azimuth beamwidth. Moreover, these subapertures avoid any "spill-over" of energy, an effect that arises in case of the apertures formed by the dotted lines. This can be important especially in case of presence of any coherent part of spectrum at the subaperture boundaries.

For the purpose of illustration, the aperture angle was increased from 4° to 6° and 5 buildings were simulated at different orientations according to table 5.2. The reflectivity

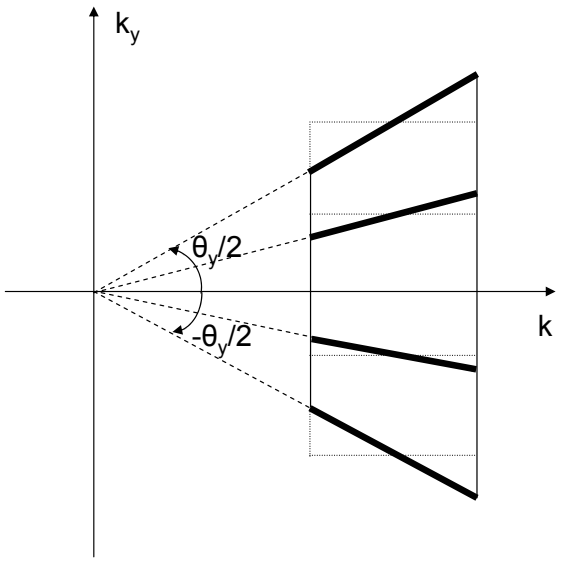

Figure 5.17: Subaperture Formation

map, corresponding image for vv channel and in Pauli basis are shown by figures 5.18 - 5.20, respectively.

Three subapertures of 2° each were formed, corresponding to an angle range of 3° to 1° (subaperture 1), −1° to 1° (subaperture 2), and −1° to −3° (subaperture 3). A subaperture analysis will show a change in DB response, that will be highest in different subapertures for different orientations. TB and wall response change also, however, they are weaker than the DB, and are, therefore, less noticeable, e.g., in subaperture 1, buildings oriented from 3° to 1° will show the highest response.

As predicted, building B has the highest DB intensity in subaperture 1, shown by figure 5.21, whereas for buildings A and C, it is highest in subapertures 2 and 3, shown by figures 5.22 and 5.23, respectively. For buildings D and E, the response remains stable as their orientation angles (−6° and 6°) are not covered within the azimuth beamwidth (−3° to 3°). The incorporation of this anisotropic behavior means that time-frequency analysis can be carried out on the simulated data, unlike [61].

5.4.5 Simulation in case of Motion Errors

A complete scene consisting of a building shown in figure 5.12 was used for RD simulation using the method presented in figure 4.15. The trajectory deviations have the sinusoidal form described in section 4.5.1 with a higher maximum amplitude. The simulated RD was used for image formation using the CSA and the resulting images with and without MoCo are shown in figure 5.24. The effects of motion errors are visible, which cause a spreading of the image in the azimuth direction. After MoCo, the image is well focused.

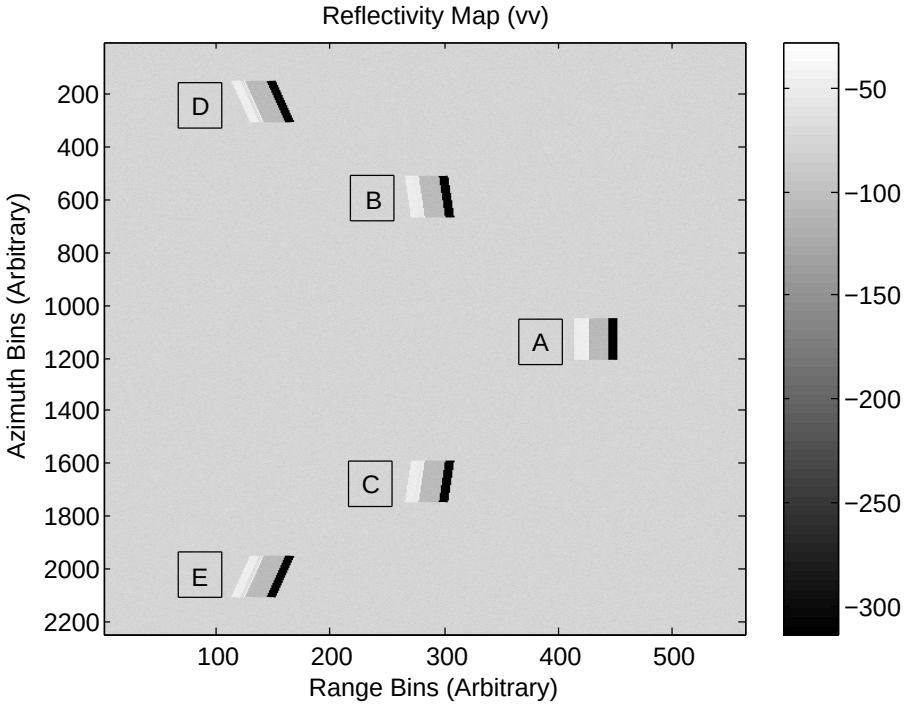

Figure 5.18: Generated Reflectivity Map for Buildings Oriented at Different Angles

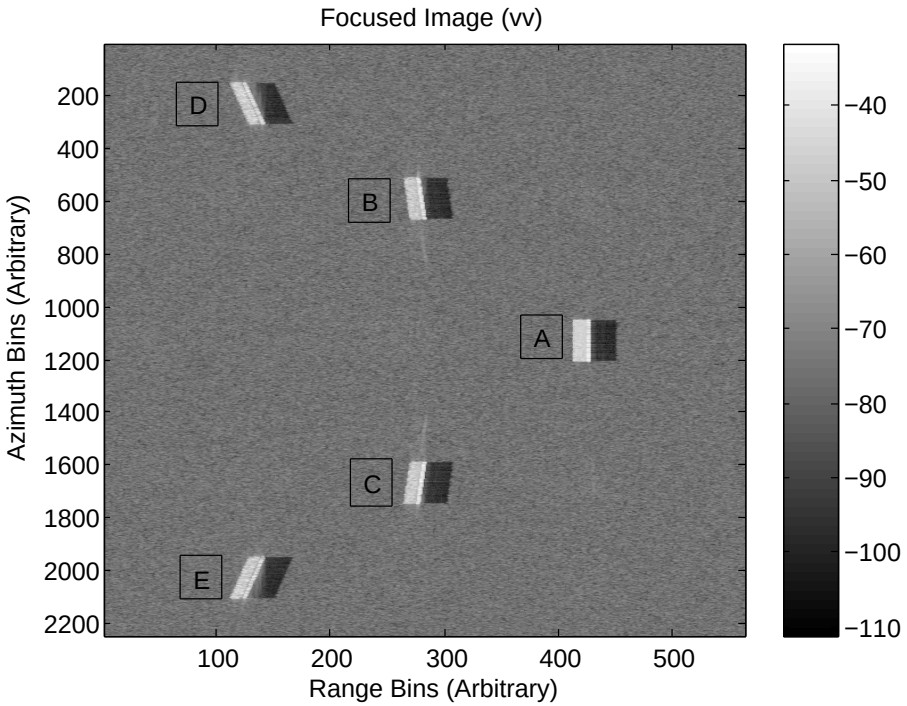

Figure 5.19: Focused Image for Buildings Oriented at Different Angles

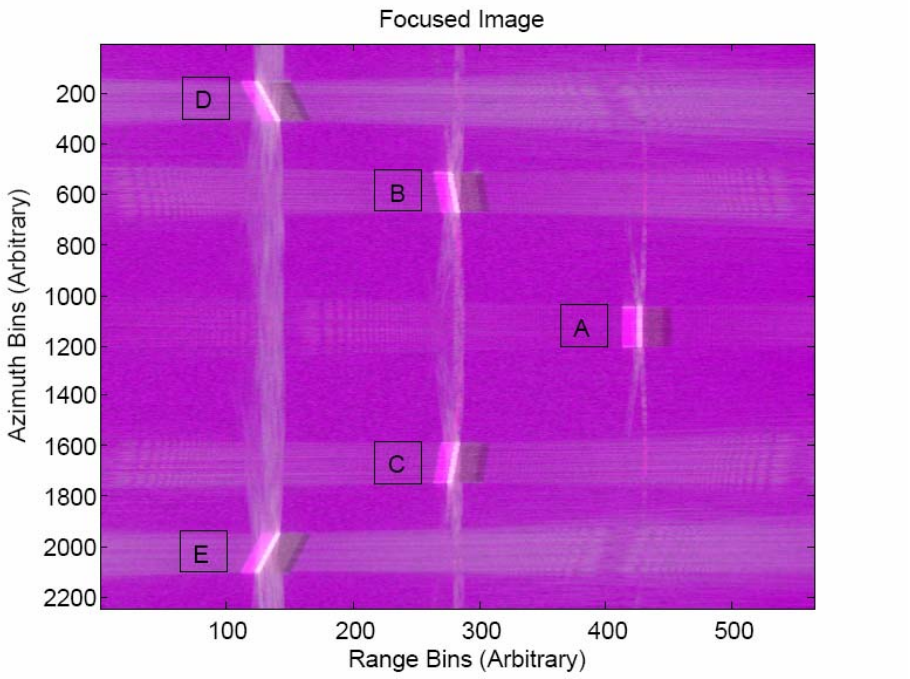

Figure 5.20: Focused Image in Pauli Basis for Buildings Oriented at Different Angles

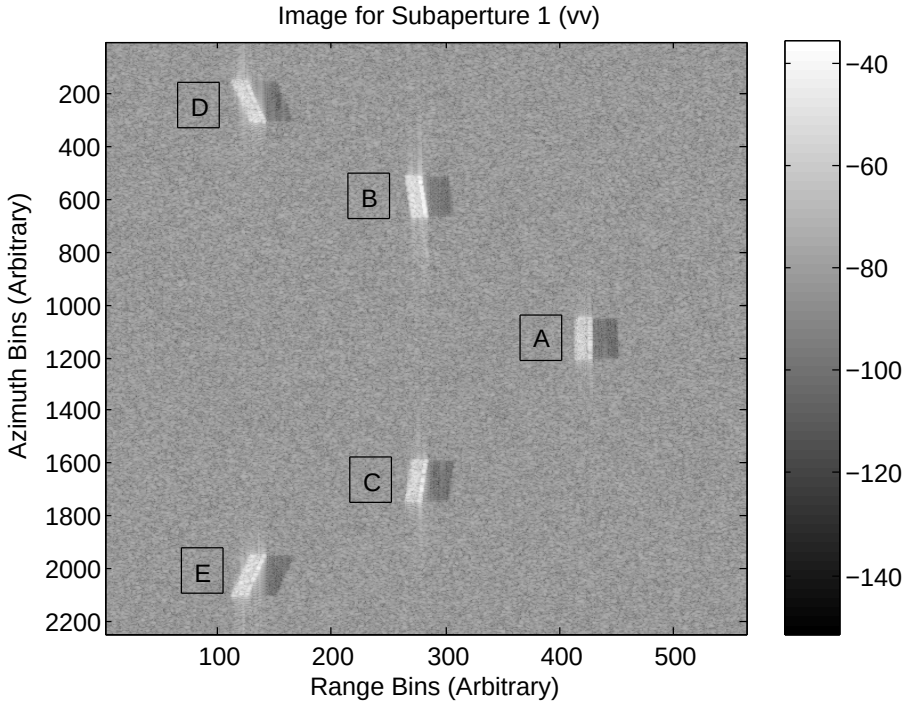

Figure 5.21: Focused Image in Subaperture 1

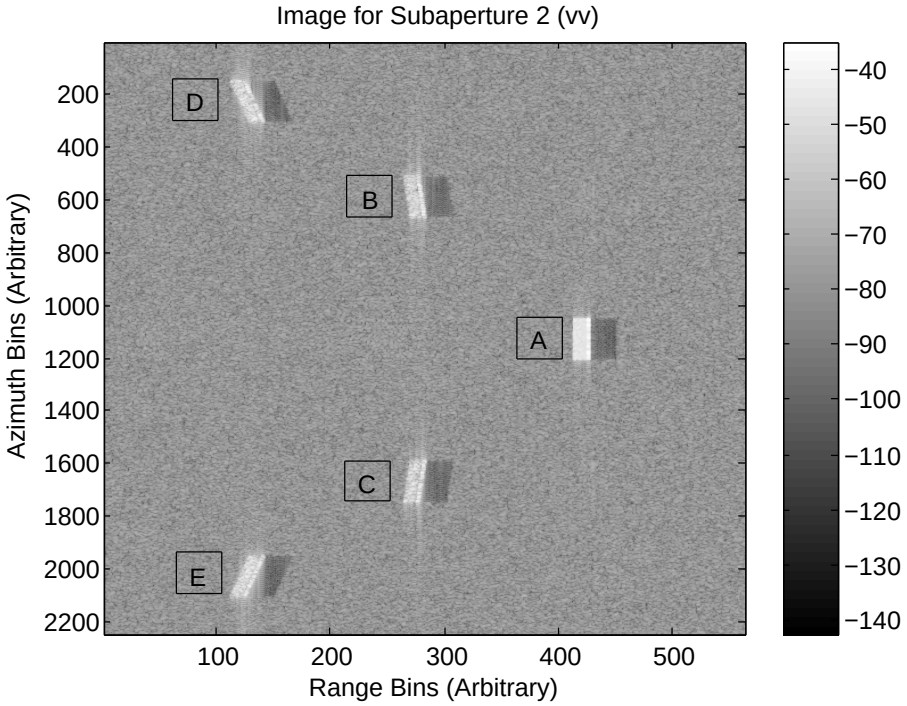

Figure 5.22: Focused Image in Subaperture 2

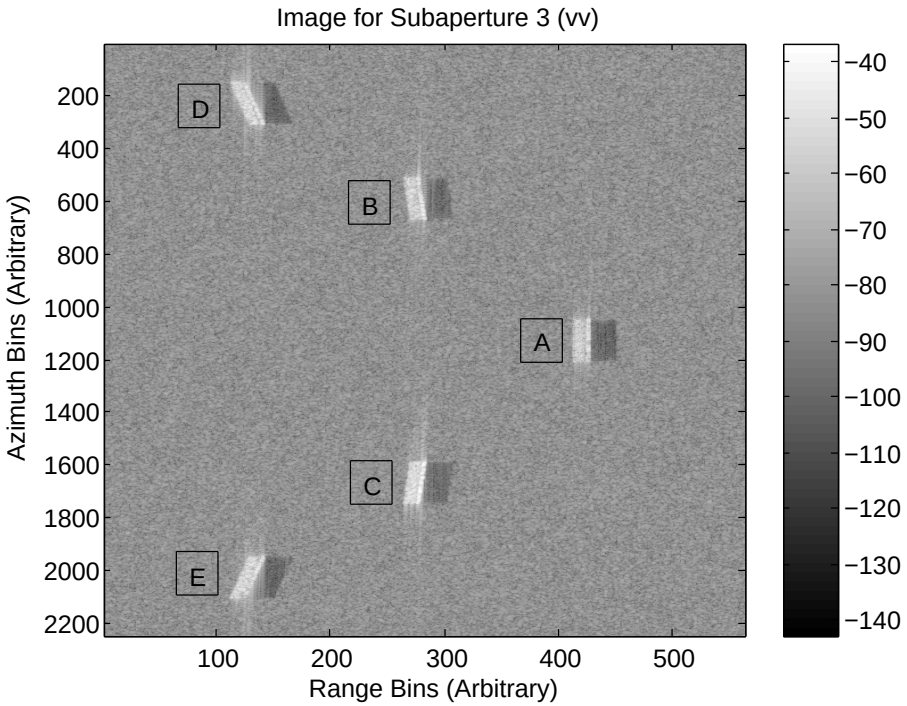

Figure 5.23: Focused Image in Subaperture 3

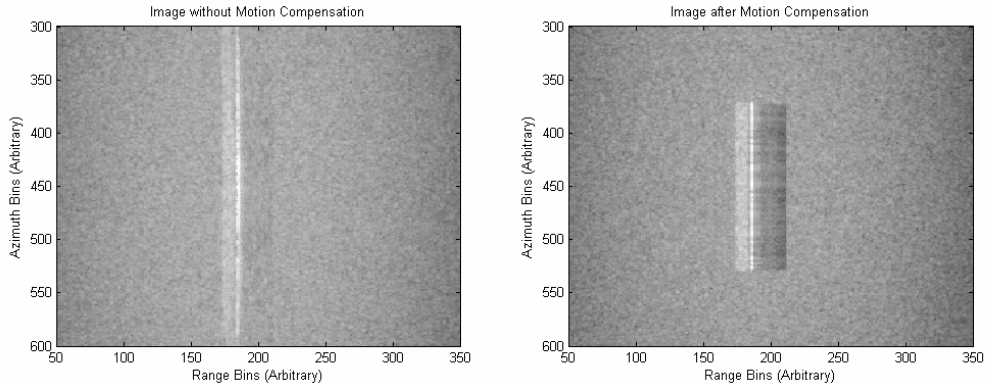

Figure 5.24: Images, without MoCo and after MoCo

5.4.6 Introduction to Interferometric SAR RD Simulation

As described in [1], [68], [69], [70], there exists decorrelation between the master and slave images. This may be due to different factors, such as misregistration (m), difference of imaging geometry (g), temporal decorrelation (t-scene changes between two different acquisitions), thermal noise (s), etc. The total correlation can be expressed as the product of the individual correlations gives as follows:

$$\gamma_i(r_m, y_n) = \gamma_{im}(r_m, y_n)\gamma_{ig}(r_m, y_n)\gamma_{it}(r_m, y_n)\gamma_{is}(r_m, y_n) \tag{5.41}$$

For simulation examples in this section, misregistration errors and system noise are neglected, although they can be taken into account easily. In addition, an urban scene in single-pass configuration is considered and temporal changes may be very small in this case.

InSAR RD simulation consists of generating RD twice according to the master and slave configurations and taking into account the geometric correlation between them. [29] presents an RD simulator based in time domain, whereas [36], [71] present an RD simulator based in the frequency domain. [72] presents a simulator that generates a slave image from a master image. [17] presents an interferogram generator. Here a frequency domain approach based on chapter 3 will be presented that follows the work of [17] and [71] and in the following discussion, the case of geometric decorrelation, its expression and its physical interpretation will be demonstrated for a flat scene by considering the master and slave RD, and the 2D FFT of the master and slave images.

$$s_1(t, y) = \sum_{m,n} \sigma(r_m, y_n) p\left(t - \frac{2\sqrt{r_m^2 + (y - y_n)^2}}{c}\right) \tag{5.42}$$

$$s_2(t, y) = \sum_{m,n} \sigma(r_m, y_n) p\left(t - \frac{2\sqrt{(r_m - \Delta r_m)^2 + (y - y_n)^2}}{c}\right) \tag{5.43}$$

$$I_1(k_r, k_y) = |P(\Delta k)|^2 \sum_{m,n} \sigma(r_m, y_n) \exp(-jk_r r_m - jk_y y_n) \tag{5.44}$$

$$I_2(k_r, k_y) = |P(\Delta k)|^2 \sum_{m,n} \sigma(r_m, y_n) \exp(-jk_r (r_m - \Delta r_m) - jk_y y_n) \tag{5.45}$$

Equation 5.45 consists of an extra exponential term as compared to equation 5.44, that can be divided in two parts:

$$\exp(jk_r \Delta r_m) = \exp\{j2(\Delta k_r + k_c)\Delta r_m\} \tag{5.46}$$

The term involving Δk_r arises due to difference of imaging geometry and represents a position shift. The second term, which is infact the interferometric phase term causes a range frequency shift, that gives rise to geometric decorrelation, as RD range spectrum in the range direction covers different parts of the reflectivity spectrum [69] for both the cases. This frequency shift can be calculated as the derivative of the term $\exp(jk_c \Delta r_m)$ with respect to range, i.e.,

$$\Delta f_m = \frac{c}{2\pi} \frac{d(k_c \Delta r_m)}{dr} = \frac{ck_c}{2\pi} \frac{d(\Delta r_m)}{dr} \tag{5.47}$$

The derivative of Δr_m can be calculated by considering the distance between two points at positions m and $m+1$ given by [1] as

$$\Delta r_m - \Delta r_{m+1} = \frac{b \cos\theta_m (r_m - r_{m+1})}{\tan\theta_m} \tag{5.48}$$

that leads to

$$\Delta f_m = \frac{cb \cos\theta_m}{\lambda_c \tan\theta_m} \tag{5.49}$$

Knowing the relation that convolution of two rectangular pulses leads to a triangular function, this frequency shift is used to calculate the expression of the geometric correlation that is given as

$$\gamma_{ig}(r, y) = 1 - \left| \frac{\Delta f_m}{B_t} \right| \tag{5.50}$$

Note that this decorrelation is caused by a change of distance for each point in the two configurations, that gives rise to the extra exponential term $\exp(jk_c \Delta r_m)$. This term, on one hand serves to provide height estimation, and on the other hand causes a decorrelation, that degrades the interferogram quality, but can be removed [73], [74], [75] using range spectral shift.

RD simulation consists of generating the RD pair with the correct correlation. This can be achieved by generating similar master and slave reflectivity map (having a mean μ and variance s) and multiplying the latter with the term $\exp\{j\Delta k_c \Delta r_m\}$ as shown in the

following equation. The incoherent part of the reflectivity map is multiplied by the same Gaussian random variables as the exponential part causes the decorrelation and subsequently equations 3.13-3.15 are used for RD simulation:

$$\sigma_1(r,y) = \mu + s/\sqrt{2}\{\mathrm{N_{1r}}(0,1) + j\mathrm{N_{1i}}(0,1)\}\sum_{m,n}\delta(r-r_m, y-y_n) \tag{5.51}$$

$$\sigma_2(r-\Delta r, y) = \mu + s/\sqrt{2}\{\mathrm{N_{1r}}(0,1) + j\mathrm{N_{1i}}(0,1)\}\sum_{m,n}\exp(-j2k_c\Delta r_m)\delta(r-r_m-\Delta r_m, y-y_n) \tag{5.52}$$

where $\mathrm{N_{1r}}$ and $\mathrm{N_{1i}}$ represent the real and imaginary parts of the speckle, respectively. In order to avoid wraparound effects of frequency shift, the reflectivity map should be upsampled by a factor of atleast 2 in the range direction as described in [71]. The simulation process is carried out twice to generate the RD set that can be processed to generate the image pairs. If the aim of the simulation process is to study only the interferometric SAR image pairs, this can be carried out by generating the image pair using equation 3.14. Note that [17] is based on this methodology, however it uses only the reflectivity map for the interferogram generation and does not take the band limiting effect of a SAR system into account that may not be sufficient if the phenomenon of range spectral shift is to be studied.

5.4.6.1 Simulation Examples

Interferometric SAR image pairs are simulated for a plane surface of size $100m$ in ground range and azimuth directions, and a height of $20m$. The SAR parameters are the same as those shown in table 3.1 and the baseline is 1 m. An example of the interferogram phase after flat earth phase removal is shown in figure 5.25. In order to check the accuracy of the simulation, the estimated height for a fixed azimuth position is also plotted.

The next example consists of a simulation for an urban scene comprising a single building. This scene is divided into three parts according to the incidence angle, as the range frequency shift is different for different angles:

- Ground surface, DB and TB having incidence angles of $\arccos\left(\frac{H}{r}\right)$.
- Roof having incidence angles of $\arccos\left(\frac{H-h_b}{r}\right)$.
- Wall having incidence angles of $\arccos\left(\frac{H-z_w}{r}\right)$ where $0 \leq z_w \leq h_b$.

All these parts are multiplied separately with an exponential term, generating by using the respective incidence angles in equation 1.55 and then used for RD simulation. Two cases were considered:

1. A building of length, width and height of 70m, 10m and 20m, respectively. In this case all the roof falls infront of the DB, leaving TB as the dominant reflection phenomenon as shown by the reflectivity map in figure 5.26. The height estimates

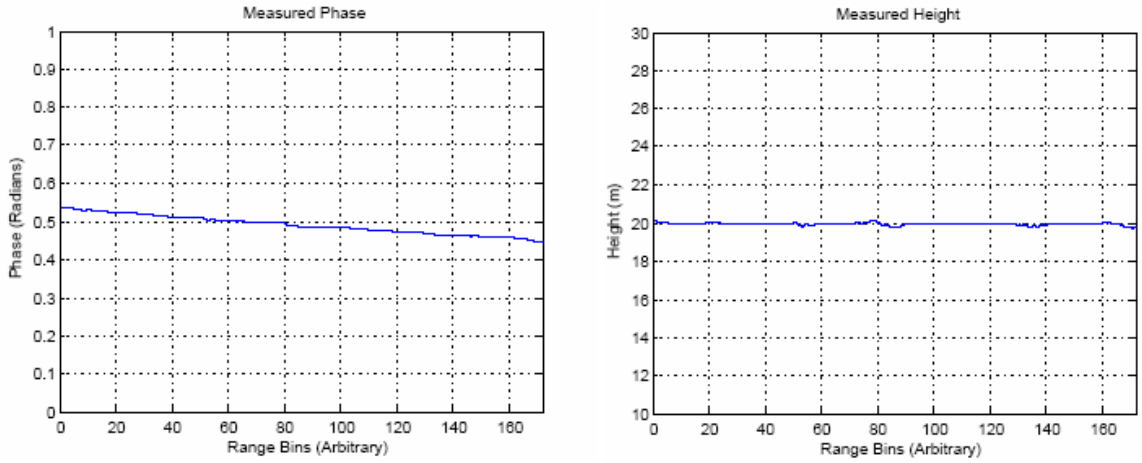

Figure 5.25: Measured Phase and Estimated Plane Height

from the simulated interferogram for a single azimuth position are also shown. Note that the height estimate decreases at and after the DB position (as DB and TB represent the ground position).

2. A building of length, width and height of 70m, 40m and 20m, respectively. The resulting height estimates for one azimuth position is shown in figure 5.27. In the case there is only a part of the roof in front of the DB. Thus the height estimate decreases near the DB position and then again increases, eventually falling to zero.

Comments

In the presented simulation examples, three main sources of decorrelation are neglected:

1. Misregistration errors.

2. System noise that causes decorrelation according to the following expression [1]:

$$\gamma_{is}(r,y) = \frac{1}{\sqrt{\{1+snr_1(r,y)^{-1}\}\{1+snr_2(r,y)^{-1}\}}} \tag{5.53}$$

where snr_1 and snr_2 represent the signal to noise ratio in the master and slave images, respectively.

3. Topography that results in an extra phase shift and thus an extra decorrelation factor [76]. If the surface is Gaussian with a variance s_g, this factor can be written as (according to [77])

$$\gamma_{it}(r,y) = \exp\left\{-\frac{1}{2}\left(\frac{2\pi cb\cos\theta_m s_g}{\lambda_c \tan\theta_m}\right)^2\right\} \tag{5.54}$$

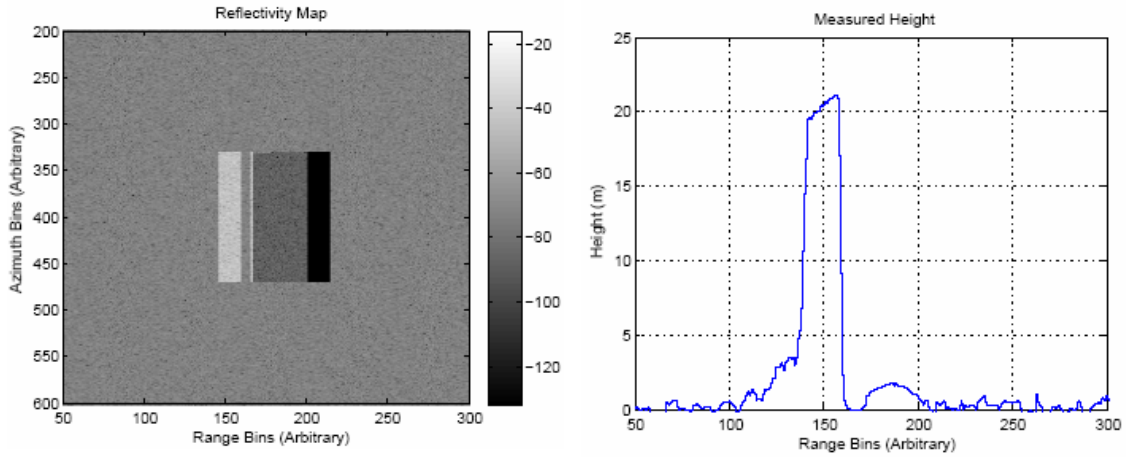

Figure 5.26: Reflectivity Map of Building (width=10m) and Estimated Height

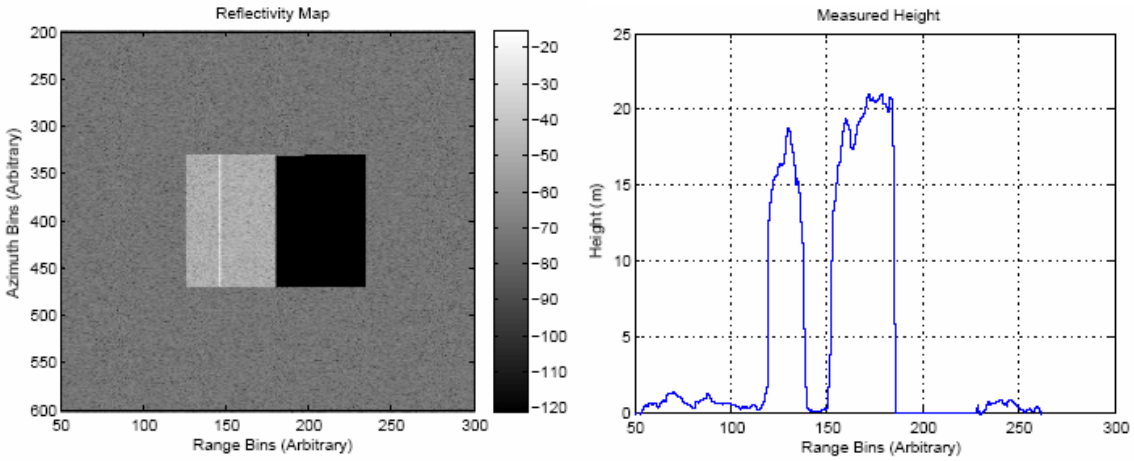

Figure 5.27: Reflectivity Map of Building (width=40m) and Estimated Height

Misregistration error effects can be included by a very high resampling of the slave reflectivity map to take into account the position shifts caused by the difference of the master and slave geometries. The remaining two effects can be taken care of by decorrelating the master and the slave reflectivity map by a factor of $\gamma_{it}\gamma_{is}$. This can be carried out by considering two complex random sequences n_1 and n_2. Another sequence n_3 that is correlated to n_1 by a factor of γ can be generated by

$$n_3 = \gamma n_1 + \sqrt{1-\gamma^2} n_2 \tag{5.55}$$

Thus equation 5.55 is used to generate a correlated random sequence $\mathrm{N}_2(0,1)$ that is used for slave reflectivity map generation described as follows:

$$\mathrm{N}_{2\mathrm{r}}(0,1) = \gamma_{it}\gamma_{is}\mathrm{N}_{1\mathrm{r}}(0,1) + \sqrt{1-(\gamma_{it}\gamma_{is})^2}\mathrm{N}(0,1) \tag{5.56}$$

$$\mathrm{N}_{2\mathrm{i}}(0,1) = \gamma_{it}\gamma_{is}\mathrm{N}_{1\mathrm{i}}(0,1) + \sqrt{1-(\gamma_{it}\gamma_{is})^2}\mathrm{N}(0,1) \tag{5.57}$$

$$\sigma_2(r-\Delta r, y) = \mu + s/\sqrt{2}\{\mathrm{N}_{2\mathrm{r}}(0,1) + j\mathrm{N}_{2\mathrm{i}}(0,1)\}\sum_{m,n}\exp(-j2k_c\Delta r_m)\delta(r-r_m-\Delta r_m, y-y_n) \tag{5.58}$$

This concept can be further extended for Polarimetric Interferometric SAR RD simulation by considering the total correlation to be a product of polarimetric and interferometric correlation [78]. The former is taken care of by the electromagnetic model used, whereas the latter can be generated using equation 5.55 for each polarization.

5.5 Conclusions

This chapter applied the techniques proposed in the preceding chapters to a realistic scene, consisting of a single and multiple buildings placed on a rough ground. The presence of an anisotropic response in the azimuth direction was shown mathematically and included in the simulation to make it more realistic. A subaperture analysis was carried out to show this behavior in the simulated images. Interferometric SAR RD/image simulation was introduced that made use of spectral shift to generate geometric decorrelation.

Conclusions and Outlook

This thesis has presented fast SAR raw data simulation and given examples for the case of airborne stripmap mode and broadside geometry.

Chapter 1 presented the mathematical relationships between different SAR system parameters and resolutions in the range and azimuth directions. The advantages of a chirp signal were described and it was shown that the sensor movement and the corresponding data storage leads to the presence of an azimuth chirp as well as an unwanted effect called range migration. The relationship between azimuth and transmitted frequency and the corresponding trapezium-like shape was demonstrated and basic points about interferometry and polarimetry were explained as well.

In chapter 2, frequency domain processing was introduced by a subpatch approach. It was shown that this subpatch approach involves accuracy, computational complexity trade-off. As a result, two of the main frequency domain processing algorithms, the Omega-k and the Chirp Scaling algorithms were explained. The change of 2D spectrum, before and after image formation was also demonstrated.

Chapter 3 examined raw data simulation in different domains. It was shown that the two dimensional frequency domain is the best one in terms of accuracy and computational efficiency. Two variants were proposed: The first one uses partial summation, while the second one replaces this summation by an interpolation. A relationship between the reflectivity map and the corresponding SAR image was shown, that actually leads to the conclusion that image formation algorithms can be reversed to generate raw data. It was also shown that RD for a moving object can be generated by a geometric transformation and interpolations.

Chapter 4 explained image formation and raw data simulation in the presence of motion errors. Two different approximate approaches were proposed for the latter purpose and analyzed to find validity limits in terms of system parameters and motion errors.

Chapter 5 applied the techniques proposed in the preceding chapters to a realistic scene, consisting of a building placed on a rough ground. The presence of an azimuth position varying response was shown mathematically and included in the simulation to make it more realistic. Interferometric SAR raw data/image simulation was introduced that made use of spectral shift to generate geometric decorrelation.

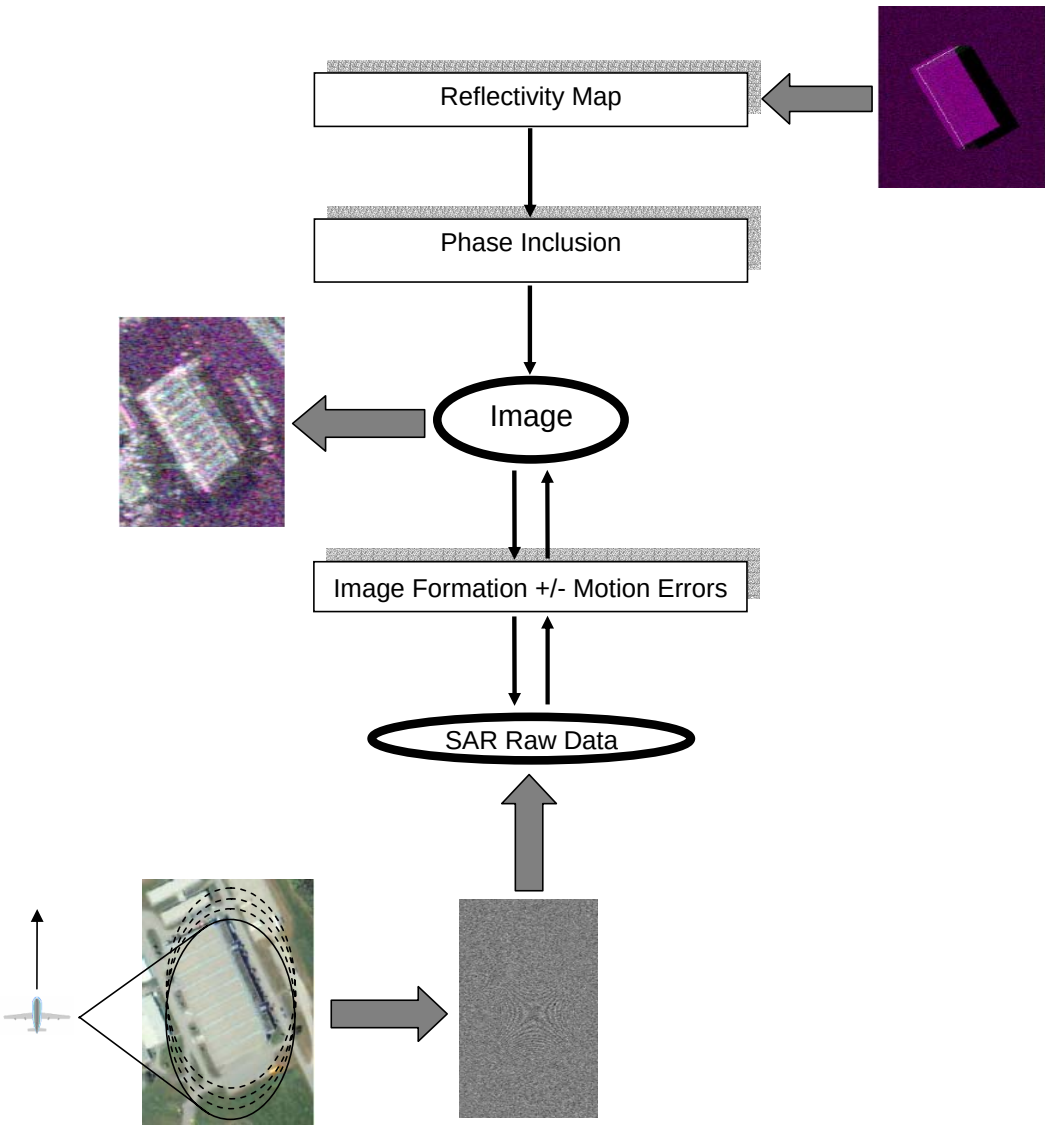

Figure 5.28: Conclusions in a Graphic Form

The above presented conclusions can be summarized by figure 5.28 and the following statements:

- Time domain simulation is the most accurate form of raw data simulation, however, it requires a lot of computations and is quite slow.
- The equation $S(k, k_y) = P(\Delta k) \sum_{m,n} \sigma(r_m, y_n) \exp(-j\sqrt{4k^2 - k_y^2} r_m - jk_y y_n)$ is the most accurate form for raw data simulation in the two dimensional frequency domain, and can offer significant computational savings in case the sensor trajectory is assumed to be ideal. Raw data for a moving object can also be simulated efficiently using this approach and a change of geometry.
- The equation $S(k, y) = P(\Delta k) \sum_{m,n} \sigma(r_m, y_n) \exp(-j2k\sqrt{r_m^2 + (y - y_n)^2})$ can reduce computational complexity compared to the time domain simulation, when used in partial summing operation to take into account trajectory errors. This may be useful in case of extended scenes. For a smaller azimuth aperture, the complexity may be further reduced by calculating Fourier Transforms in the azimuth direction at the expense of accuracy.
- An urban scene consists of an anisotropic azimuth response that can be modeled in terms of shifted sinc functions.
- Interferometric SAR image or raw data simulation can be carried out by using the two dimensional frequency domain approach and different types of decorrelation factors can be taken into account using spectral shift and partially correlated speckle.

Based on the terminology of [84], it can be said that the simulator presented in this thesis is a combination of "SAR processing oriented" and "SAR oriented" simulator.

The results and the knowledge gained through this thesis will be applied further for simulation of marine environment as observed by electromagnetic sensors as a part of the Brittany region project MODENA (Modelisation de l'observation à distance de l'environnement maritime), based on [49], [79], [80] and [81]. Moreover, there may be further extensions to this work that can either improve the results presented here, or take into accounts different cases that have not been considered. A few possibilities are:

- To extend the SAR raw data simulation for a squint-mode geometry. This can be taken into account using frequency shift in the azimuth direction. The use of this data may be used for different experiments alongwith the data for broadside geometry.
- To examine in detail the phase difference between raw data for a time domain simulator and the proposed simulation methods and reduce them, or find their dependency on different factors, such as upsampling factor, interpolator type, etc.
- To take into account shadow of a moving object. In this thesis, it has been assumed that a moving object is placed on a totally non-reflecting background. However, in more realistic cases, there is the shadowing effect of the object on the surrounding environment that will be quite pronounced in case of a big object or very high resolutions. This effect can be taken into account correctly by considering the shadow

to consist of two parts: One part, which remains covered throughout the imaging process and the second part that reflects partially during the raw data acquisition process, depending on the relative speeds between the sensor and the object. This may be taken into account by partially generating the reflectivity map in the frequency domain, as there is a direct relation between the azimuth distance and frequency domain.

- To generate raw data for multiple moving points, each having a different azimuth and range velocity. Until now, this process has remained elusive as varying range velocities cause varying azimuth frequency shifts that cannot be incorporated efficiently. For this purpose, the method presented in [49] may be studied as well as the time-frequency techniques [40], [51]. [48] can also be explored for this purpose.

- To include misregistration errors, topography and system noise effects in case of interferometric simulation and realistic scenes consisting of multiple buildings. An efficient way to include misregistration errors, instead of oversampling of the reflectivity map can also be explored based on the results of [19], [50].

- To extend the interferometric simulation to polarimetric interferometric case. This may be possible by using partially decorrelated speckle between the master and slave images for each polarization.

- To generate a backscattering model for an urban scene taking into account the presence of different structures such as doors, windows, tilted roof, etc. as well as the presence of grass and trees. A more accurate electromagnetic model having a wider validity domain may also be used. The results presented in [52] may be used as a reference.

- To simulate data and images for Multibaseline Interferometric and Polarimetric Interferometric case, using decorrelated speckle that may be tested with algorithms proposed in [53] for the former and [54] for the latter.

Appendix

Appendix A

Application of POSP to Calculate Raw Data Spectrum for a Single Point

In order to explain the POSP, a signal having the following form is considered:

$$g(t) = \exp\{j\Theta(t)\} \tag{A.1}$$

Its Fourier transform (FT) can be written as:

$$\begin{aligned} G(f) &= \int_{-\infty}^{+\infty} g(t)\exp(-j2\pi ft)dt \\ &= \int_{-\infty}^{+\infty} \exp(j\pi\Theta_m(t))dt \end{aligned} \tag{A.2}$$

and

$$\Theta_m(t) = \Theta(t) - 2\pi ft \tag{A.3}$$

If this phase is rapidly varying, the integral given by equation A.2 is almost zero as its positive and negative parts cancel each other. The only contribution to the integral will be around the stationary point t_0 where the derivative of the phase given by equation A.3 will be zero with respect to t, i.e.,

$$\frac{d\Theta_m(t)}{dt}|_{t=t_0} = 0 \tag{A.4}$$

A Taylor Series expansion of the phase in the vicinity of the stationary point gives [22]

$$\Theta_m(t) \approx \Theta_m(t_0) + \frac{(t-t_0)^2}{2}\Theta_m''(t_0) \tag{A.5}$$

where

$$\Theta_m^{''}(t_0) = \frac{d^2\Theta_m^{''}(t_0)}{dt^2}|_{t=t_0} \tag{A.6}$$

Making use of the relation

$$\int_{-\infty}^{+\infty} \exp\{ja(t-t_0)^2\}dt = \left(\frac{j\pi}{a}\right)^{1/2} \tag{A.7}$$

the integral given in equation A.2 can be written as follows:

$$G(f) = \left(\frac{j2\pi}{\Theta_m^{''}(t_0)}\right)^{1/2} \exp\{j\Theta_m(t_0)\} \tag{A.8}$$

This approximate form can be used to calculate the FT of a chirp signal and can be highly accurate if the TBP ($TBP = KT_p^2$) for the considered phase function is more than 100 [3].

The expression of the demodulated received signal by a SAR for a point at a position m (ignoring the range and azimuth envelopes and taking the reflectivity to be equal to one) is given as

$$s_m(t,y) = \exp\left\{-j2k_c d_m(y) + j\pi K_r\left(t - \frac{2d_m(y)}{c}\right)^2\right\} \tag{A.9}$$

where $d_m(y) = \sqrt{r_m^2 + (y-y_m)^2}$. The expression of the received signal in one-dimensional (1D) and two-dimensional (2D) wavenumber domains can be derived approximately using the POSP. Two cases will be considered: Small azimuth aperture and large azimuth aperture. In the former case, the calculations are much simplified.

A.1 Small Azimuth Aperture

In this case, the radar-target distance can be written as

$$d_m(y) \approx r_m + \frac{(y-y_m)^2}{2r_m} \tag{A.10}$$

using the parabolic approximation. Substituting this expression in equation A.9 gives

$$s_m(t,y) = \exp\left\{-j2k_c\left(r_m + \frac{(y-y_m)^2}{2r_m}\right) + j\pi K_r\left(t - \frac{2d_m(y)}{c}\right)^2\right\} \tag{A.11}$$

A.1.1 Azimuth Fourier Transform

The FT of the above equation in the azimuth direction can be computed by applying the POSP to the following integral:

$$S_m(t, k_y) = \int_{-\infty}^{\infty} s_m(t, y) \exp(-jk_y y) dy \tag{A.12}$$

The phase of the above integral can be approximated as

$$\Theta_m(y) \approx -2k_c r_m - k_c \frac{(y - y_m)^2}{r_m} - k_y y \tag{A.13}$$

Taking its derivative with respect to y and equating the result equal to 0 gives the following expression for y

$$y = y_m - \frac{r_m k_y}{2k_c} \tag{A.14}$$

The radar-target distance in the azimuth wavenumber domain can be written as

$$d_m(k_y) = r_m + \frac{r_m k_y^2}{8k_c^2} \tag{A.15}$$

making use of the preceding expression. The 1 D FT is written (by substituting the value of y in $\Theta_m(y)$) as:

$$S_m(t, k_y) = \exp\left\{-j2k_c r_m + j\frac{r_m k_y^2}{4k_c} - jk_y y_m + j\pi K_r \left(t - \frac{2d_m(k_y)}{c}\right)^2\right\} \tag{A.16}$$

A.1.2 2D Fourier Transform

The 2D FT is calculated by taking a further 1D FT of the preceding expression using the following integral:

$$S_m(f, k_y) = \int_{-\infty}^{\infty} S_m(t, k_y) \exp\{-j2\pi ft\} dt \tag{A.17}$$

The corresponding phase is

$$\Theta_m(t, k_y) = -2k_c r_m + \frac{r_m k_y^2}{4k_c} - k_y y_m + \pi K_r \left\{t - \frac{2d_m(k_y)}{c}\right\}^2 - 2\pi ft \tag{A.18}$$

Once again, taking a derivative with respect to t, and equating the result equal to 0 gives the following expression for t:

$$t = \frac{f}{K_r} + \frac{2d_m(k_y)}{c} \tag{A.19}$$

Substituting the above value in equation A.18, the following expression is obtained:

$$\Theta_m(f,k_y) = -2k_c r_m + \frac{r_m k_y^2}{4k_c} - k_y y_m + \pi K_r \left(\frac{f}{K_r}\right)^2 - 2\pi \frac{f^2}{K_r} - \frac{4\pi f}{c}\left(r_m + \frac{r_m k_y^2}{8k_c^2}\right) \quad \text{(A.20)}$$

Using $\Delta k = 2\pi f/c$ and a few simple mathematical manipulations, the 2D FT is given as

$$S_m(\Delta k, k_y) = \exp\left\{-j2(k_c+\Delta k)r_m - jk_y y_m - j\frac{\Delta k^2 c^2}{K_r \pi} + j\frac{r_m k_y^2}{4k_c} - j\frac{\Delta k r_m k_y^2}{4k_c^2}\right\} \quad \text{(A.21)}$$

A.2 Large Azimuth Aperture

In this case, the approximation in equation A.10 cannot be used that makes the calculations more complicated.

A.2.1 Time Fourier Transform

The phase of the integral that needs to be evaluated in this case is given as

$$\Theta_m(t,y) = -2k_c d_m(y) + \pi K_r \left(t - \frac{2d_m(y)}{c}\right)^2 - 2\pi f t \quad \text{(A.22)}$$

The derivation of this phase and the subsequent time when this derivative is 0 is given by

$$t = \frac{f}{K_r} + \frac{2d_m(y)}{c} \quad \text{(A.23)}$$

Substituing the above value of t in equation A.22, the phase can be written as

$$\Theta_m(f,y) = -2k_c d_m(y) + \frac{\pi f^2}{K_r} - \frac{4\pi f d_m(y)}{c} \quad \text{(A.24)}$$

or

$$\Theta_m(\Delta k, y) = -2(k_c+\Delta k)d_m(y) - \frac{\Delta k^2 c^2}{4\pi K_r} \quad \text{(A.25)}$$

The last phase term is actually the phase of the range chirp and can be used to describe the FT of the chirp as

$$P(\Delta k) = \exp\left\{-j\frac{\Delta k^2 c^2}{4\pi K_r}\right\} \quad \text{(A.26)}$$

It shows that the FT of a chirp signal is again a chirp, as described in [2].

Note that the use of FT assumes that the value of t is centered around 0, whereas, in the actual received RD, the received chirps are centered around the time corresponding

to the middle of the scene. Thus, the RD in case of processing by OKA should be multiplied by $\exp(-j2\Delta k r_{ref})$ and the RD simulated by inverse OKA should be multiplied by $\exp(j2\Delta k r_{ref})$. r_{ref} is the reference range, which is usually chosen to be in the middle of the scene.

A.2.2 Validity Domain for Small Azimuth Aperture Approximation

The validity of the FT pairs for the small azimuth aperture can be calculated by considering the following series expansion of the radar-target distance:

$$d_m(y) = r_m + \frac{(y - y_n)^2}{2r_m} - \frac{(y - y_n)^4}{8r_m^3} + ... \tag{A.27}$$

The phase error due to ignoring terms higher than first-order, in the case of parabolic approximation, can be calculated by putting a limit that the phase error due to the second-order term should be very small, assuming that it is large enough to contain the phase error for higher-order terms:

$$\begin{aligned} k\frac{(y - y_n)^4}{4r_m^3} &\ll 1 \\ k\frac{\Delta Y^4}{64r_m^3} &\ll 1 \end{aligned} \tag{A.28}$$

Assuming $k \approx k_c$ and using the relationship given by equation 1.8, the limit on the azimuth aperture angle is

$$\theta_{ymax}^4 \ll \frac{64}{k_c r_m} \tag{A.29}$$

A.2.3 2D Fourier Transform

In this case, the phase function is

$$\Theta_m(\Delta k, y) = -2(k_c + \Delta k)d_m(y) - \frac{\Delta k^2 c^2}{4\pi K_r} - k_y y \tag{A.30}$$

The derivative of the radar-target distance with respect to the azimuth position is

$$\frac{d\{d_m(y)\}}{dy} = \frac{y - y_m}{\sqrt{r_m^2 + (y - y_m)^2}} \tag{A.31}$$

Using this value in the derivative of the phase function, the consequent manipulations give

$$y = -\frac{k_y r_m}{\sqrt{4(k_c + \Delta k)^2 - k_y^2}} + y_m \tag{A.32}$$

Substituting this value in equation A.30 gives

$$\Theta_m(\Delta k, k_y) = \frac{-2(k_c+\Delta k)r_m\sqrt{1+\frac{k_y^2}{4(k_c+\Delta k)^2-k_y^2}}\sqrt{4(k_c+\Delta k)^2-k_y^2}+r_m k_y^2}{\sqrt{4(k_c+\Delta k)^2-k_y^2}} - \frac{\Delta k^2 c^2}{4\pi K_r} - k_y y_m \tag{A.33}$$

that leads to

$$S_m(\Delta k, k_y) = \exp\left\{-jr_m\sqrt{4(k_c+\Delta k)^2-k_y^2} - j\frac{\Delta k^2 c^2}{4\pi K_r} - jk_y y_m\right\} \tag{A.34}$$

This equation, that varies with the range and azimuth position, can be used to derive matched filters in the 2D frequency domain and is used in the OKA.

A.2.4 Azimuth Fourier Transform

The inverse time FT of equation A.34 leads to an expression of RD in the time azimuth-wavenumber domain. However, to simplify the calculations, an approximation is made [3], [46] to the phase term of the integral as well as the substitution $f = c\Delta k/(2\pi)$. Under this approximation, a Taylor series expansion is used and any terms higher than the quadratic term in transmitted frequency are ignored. The phase is given as

$$\Theta_m(f, k_y) = -\sqrt{4k_c^2-k_y^2}r_m - \frac{8k_c\pi f}{c\sqrt{4k_c^2-k_y^2}}r_m + \frac{8k_y^2\pi^2 f^2}{c^2(4k_c^2-k_y^2)^{3/2}}r_m - \frac{\pi f^2}{K_r} - k_y y_m + 2\pi f t \tag{A.35}$$

Its derivative with respect to f is zero at the following value of f:

$$f = K(r_m, k_y)\left(t - \frac{4k_c r_m}{c\sqrt{4k_c^2-k_y^2}}\right) \tag{A.36}$$

where

$$K(r_m, k_y) = \frac{K_r}{1-K_r e(k_y)} \tag{A.37}$$

$e(k_y) = (k_y^2\pi r_m)/(k_c^3 a^3(k_y)c^2)$ and $a^2(k_y) = 1-(k_y/2k_c)^2$. Using the value of f given in equation A.36 and a few mathematical manipulations elaborated as follows, the phase simplifies to equation A.39.

$$\begin{aligned}\Theta_m(t,k_y) &= -\sqrt{4k_c^2-k_y^2}r_m - \frac{8k_c\pi f}{c\sqrt{4k_c^2-k_y^2}}r_m\frac{K_r}{1-K_re(k_y)}\left(t-\frac{4k_cr_m}{c\sqrt{4k_c^2-k_y^2}}\right)+\pi e(k_y)\\ &\left(\frac{K_r}{1-K_re(k_y)}\right)^2 r_m\left(t-\frac{4k_cr_m}{c\sqrt{4k_c^2-k_y^2}}\right)^2-\frac{\pi}{K_r}\left(\frac{K_r}{1-K_re(k_y)}\right)^2 r_m\\ &\left(t-\frac{4k_cr_m}{c\sqrt{4k_c^2-k_y^2}}\right)^2-k_ry_m+2\pi f\frac{K_r}{1-K_re(k_y)}\left(t-\frac{4k_cr_m}{c\sqrt{4k_c^2-k_y^2}}\right)\end{aligned} \tag{A.38}$$

$$\begin{aligned}&= -\sqrt{4k_c^2-k_y^2}r_m+(t-\frac{4k_cr_m}{c\sqrt{4k_c^2-k_y^2}})^2\frac{2\pi K_r}{1-K_re(k_y)}\\ &+\left(t-\frac{4k_cr_m}{c\sqrt{4k_c^2-k_y^2}}\right)^2\frac{\pi e(k_y)K_r^2-\pi K_r}{\{1-K_re(k_y)\}^2}\\ &= \pi K(r_m,k_y)\left(t-\frac{2d(r_m,k_y)}{c}\right)^2-2k_cr_ma(k_y)-k_ry_m\end{aligned} \tag{A.39}$$

giving the following expression:

$$S(t,k_y)=\exp\left\{j\pi K(r_m,k_y)\left(t-\frac{2d(r_m,k_y)}{c}\right)^2-j2k_cr_ma(k_y)-jk_ry_m\right\} \tag{A.40}$$

This expression is used in the CSA. It can be easily verified that the dependance of the range migration trajectory on the azimuth position of the scatterer has been removed in the time azimuth- wavenumber domain.

Appendix B

Expanded View from Subaperture Analysis

An expanded view of each building in different subapertures is shown in the next figures. It can be seen that buildings A, B and C have the highest DB amplitude in subapertures 2, 1 and 3, respectively. Buildings D and E donot show a high DB amplitude in any of the subapertures, however, the overall amplitude of the scene is the highest in subaperture 2. This is because, the roof and the ground have a small coherent component that lies around 0° aspect angle.

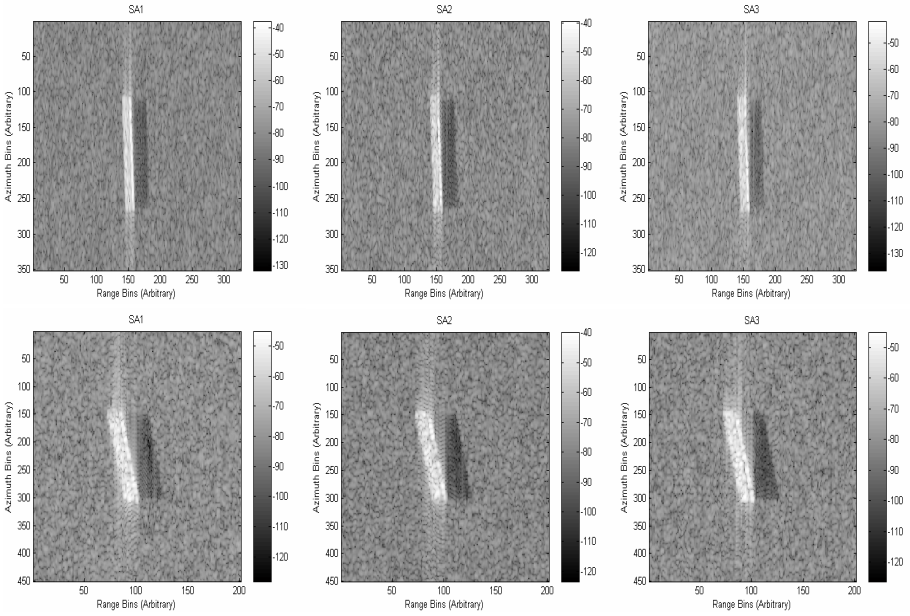

Figure B.1: Magnified View of each Subaperture

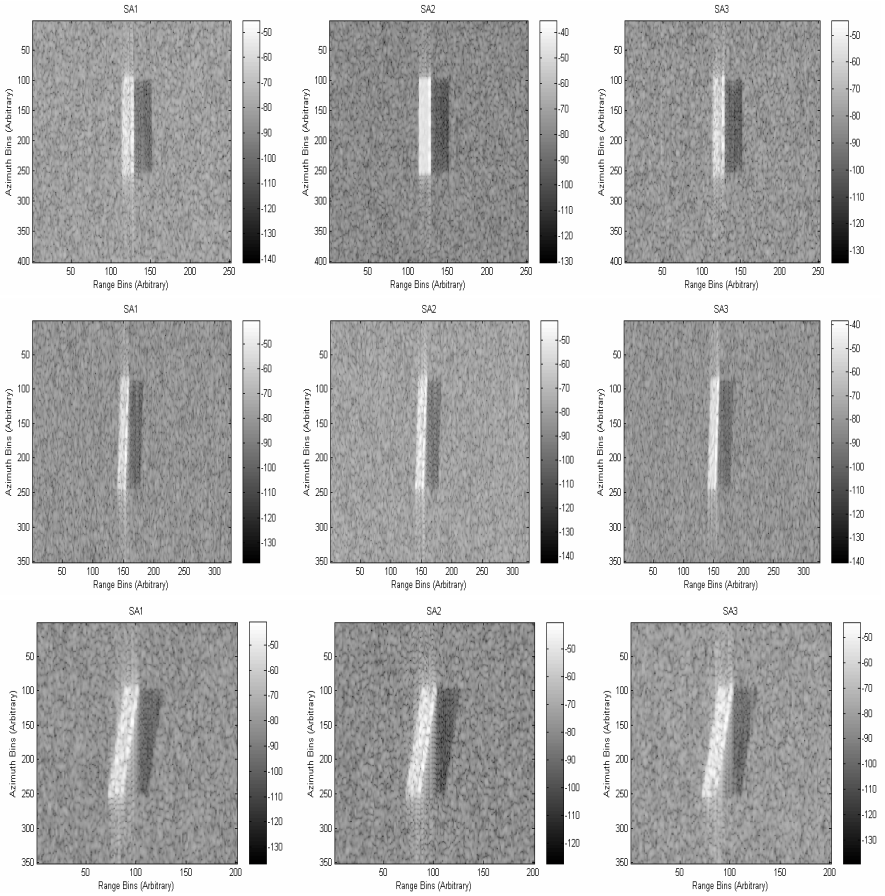

Figure B.2: Magnified View of each Subaperture (Cont'd)

Bibliography

[1] G. Franceschetti and R. Lanari, "Synthetic Aperture Radar Processing", *CRC Press*, 1999.

[2] M. Soumekh, "Synthetic Aperture Radar Signal Processing", *John Wiley and Sons, Inc.*, 1999.

[3] I. Cumming and F. Wong, "Digital Processing of Synthetic Aperture Radar Data", *Norwood, MA: Artech House*, 2005.

[4] K. Raney, H. Runge, R. Bamler, I. Cumming and F. Wong, "Precision SAR processing using chirp scaling ", *IEEE Trans. Geosci. Remote Sens.*, 32:4, 1994.

[5] C. Cafforio, C. Prati and F. Rocca, "SAR Data Focusing using Seismic Migration Techniques", *IEEE Trans. Aerosp. Electron. Syst.*, 27:2, 1991.

[6] W. Carrara, R.Goodman and R. Majewski, "Spotlight Synthetic Aperture Radar", *Norwood, MA: Artech House*, 1995.

[7] B. Brand, S. Florio, T. Neff, R. Speck and T. Zehetbauer, "Simulation Tool for SAR Missions", *Proc. EUSAR*, 2006.

[8] J. M-Hilberg, "PIRDIS: A New Versatile Tool for SAR/MTI Systems Simulation", *Proc. EUSAR*, 2006.

[9] G. Franceschetti, R. Guida, A. Iodice, D. Riccio and G. Ruello, "Efficient Simulation of Hybrid Stripmap/Spotlight SAR Raw Signals from Extended Scenes", *IEEE Trans. Geosci. Remote Sens.*, 42:11, 2004.

[10] G. Franceschetti and G. Schirinzi, "A SAR Processor Based on Two-Dimensional FFT Codes", *IEEE Trans. Aerosp. Electron. Syst.*, 26:2; 1990.

[11] G. Franceschetti, M. Migliaccio, D. Riccio and G. Schirinzi, "SARAS: A SAR Raw Signal Simulator", *IEEE Trans. Geosci. Remote Sens.*, 30, 1992.

[12] G.Fornaro, "Trajectory Deviations in Airborne SAR: Analysis and Compensation", *IEEE Trans. Aerosp. Electron. Syst.*, 35, 1999.

[13] A. Moreira and H. Yonghong, "Airborne SAR Processing of Highly Squinted Data using a Chirp Scaling Approach with Integrated Motion Compensation", *IEEE Trans. Geosci. Remote Sens.*, 32:5, 1994.

[14] A. Reigber, E. Alivizatos, A. Potsis and A. Moreira, "Extended Wavenumber Domain SAR Focusing with Integrated Motion Compensation", *IEE Radar, Sonar and Navigation*, 153:3, 2006.

[15] G. Franceschetti, A. Iodice and D. Riccio, "A Canonical Problem in Electromagnetic Backscattering from Buildings", *IEEE Trans. Geosci. Remote Sens.*, 40:8, 2002.

[16] L. Ferro-Famil, A. Reigber and E. Pottier, "Nonstationary Natural Media Analysis from Polarimetric SAR data using a Two-Dimensional Time-Frequency Decomposition Approach", *Can. J. Remote Sensing*, 31:1, 2005.

[17] L. Wray, "Synthetic Aperture Radar Image Simulator for Interferometry", *Master thesis, University of Cape Town*, 2001.

[18] F. Ulaby and C. Elachi, "Radar Polarimetry for Geoscience Applications", *Artech House*, 1990.

[19] G.Fornaro and G.Franceschetti, "Image Registration in Interferometric SAR Processing", *IEE Proc.-Radar, Sonar Navig.*, 142:6, 1995.

[20] P. Prats, A. Reigber and J. Mallorqui, "Interpolation-free coregistration and phase-correction of airborne SAR interferograms", *IEEE Trans. Geosci. Remote Sens.*, 1:3, 2004.

[21] L. Ulander, H. Hellsten and G. Stenström, "Synthetic-Aperture Radar Processing Using Fast Factorized Back-Projection", *IEEE Trans. Aerosp. Electron. Syst.*, 39:3, 2003.

[22] R. Sabry, "Electromagnetic Modeling in the Spectral Domain for Polarimetric Radar Applications", *DRDC*, 2004.

[23] G. Franceschetti, R. Lanari, V. Pascazio and G. Schirinzi, "WASAR: A Wide-Angle SAR Processor," *IEE Proceedings-F*, 139:2, 1992.

[24] R. Bamler, "A Comparison of Range-Doppler and Wavenumber Domain SAR Focusing Algorithms", *IEEE Trans. Geosci. Remote Sens.*, 30:4, 1992.

[25] A. Moreira, J. Mittermayer and R. Scheiber, "Extended Chirp Scaling Algorithm for Air and Spaceborne SAR Data Processing in Stripmap and ScanSAR Imaging Modes", *IEEE Trans. Geosci. Remote Sens.*, 34:5, 1996.

[26] J. Goodman, "Some Fundamental Properties of Speckle", *J. Opt. Soc. Am.*, 66:11, 1976.

[27] A. Guarbeiri and C. Prati, "SAR Interferometry: A "Quick and Dirty" Coherence Estimator for Data Browsing", *IEEE Trans. Geosci. Remote Sens.*, 35:3, 1997.

[28] A. Reigber, "Airborne Polarimetric SAR Tomography", *PhD thesis, University of Stuttgart*, 2001.

[29] A. Mori and F. De Vita, "A Time-Domain Raw Signal Simulator for Interferometric SAR", *IEEE Trans. Geosci. Remote Sens.*, 42:9, 2004.

[30] M. Vandewal, R. Speck and H. Suß, "A UAV-Based Raw Data Simulator for Complex Scenes", *Proc. EUSAR 2006.*

[31] M. Vandewal, R. Speck and H. Suß, "Efficient SAR Raw Data Generation including Low Squint Angles and Platform Instabilities", *IEEE Letters Geosci. Remote Sens.*, 5:1, 2007.

[32] G. Franceschetti, A. Iodice, S. Perna and D. Riccio, "SAR Sensor Trajectory Deviations: Fourier Domain Formulation and Extended Scene Simulation of Raw Signal", *IEEE Trans. Geosci. Remote Sens.*, 44:9, 2006.

[33] G. Franceschetti, A. Iodice, S. Perna and D. Riccio, "Efficient Simulation of Airborne SAR Raw Data of Extended Scenes", *IEEE Trans. Geosci. Remote Sens.*, 44:10, 2006.

[34] S. Cloude and E. Pottier, "A review of target decomposition theorems in radar polarimetry", *IEEE Trans. Geosci. Remote Sens.*, 34:2, 1996.

[35] K. Eldhuset, "Raw Signal Simulation for Very High Resolution SAR Based on Polarimetric Scattering Theory", *Proc. IGARSS*, 2004.

[36] K. Eldhuset, "High Resolution Spaceborne IN-SAR Simulation with Extended Scenes", *IEE Proc.-Radar sonar Navig.*, 152:2, 2005.

[37] S. Cimmino, G. Franceschetti, A. Iodice, D. Riccio and G. Ruello, "Efficient Spotlight SAR Raw Signal Simulation of Extended Scenes", *IEEE Trans. Geosci. Remote Sens.*, 41:10, 2003.

[38] M. Soumekh, "Fourier Array Imaging", *P T R Prentice-Hall, Inc.*, 1994.

[39] K. Raney, "Synthetic Aperture Imaging Radar and Moving Targets", *IEEE Trans. Aerosp. Electron. Syst.*, AES-7:3, 1971.

[40] V. Chen and H. Ling, "Time-Frequency Transforms for Radar Imaging and Signal Analysis", *Artech House*, 2002.

[41] G. Franceschetti, V. Pascazio and G. Schirinzi, "A SAR Raw Data Simulator of Nonstationary Scenes", *Proc. IGARSS*, 1990.

[42] S. Madsen, "Motion compensation for Ultra Wide Band SAR", *Proc. IGARSS*, 2001.

[43] G. Fornaro, G. Franceschetti and S. Perna, "On Center-Beam Approximation in SAR Motion Compensation", *IEEE Letters Geosci. Remote Sens.*, 3:2, 2006.

[44] W. Carrara, S. Tummala and R. Goodman, "Motion Compensation Algorithm for Widebeam Stripmap SAR", *Proc. SPIE Conference*, 5 June 1995.

[45] S. Méric, "Etude de l'influence et de la correction des mouvements perturbateurs du porteur pour imagerie radar à ouverture synthétique", *PhD thesis, INSA (Rennes)*, 1996.

[46] K. Raney, "A New and Fundamental Fourier Transform Pair", *Proc. IGARSS*, 1992.

[47] N. Bleistein and R. Handelsman, "Asymptotic Expansions of Integrals", *Dover Publications*, 1986.

[48] D. Zhu, Y. Li and Z. Zhu, "A Keystone Transform without Interpolation for SAR Ground Moving-Target Imaging", *IEEE Trans. Geosci. Remote Sens.*, 4:1, 2007.

[49] P. Vachon, K. Raney and W. Emery, "A Simulation for Spacebome SAR Imagery of a Distributed, Moving Scene", *IEEE Trans. Geosci. Remote Sens.*, 27:1, 1989.

[50] D. Fernandez, G. Waller and J. Moreira, "Registration of SAR Images using the Chirp Scaling Algorithm", *Proc. IGARSS*, 1996.

[51] J. Son, G. Thomas and B. Flores, "Range-Doppler Radar Imaging and Motion compensation", *Artech House*, 2001.

[52] F. Xu and Y. Jin, "Imaging Simulation of Polarimetric SAR for a Comprehensive Terrain Scene using the Mapping and Projection Algorithm", *IEEE Trans. Geosci. Remote Sens.*, 44:11, 2006.

[53] F. Gini and F. Lombardini, "Multibaseline Cross-Track SAR Interferometry: A Signal Processing Perspective", *IEEE Trans. Aerosp. Electron. Syst.*, 20:8, 2005.

[54] S. Sauer, L. Ferro-Famil, A. Reigber and E. Pottier, "Multibaseline POL-InSAR Analysis of Urban Scenes for 3D Modeling and Physical Feature Retrieval at L-band", *Proc. IGARSS*, 2007.

[55] J. Oglivy, "Theory of Wave Scattering from Random Rough Surfaces", *IOP Publishing*, 1991.

[56] L. Porcello, N. Massey, R. Innes and J. Marks, "Speckle Reduction in Synthetic-Aperture Radars", *J. Opt. Soc. Am.*, 66:11, 1976.

[57] K. Tomiyasu, "Computer Simulation of Speckle in a Synthetic Aperture Radar Image Pixel ", *IEEE Trans. Geosci. Remote Sens.*, GE-21:3, 1983.

[58] K.Raney, "SAR Response to Partially Coherent Phenomena ", *IEEE Trans. Antennas Propagat.*, 28:6, 1980.

[59] C. Oliver and S. Quegan, "Understanding Synthetic Aperture Radar Images", *Artech House*, 1998.

[60] F. Leberl, "Radargrammetric Image Processing", *Artech House*, 1990.

[61] G. Franceschetti, A. Iodice, D. Riccio and G. Ruello, "SAR Raw Signal Simulation for Urban Structures ", *IEEE Trans. Geosci. Remote Sens.*, 41:9, 2003.

[62] P. Leducq, "Traitements temps-fréquence pour l'analyse de scènes complexes dans les images SAR polarimétriques", *PhD thesis, University of Rennes 1*, 2006.

[63] L. Tsang, J. Kong and R. Shin, "Theory of Microwave Remote Sensing", *John Wiley and Sons*, 1985.

[64] K. Tomiyasu, "Tutorial Review of Synthetic-Aperture Radar (SAR) with Applications to Imaging of the Ocean Surface ", *Proc. IEEE*, 66:5, 1978.

[65] K. Hayashi, R. Sato, Y. Yamaguchi and H. Yamada, "Polarimetric Scattering Analysis for a Finite Dihedral Corner Reflector", *IEICE Trans. Commun.*, E89-B:1, 2006.

[66] R. Schneider, K. Papathanassiou, I. Hajnsek and A. Moreira, "Polarimetric and Interferometric Characterization of Coherent Scatterers in Urban Areas", *IEEE Trans. Geosci. Remote Sens.*, 44:4, 2006.

[67] R. Schneider, K. Papathanassiou, I. Hajnsek and A. Moreira, "Characterisation of Coherent Scatterers in Urban Areas by Means of Angular Diversity", *Proc. IGARSS*, 2006.

[68] R. Bamler and P. Hartl, "Synthetic Aperture Radar Interferometry", *Inverse Problems*, 14, 1998.

[69] F. Gatelli, A. Guamieri, F. Parizzi, P. Pasquali, C. Prati and F. Rocca, "The Wavenumber Shift in SAR Interferometry", *IEEE Trans. Geosci. Remote Sens.*, 32:4, 1994.

[70] H. Zebker and J. Villasenor, "Decorrelation in Interferometric Radar Echoes", *IEEE Trans. Geosci. Remote Sens.*, 30:5, 1992.

[71] G. Franceschetti, A. Iodice, M. Migliaccio and D. Riccio, "A Novel Across-Track SAR Interferometry Simulator ", *IEEE Trans. Geosci. Remote Sens.*, 36:3, 1998.

[72] W. Xu and I. Cumming, "Simulator for Repeat-Pass Satellite InSAR Studies", *Proc. IGARSS*, 1997.

[73] C. Prati and F. Rocca, "Improving Slat-Range Resolution with Multiple SAR Surveys", *IEEE Trans. Aerosp. Electron. Syst.*, 29:1, 1993.

[74] A. Reigber, "Range Dependent Spectral Filtering to Minimize the Baseline Decorrelation in Airborne SAR Interferometry", *proc. IGARSS*, 1999.

[75] S. Guillaso, A. Reigber, L. Ferro-Famil and E. Pottier, "Range Resolution Improvement of Airborne SAR Images", *IEEE Letters Geosci. Remote Sens.*, 3:1, 2006.

[76] E. Rodriguez and J. Martin, "Theory and Design of Interferometric Synthetic Aperture Radars", *proc. IEE-F*, 139:2, 1992.

[77] J. Hagberg, L. Ulander and J. Askne, Member, IEEE, "Repeat-Pass SAR Interferometry over Forested Terrain", *IEEE Trans. Geosci. Remote Sens.*, 33:2, 1995.

[78] S. Cloude and K. Papathanassiou, "Polarimetric SAR Interferometry", *IEEE Trans. Geosci. Remote Sens.*, 36:5, 1998.

[79] G. Franceschetti, M. Migliaccio and D. Riccio, "On Ocean SAR Raw Signal Simulation", *IEEE Trans. Geosci. Remote Sens.*, 36:1, 1998.

[80] D. Lyzenga, "Numerical Simulation of Synthetic Aperture Radar Image Spectra for Ocean Waves", *IEEE Trans. Geosci. Remote Sens.*, GE-24:6, 1986.

[81] M. Bao, C. Bruning and W. Alpers, "Simulation of Ocean Waves Imaging by an Along-Track Interferometric Synthetic Aperture Radar", *IEEE Trans. Geosci. Remote Sens.*, 35:3, 1997.

[82] K. Raney and G. Wessels, "Spatial Considerations in SAR Speckle Consideration", *IEEE Trans. Geosci. Remote Sens.*, 26:5, 1988.

[83] P. Rosen, S. Hensley, I. Joughin, F. Li, S. Madsen, E. Rodriguez and R. Goldstein, "Synthetic Aperture Radar Interferometry", *Proc. IEEE*, 88:3, 2000.

[84] G. Franceschetti, M. Migliaccio and D. Riccio "The SAR Simulation: an Overview", *proc. IGARSS*, 1995.

[85] K. Tansey, K. White, A. Millington and A. Battikhi, "Comparison of Modelled Backscatter Response and ERS-1 SAR Data for Desert Surfaces, the Eastern Badia of Jordan", 3^{rd} *ERS Symposium*, 1997.

[86] A. S. Khwaja, L. Ferro-Famil and E. Pottier, "SAR Raw Data Simulation using High Precision Focusing Methods", *Proc. EUSAR*, 2006.

[87] A. S. Khwaja, L. Ferro-Famil and E. Pottier, "SAR Raw Data Simulation using Inverse SAR Image Formation Algorithms", *Proc. IGARSS*, 2006.

[88] A. S. Khwaja, L. Ferro-Famil and E. Pottier, "SAR Raw Data Simulation in the Frequency Domain", *Proc. EURAD*, 2006.

[89] A. S. Khwaja, L. Ferro-Famil and E. Pottier, "SAR Raw Data Simulation in case of Motion Errors", *Proc. IEEE RADAR Conference*, 2008.

Résumé

Cette thèse traite de la simulation rapide de données SAR au moyen de méthodes de synthèse inverse. Pour ce faire, les algorithmes omega-k et chirp scaling inverses sont dévelopés pour le cas d'une trajectoire lineaire. Une transformation est proposée, qui permet de produire des données brutes d'un objet mobile à partir d'image SAR d'un objet statique opérant dans le domaine spectral. Les déviations non-linéaires de trajectoire du capteur sont aussi prises en considération en simulant des données partiellement dans le domaine temporel avec l'approximation d'un faisceau d'antenne étroit en largeur ou avec l'approximation d'une largeur de bande réduite. Toutes ces techniques sont analysées et les résultats sont comparés avec ceux d'un simulateur temporel pris comme réfèrence. Les données brutes sont simulées pour une scène complexe comportant un ou plusiers bâtiments placés au sein d'un environnement naturel surfacique et ayant une réponse anisotrope. Finalement, la simulation d'images et de données interférometriques est abordée.

Mots-clés: Télédétection, radar à ouverture synthétique, méthodes de simulation.

Summary

This thesis concerns efficient SAR raw data simulation making use of inverse raw data processing. For this purpose, the Omega-k and Chirp Scaling algorithms are inversed to generate raw data for an ideal sensor trajectory. Raw data simulation corresponding to a moving object is also shown to be a modified form of these two dimensional frequency domain simulation algorithms. The case of sensor trajectory errors is considered next and it is demonstrated that this process can be carried out partially in the time domain by making narrow-beamwidth and narrow-bandwidth approximations. These approximations are analyzed, alongwith examples for a point scatterer to check the accuracy of the simulated data compared to those generated by a reference time domain simulator. Finally, these techniques are applied to generate raw data for a complex scene, consisting of a single or multiple buildings placed on a rough ground. The anisotropic nature of the building response is also taken into account, besides introducing interferometric image and raw data simulation.

Keywords: Remote sensing, synthetic aperture radar (SAR), simulation methods.